SERRI Report 70015-001

LEVEE BREACH GEOMETRIES AND ALGORITHMS TO SIMULATE BREACH CLOSURE

SERRI Project: *Increasing Community Disaster Resilience Through Targeted Strengthening of Critical Infrastructure*

Project Principal Investigator:
Isaac L. Howard, PhD

Report Written and Performed By:

Chris L. Saucier - Mississippi State University
Isaac L. Howard - Mississippi State University
Joe G. Tom, Jr. - Mississippi State University

"An Industry, Agency & University Partnership"

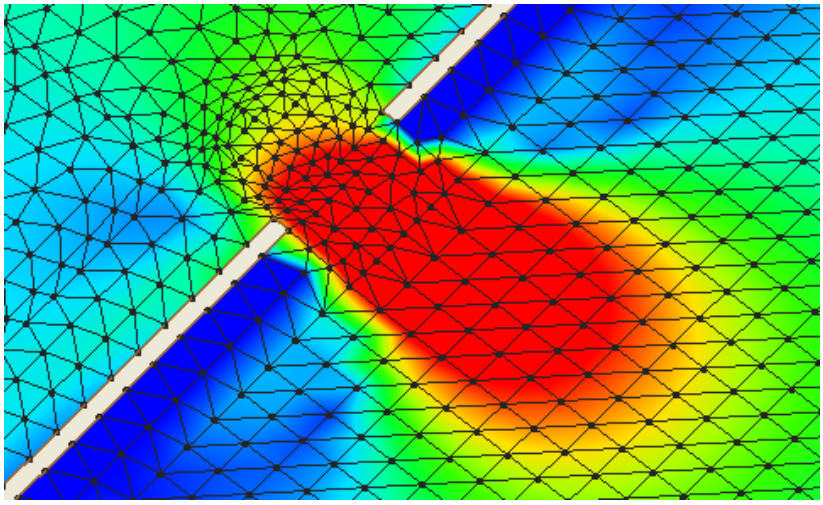

This material is based upon work supported by the U.S. Department of Homeland Security under U.S. Department of Energy Interagency Agreement 43WT10301. The views and conclusions contained in this document are those of the authors and should not be interpreted as necessarily representing the official policies, either expressed or implied, of the U.S. Department of Homeland Security.

SERRI Project: Increasing Community Disaster Resilience
Through Targeted Strengthening of Critical Infrastructure

LEVEE BREACH GEOMETRIES AND ALGORITHMS TO SIMULATE BREACH CLOSURE

Written By:

Chris L. Saucier - Mississippi State University
Isaac L. Howard - Mississippi State University
Joe G. Tom, Jr. - Mississippi State University

Date Published:

October 2009

Prepared for
U.S. Department of Homeland Security
Under U.S. Department of Energy Interagency Agreement 43WT10301

Prepared by
OAK RIDGE NATIONAL LABORATORY
Oak Ridge, Tennessee 37831-6283
managed by
UT-BATTELLE, LLC
for the
U.S DEPARTMENT OF ENERGY
under contract DE-AC05-00OR22725

Technical Report Documentation Page

1. **Report No.** SERRI Report 70015-001	2. **Government Accession No.**	3. **Recipient's Catalog No.**
4. **Title and Subtitle** Levee Breach Geometries and Algorithms to Simulate Breach Closure		5. **Report Date** 12 October 2009
		6. **Performing Organization Code**
7. **Author(s) and Affiliation(s)** Chris L. Saucier, Assistant Professor, Mississippi State University Isaac L. Howard, Assistant Professor, Mississippi State University Joe G. Tom, Jr., Undergraduate Research Assistant, Mississippi State University.		8. **Performing Organization Report No.** CMRC-09-01
9. **Performing Organizations Name and Address** Mississippi State University Department of Civil and Environmental Engineering 501 Hardy Road / P O Box 9546 Mississippi State, Mississippi 39762-9546		10. **Work Unit No. (TRAIS)**
		11. **Contract or Grant No.** TO 4000064719
12. **Sponsoring Agency Name and Address** U.S. Department of Homeland Security Science and Technology Directorate Washington, DC 20528		13. **Type of Report and Period Covered** Final Report Jan 2008 to Dec 2008
		14. **Sponsoring Agency Code**

Supplementary Notes: Work performed under Mississippi State University research project entitled "Increasing Community Disaster Resilience Through Targeted Strengthening of Critical Infrastructure." The project number assigned to the work by the sponsor was 70015. Research sponsor administers project contract for the Department of Homeland Security's Southeast Regional Research Initiative (SERRI). This report is Volume I in a series of reports performed as part of this research effort.

16. **Abstract**

This report examines the common conditions in which levee breaches may exist and the various means by which the typical size of a levee breach may be estimated. These assessments may be used to crudely define the conditions acting near a levee breach at the initiation of a closure attempt. When coupled with additional information regarding the polder size, polder topography, and flood period, these initial assessments have been demonstrated to provide additional critical information regarding the time available to achieve breach closure.

A set of computational algorithms have been developed to simulate the motion of solid particles entrained within a fluid flow. These algorithms were developed for specific application to the problem of achieving levee breach closure via entraining large solid masses into the breach discharge. However, the proposed techniques are general in nature and may be useful in applications beyond the levee breach closure problem. The algorithms are centered upon modeling the trajectory of the solid masses (e.g., the "particles") under the influence of interactions with a flowing fluid, local boundaries, and other particles. The motions of the fluid in the vicinity of the particle are independently-generated from a hydrodynamic simulation. The resulting fluid velocity field is maintained constant over a small increment of time corresponding to that required for a single particle to be entrained and subsequently come to rest. An entire simulation of breach closure may be created through successive cycles alternating between the hydrodynamic model and the particle trajectory model.

Several simplifying assumptions were employed to demonstrate the proposed algorithms for the case of spherical particles in free-fall through a water column. The results obtained from the simulation compare well with those observed in a separately-performed experimental program.

17. **Key Words** Flooding, Levee, Breach Closure, Distinct Element Method, Sediment Transport	18. **Distribution Statement** TBD		
19. **Security Classif. (this report)** TBD	20. **Security Classif. (this page)** TBD	21. **No. of Pages** 154	22. **Price**

Form DOT F 1700.7 (8-72) **Reproduction of completed page authorized**

TABLE OF CONTENTS

LIST OF FIGURES

LIST OF FIGURES (CONTINUED)

LIST OF FIGURES (CONTINUED)

LIST OF TABLES

LIST OF SYMBOLS

The following symbols are used in this document. Lower case symbols accented by boldface type and an underline (e.g., $\underline{\mathbf{a}}$) represent vector quantities. Upper case symbols accented by boldface type and an underline (e.g., $\underline{\mathbf{T}}$) represent tensor quantities. Unless specifically noted below, all remaining symbols represent scalar quantities.

$\underline{\mathbf{a}}$	=	acceleration
A_L	=	cross-sectional area of levee
A_P	=	plan area of drainage polder
b	=	width of levee crown (in levee cross-section)
$\underline{\mathbf{b}}$	=	body force
B	=	breach length (along centerline of levee)
c	=	cohesive component of strength in Mohr-Coulomb failure criterion
c_{CF}	=	contact friction constant for interparticle shear slip
c_{CN}	=	contact damping constant for normal forces
c_{CS}	=	contact damping constant for shear forces
c_{GN}	=	global damping constant for particle displacement
c_{GW}	=	global damping constant for particle rotation
C_D	=	particle drag coefficient
d_{CF} or $\underline{\mathbf{d}}_{CF}$	=	contact friction damping force
d_{CN} or $\underline{\mathbf{d}}_{CN}$	=	contact normal damping force
d_{CS} or $\underline{\mathbf{d}}_{CS}$	=	contact shear damping force
d_{GN} or $\underline{\mathbf{d}}_{GN}$	=	global damping force applied to translational motion of particle
d_{CS} or $\underline{\mathbf{d}}_{CS}$	=	global damping force applied to rotation of particle
d_I	=	permissible average inundation depth over polder area
d_S	=	scour depth below bottom of levee
D	=	depth of levee breach
$D_{(i)}$	=	diameter of Particle (i)
$\underline{\mathbf{e}}$	=	orthonormal base vector

E	=	an error measure
$\mathbf{E}_{TOL}$	=	an error tolerance
f or $\underline{\mathbf{f}}$	=	force
f_A or $\underline{\mathbf{f}}_A$	=	apparent mass force due to fluid displacement
f_B or $\underline{\mathbf{f}}_B$	=	body force due to buoyancy
f_D or $\underline{\mathbf{f}}_D$	=	force on particle due to viscous fluid drag
f_G or $\underline{\mathbf{f}}_G$	=	gravitational force on particle
f_H or $\underline{\mathbf{f}}_H$	=	Basset force
f_N or $\underline{\mathbf{f}}_N$	=	normal force from interaction with adjacent particles or boundaries
f_S or $\underline{\mathbf{f}}_S$	=	tangential force from interaction with adjacent particles or boundaries
g or $\underline{\mathbf{g}}$	=	gravitational acceleration constant
< g >	=	subscript indicator for computational iteration
h	=	water depth
h_F	=	water depth on flood side of levee
h_L	=	height of levee
h_P	=	water depth on protected side of levee
□	=	rate of heat exchange
Ħ« x »	=	Heaviside step function centered at position x
(i)	=	subscript for particle number
(i : j)	=	subscript for contact from Particle (i) to Particle (j)
(i : k]	=	subscript for contact from Particle (i) to Boundary [k]
(i : y /	=	subscript for Force /y/ within vicinity of Particle (i)
İ	=	mass moment of inertia
J	=	number of particles in contact with Particle (i)
[k]	=	subscript for boundary number
k_{BN}	=	stiffness for particle-to-boundary normal displacements
k_{BS}	=	stiffness for particle-to-boundary shear displacements
k_N	=	stiffness for interparticle normal displacements

k_S	=	stiffness for interparticle shear displacements
K	=	number of boundaries in contact with Particle (i)
m	=	mass
m_F	=	side slopes of levee on flood side
m_P	=	side slopes of levee on protected side
m_W	=	side slopes of levee breach
n	=	Manning's roughness
$\underline{\mathbf{n}}$	=	unit vector normal to surface
p or $\underline{\mathbf{p}}$	=	boundary normal traction
P_S	=	"shaft work", an externally-supplied power to a control volume
q	=	series summation index
Q_D	=	breach discharge
Q_S	=	discharge capacity of flood source
r or $\underline{\mathbf{r}}$	=	relative velocity between particle and surrounding fluid
$\underline{\mathbf{R}}$	=	rotation tensor (rotation thru $\pi/2$ radians, unless noted)
$\mathbf{R}$	=	Reynold's number (scalar value)
$\underline{\mathbf{s}}$	=	unit vector tangent to surface
t	=	torque
{ t }	=	subscript indicator for time
t_2	=	elapsed time from breach initiation to end of Stage 2 erosion
t_B	=	breach closure time
t_D	=	breach development time
t_F	=	breach formation time or "time to failure"
t_I	=	polder inundation time
t_Q	=	breach balance time
T_F	=	period of flood source (inverse of flood wavelength)
u_N or $\underline{\mathbf{u}}_N$	=	normal displacement
u_S or $\underline{\mathbf{u}}_S$	=	shear displacement

v or $\underline{\mathbf{v}}$	=	velocity
v_N or $\underline{\mathbf{v}}_N$	=	velocity of normal displacement
v_S or $\underline{\mathbf{v}}_S$	=	velocity of shear displacement
V	=	volume
w_S or $\underline{\mathbf{w}}_S$	=	static torque for particle rotation
w_θ or $\underline{\mathbf{w}}_\theta$	=	damping torque for particle rotation
w or $\underline{\mathbf{w}}$	=	angular velocity
W_B	=	width of breach (across cross-section of levee)
x or $\underline{\mathbf{x}}$	=	position
/ y /	=	subscript for forces in neighborhood of Particle (i)
Y	=	number of forces in neighborhood of Particle (i)
z	=	elevation
α	=	interparticle surface cohesive force
β	=	interparticle surface friction coefficient
γ	=	unit weight
δ	=	displacement at which interparticle slip occurs
Δt	=	increment of time
ε	=	extent of a "neighborhood" (a perimeter distance from a point)
θ	=	angular position (orientation with respect to a reference vector)
κ	=	apparent mass fraction
λ	=	second coefficient of viscosity
μ	=	dynamic viscosity
μ^*	=	kinematic viscosity
π	=	circular constant
ρ_F	=	density of fluid
ρ_S	=	density of particle solids
σ or $\underline{\boldsymbol{\sigma}}$	=	normal stress (tensorial quantity when shown with underline)
τ or $\underline{\boldsymbol{\tau}}$	=	shear stress (tensorial quantity when shown with underline)

υ or $\underline{\boldsymbol{\upsilon}}$	=	unhindered velocity of flow field
ϕ	=	frictional component of strength in Mohr-Coulomb failure criterion
ψ	=	parameter or function used to describe particle surface
ω or $\underline{\boldsymbol{\omega}}$	=	angular acceleration (vectorial quantity when with underline)
$\lVert \underline{\mathbf{v}} \rVert$	=	scalar norm of a vector $[\ \underline{\mathbf{v}} \cdot \underline{\mathbf{v}}\ ]^{1/2}$
$\lvert\ \underline{\mathbf{v}}\ \rvert$	=	normalized unit vector of the vector $\underline{\mathbf{v}} = \underline{\mathbf{v}} \,/\, \lVert \underline{\mathbf{v}} \rVert$
$\nabla_{\underline{\mathbf{x}}}\, \underline{\mathbf{v}}$	=	the gradient operator $(\partial \underline{\mathbf{v}}_i / \partial \underline{\mathbf{x}}_j)\ \underline{\mathbf{e}}_i \otimes \underline{\mathbf{e}}_j$
div	=	the divergence operator
curl	=	the curl operator

UNITS CONVERSIONS

Multiply	by	To Obtain
meters (m)	3.2808	feet (ft)
centimeters (cm)	0.3937	inches (in)
kilometers (km)	0.6214	miles (mi)
meters per second (m/s)	3.2808	feet per second (ft/s)
meters per second (m/s)	2.2369	miles per hour (mph)
hectares (ha)	2.4711	acres (ac)
hectares (ha)	3.8610×10^{-3}	square miles (mi^2)
kilograms (kg)	2.2046	pounds (lbs)
newtons (N)	0.2248	pounds (lbs)
grams per cubic centimeter (g/cm^3)	62.428	pounds per cubic foot (pcf)
kilonewtons per cubic meter (kN/m^3)	6.3661	pounds per cubic foot (pcf)

PREFIXES IN SYSTEME INTERNATIONAL (SI)

kilo- (k)	1.0×10^3	centi- (c)	1.0×10^{-2}
mega- (M)	1.0×10^6	milli- (m)	1.0×10^{-3}
giga- (G)	1.0×10^9	micro- (u)	1.0×10^{-6}

ACKNOWLEDGEMENTS

Thanks are due to many for the successful completion of this report. The authors are especially grateful for the financial support provided by the Southeast Regional Research Initiative (SERRI). In addition, due gratitude is extended to everyone employed at the US Department of Homeland Security (DHS) and Oak Ridge National Laboratory (ORNL) who worked diligently with the authors to make this project a success. A great deal of the success of this research can be attributed to the efforts of DHS and ORNL personnel.

The authors are also thankful for the many fruitful discussions held among colleagues at Mississippi State University. In particular, the valuable comments provided by Drs. William McAnally and Tom White of the MSU Department of Civil and Environmental Engineering; and Dr. Keith Koenig of the MSU Department of Aerospace Engineering are recognized. Dr. McAnally is also thanked for feedback provided related to portions of the work. Finally the assistance of Mr. Jeremy Sharp is recognized for producing the hydrodynamic simulations employing the Adaptive Hydraulics (ADH) computer code.

CHAPTER 1

INTRODUCTION

1.1 Background Information

The work presented in this report was developed in partial fulfillment of the requirements of Task Order No. 4000064719 (hereafter referenced as the "TO") under the Southeast Regional Research Initiative (SERRI) program at the United States Department of Energy's Oak Ridge National Laboratory (ORNL) in Oak Ridge, Tennessee. SERRI is funded by the United States Department of Homeland Security. The research was proposed by members of the Department of Civil and Environmental Engineering (CEE) at Mississippi State University (MSU) to SERRI in a document dated 1 June 2007. The proposed research was subsequently authorized by UT-Battelle in the TO dated 10 December 2007. This task order included a scope of work defined through joint discussions between MSU and SERRI. Work on the project was initiated on 1 January 2008.

While the work presented in this report may be taken as complete and independent of other research efforts within DHS, SERRI, and MSU, it should be noted that the scope of work associated with the TO included several related components. The general objectives of the project were to investigate means for rapidly using on-site materials and methods in ways that would most effectively enable local communities to rebuild in the wake of a flooding disaster. Within this general framework, several key work components were associated with the TO. Specifically, the scope of work dated 10 December 2007 compartmentalizes research efforts into the tasks shown in Table 1.1. The division of the research effort into the tasks shown in Table 1.1 is an internal work division created at MSU. However, it is useful in providing a framework for the research described in this report and other reports developed during the research effort. The work contained in this report was associated with Task 3: Levee Breach Repair-Closure of Breaches in Flood Protection Systems. The report of this work was the first deliverable item of the research project, hence the designation of the report as SERRI Report 70015-001.

It is also important to notice that this component of the TO was truncated in an effort to minimize duplication of existing research efforts within the SERRI program. On

Table 1.1
Overview of Research Components in Task Order

COMPONENT	DESCRIPTION OF RESEARCH
Task 1	Erosion Control-Erosion Protection for Earthen Levee
Task 2	Bridge Stability-Lateral & Uplift Stability of Gravity-Supported Bridge Decks
Task 3	Levee Breach Repair-Closure of Breaches in Flood Protection Systems
Task 4	Pavement Characterization and Repair
Task 5	Emergency Construction Material Development-Staging Platform Construction
Task 6	Fresh Water Reservoir-Restoration of Fresh Water Supplies

18 July 2008, representatives of SERRI convened research teams from MSU and the University of Mississippi (UM) to discuss opportunities for collaborative work between the two teams. During these discussions, substantial overlap was identified between the works being performed by the two research teams in the area of computational simulation of breach closure techniques. As a result of these discussions, MSU submitted a letter on 9 September 2008 which was accompanied by a proposal for modifying the scope of work dated 10 December 2007. The revised scope of work allowed more efficient use of research allocations within SERRI, expanding portions of the MSU contract associated with Tasks 1 and 5 described above. The revised scope of work simultaneously reduced portions of the TO associated with Task 3 in an effort to minimize duplication of research efforts being conducted by MSU and UM researchers. The revised scope of work was endorsed by UM researchers in an electronic mail message dated 22 September 2008, and the proposed modifications to the TO were accepted by UT-Battelle on 29 September 2008. This report represents a final report of Task 3 described in the revised scope of work dated 9 September 2008, and the work presented herein is considered full completion of this task.

1.2 Objectives of Research

As mentioned previously, the general directives of the TO are to investigate several specific means by which local communities may best use available resources in an effort to rapidly recover from a flooding disaster. In the wake of a flooding disaster, this broad objective would include rebuilding a community with the efforts of a variety of professionals practicing within the physical and social sciences. This work is much more narrowly focused upon certain recovery efforts typically associated with civil engineering, as can be seen from the work components described in Section 1.1.

Specifically, the work described in this report is intended to develop means by which researchers may assess the validity of closing active levee breaches by entraining soil or rock masses within the water flow traveling through the breach. Because of the large number of possibilities which may be available to seal active levee breaches, computational simulation of breach closure techniques is a viable technique for reducing the available alternatives to a feasible set for which additional field experimentation and training would be most effective. Due to the truncation of the work effort described previously, the current work is limited to

the development of calculation algorithms associated with the simulations. These efforts will be made available to collaborating research teams within the SERRI initiative, so that the algorithms presented herein may be incorporated into associated research efforts in computational simulation of breach closure.

1.3 Scope of Research

For the specific research component described in this report (Task 3 of Table 1.1), the revised scope of work dated 9 September 2008 includes the items shown in Table 1.2. The scope of work is fully described in Table 1.2 and is thus not elaborated further.

1.4. Incorporation Into the National Response Framework

The National Response Framework (NRF) is a document that guides the United States when conducting all-hazards response ("response" refers to immediate actions to save lives, protect property and the environment, and meet basic human needs). This framework is entailed in NRF (DHS, 2008), which has complimentary material found in print and online. The NRF is a continuation of previous federal level planning documents (e.g. Federal Response Plan of 1992), and serves as the state of the art in responding to disaster events. The following paragraphs summarize how the research conducted in this task of the TO could be applicable to the NRF and in what manner. The tone of the paragraphs assumes the reader is at least casually familiar with the NRF and supporting documentation.

The Stafford Act is a key piece of legislation regarding disaster response and recovery. Specifically, the Stafford Act Public Assistance Program provides disaster assistance to key responding units (e.g. states, local governments). Figure 1.1 was taken from NRF (DHS, 2008) to illustrate the overall disaster funding flowchart that summarizes Stafford Act support.

According to NRF (DHS, 2008), "Resilient communities begin with prepared individuals and depend on the leadership and engagement of local government, nongovernmental organizations, and the private sector." In the authors' opinions, the current level of preparedness for emergency strengthening prior to a water-based catastrophe and

Table 1.2
Items Defining Scope of Work for Task 3

SCOPE ITEM	DESCRIPTION
a)	Identify typical geometries that breach failures may assume for a given flood event and duration.
b)	Define pertinent material properties for sediments distributed around the breach area, with particular emphasis on the effects of these properties on widely available chemical admixtures (e.g., portland cement). The effort attempts to qualitatively correlate soil particle sizes to estimates of moisture and stabilization alternatives.
c)	Develop a method for coupling of hydrodynamic simulation codes (i.e., ADH or HEC) with discrete element methods to simulate the transport of materials dropped into the breach flow to create a closure.
d)	Provide the results of simulations of the type described in c) for a typical stabilized soil mass that may be used to close a typical breach geometry identified in a).

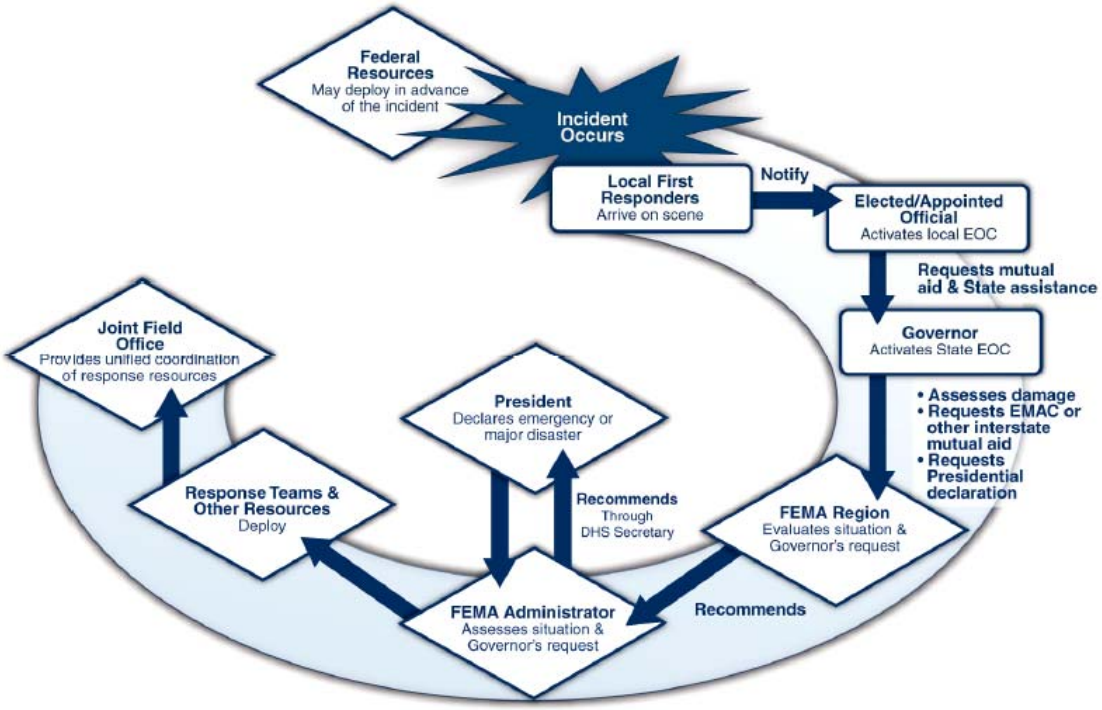

Figure 1.1 Summary of the Stafford Act, as Described in the National Response Framework (DHS, 2008).

emergency construction subsequent to a water-based catastrophe is insufficient. To approach a state of readiness where the United States is "prepared" for these events, protection and mitigation concepts need to be developed and studied to reasonable resolution. Presumably, specific design methods and materials would be developed in association with such an effort (commonly via laboratory scale and analytical studies). These methods and materials would subsequently be demonstrated at full scale, and training would be completed to ensure first responders are capable of performing the requisite tasks. Research efforts of the type reported herein thus represent an appropriate response to eliminate deficiencies in the nation's current level of preparedness.

The NRF is primarily oriented toward implementing nationwide response policy and operational coordination for any domestic event. NRF focuses on responding to and recovering from incidents that do occur, as one of four major components of a larger National Strategy for Homeland Security. While a certain level of risk is unavoidable, NRF (DHS, 2008) states that first responders can effectively anticipate and manage risk through proper training and planning. The research presented in this report is associated with techniques used to properly simulate various options for closing an active breach of a flood protection system. The use of simulation techniques developed from the current work permits an evaluation of multiple proposals for breach closure techniques prior to selection of a limited number of these methods for subsequent field trials. This distillation of proposed alternatives for disaster mitigation is a central element of planning for natural disasters and is thus directly tied to the philosophy of the NRF and the mission of the Department of Homeland Security.

Neither training nor planning appears to be performed to any widespread extent related to emergency design and construction for the purpose of rapidly strengthening and/or repairing civil infrastructure. Training programs that result in certifications to perform certain activities would expedite the identification and selection of pre-qualified organizations or individuals to immediately insert their capabilities into time-sensitive environment of a natural disaster.

The response structure of NRF (DHS, 2008) is based on the National Incident Management System (NIMS). Several key concepts are presented in the NIMS related to initial and ongoing training of first responders. As indicated in Section 1.1, this report is

limited in scope, and is not intended to determine the most appropriate measures for breach closure. However, the larger research objectives of the TO underscore certain needs defined by the NRF. For example, the identification and pre-qualification of first responders mentioned in the previous paragraph aligns closely with the NIMS directives to engage qualified personnel in disaster response to ensure effectiveness.

The goals of the research conducted under the TO align most closely with the needs of the Hurricane Liaison Team (HLT), whose goal is to enhance hurricane disaster response. Response was stated earlier to refer to immediate actions to save lives, protect property and the environment, and meet basic human needs. This particular work component (Task 3 of the TO) is specifically intended to further the mitigation of levee damage which may be caused by hurricane events, though extension of the simulations presented herein may naturally be extended to breaches associated with flood control structures or with tailings ponds or surface water reservoirs. All the aforementioned discussion also aligns with "Scenario 10: National Disaster-Major Hurricane" of the National Planning Scenarios that have been established in NRF (DHS, 2008).

Response at the local level is organized within an Incident Command System (ICS). At the field level local responders use the ICS, which is led by an Incident Commander who has overall authority and responsibility at the incident site. An Emergency Operations Center (EOC) is a physical location established at the incident site. They can be organized by discipline (e.g. transportation), jurisdiction (e.g. city), Emergency Support Function (e.g. engineering), or a combination. A key EOC function is to ensure on scene responders have needed resources. The design recommendations and construction methods produced from each of the six tasks would be needed resources and could be provided through the Incident Commander.

The process of response within the NRF is divided into three stages: gaining and maintaining situational awareness; activating and deploying resources and capabilities; and coordinating response actions. The NRF emphasizes the need to anticipate those resources and capabilities which may be needed, including the potential need to pre-position resources and personnel where the occurrence of a disaster is most likely. Evaluations of the resources necessary for closure of an active breach are furthered by the current research. While local governments retain responsibility for their own public works, the United States Army Corps

of Engineers (USACE) is designated as the primary coordinator of emergency support functions associated with public works and engineering. The current research, through its efforts to aid a-priori assessments of breach closure techniques may prove useful for USACE personnel tasked with the responsibility of conducting pre-incident and post-incident public works and infrastructure assessments and with providing technical and engineering expertise including repair of damaged public infrastructure. The research herein may also be of interest to "Unified Coordination Groups" assembled to provide field support to USACE efforts to manage flood response efforts. Finally, the current work may be of interest to Bureau of Reclamation personnel providing engineering support for damage evaluation of water control systems (e.g. dams and levees).

CHAPTER 2

A CONTEXT FOR BREACH CLOSURE SIMULATIONS

2.1 Introduction

While the problem of levee breach closure has received renewed attention in recent years, it is one which has been considered over a long history of devastating floods in the United States. In testimony before Congress in 1898, Major T.G. Dabney described efforts undertaken to close several large breaches on the Mississippi River south of Memphis during floods occurring in the summer of that year (U.S. Congress, 1898). Subsequent flooding of the Mississippi River in 1927 provided greater motivation for coordinating the efforts of independent levee districts toward public safety. Since that time, the study of levee breaches and means for their mitigation has been largely centralized into efforts led by the U.S. Army Corps of Engineers and the U.S. Bureau of Reclamation. This section of the report attempts to summarize certain characteristics and conditions existing in the vicinity of a breach at the time breach closure is attempted. As the breach closure problem (and thus the simulation of breach closure via computational techniques) may be influenced by the source of flooding, the area being flooded, and the structure that was breached, each of these factors is discussed in some detail.

2.2 The Language of Levee Breaches

Prior to discussion of levee breaches and their geometry, it is useful to introduce several standard terminologies pertinent to the discussion. Figure 2.1 illustrates a typical levee geometry associated with primary flood protection levees used to channelize major river systems in the U.S. In operation, these levees provide separation between the flood-susceptible community on the "protected side" of the levee and the rising floodwaters on the "flood side" of the levee.

The geometries of flood protection levees varies considerably, based on the level of intended protection and local experiences with successful levee construction. This

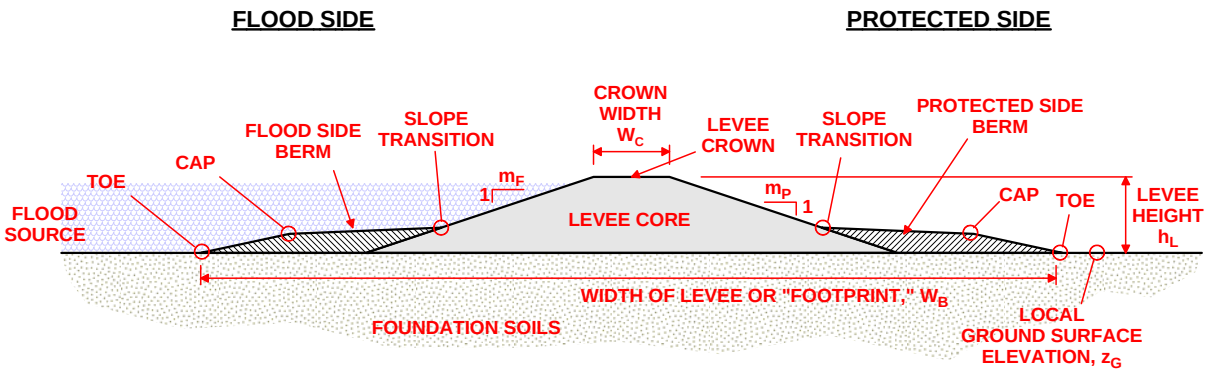

Figure 2.1 Definitions of Terms Associated With Levees.

variation is illustrated by Figure 2.2, in which the geometries of several flood protection levees (including federally-controlled "primary flood protection levees" and locally-controlled levees) are shown. In general, levees may be said to have a steeper-sloping central section, here termed the "core," which may be flanked on either side or both sides by earthen "berms" or "banquettes." The highest elevation of the levee core is defined by the levee "crest" or "crown." The "crown width" shown in Figure 2.1 usually measures 3.0 to 4.5 meters (10 to 15 feet). From the crown, the core commonly broadens as a trapezoidal shape along slopes defined by 3 to 4 units of horizontal distance for every 1 unit of vertical rise (for which an abbreviated notation of the slope would be "1V:4H"). The side slopes of the levee are then defined as 1V:m_F H (on the flood side) and 1V:m_P H (on the protected side), as shown in Figure 2.1. While the core is considered to extend from the elevation of the levee crown to meet the grade of the local ground surface, that part of the core which is exposed to the elements of nature is often limited to a height of 4.5 meters (15.0 feet).

As shown in Figure 2.1, the levee core may be flanked on either side or both sides by a "berm" (sometimes also called a "banquette"). These berms may serve one or more purposes, described in Table 2.1, and the sizes of berms may be anticipated to vary widely according to the intended function(s). In general, trial berm sizes are selected and analyzed for each function which the berm may provide, and the design of the berm is optimized to provide a suitable minimum level of safety appropriate for each of these its intended functions.

The berms are said to encounter the levee core at an elevation corresponding to the "slope transition point" shown in Figure 2.1. From this elevation, the berms are constructed to slope downward at slopes which may vary from 1V:10H to 1V:40H, until the "cap elevation" of the berm is reached. From the cap of the berm, the levee slopes downward to meet the local ground surface at the "toe" of the levee (also the "berm toe elevation"), usually at a slope of 1V:4H. The elevation change between the cap and the toe may vary from 0.5 to 1.5 meters (1 to 5 feet).

The overall heights of levees from the crown elevation to the toe elevation typically vary between 2.4 to 6.1 meters (8 feet to 20 feet), though greater elevation changes are used. The total area occupied by the levee (in plan view, between the flood

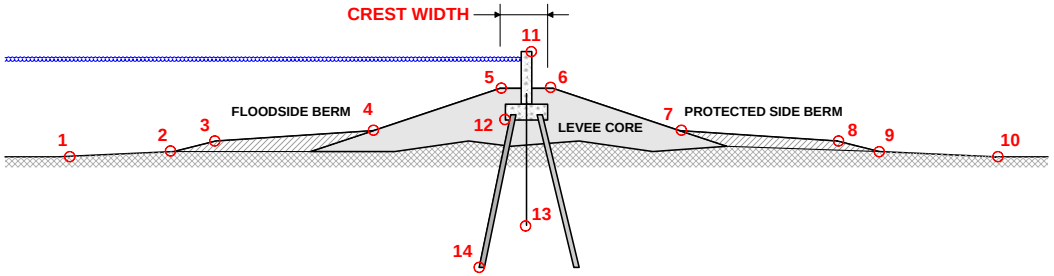

ELEVATIONS (NGVD) AND DIMENSIONS IN METERS FOR LEVEE POINTS IDENTIFIED ABOVE, WITH SLOPES (1V : # H) BETWEEN THESE POINTS.

Levee No.	Point 1	Slope 1-2	Point 2	Slope 2-3	Point 3	Slope 3-4	Point 4	Slope 4-5	Point 5	Crest Width	Slope 5-6	Point 6	Slope 6-7	Point 7	Slope 7-8	Point 8	Slope 8-9	Point 9	Slope 9– 10	Point 10	Point 11	Point 12	Point 13	Point 14
1	X	X	14.5	18.1	-->	-->	14.9	3.0	18.3	3.7	0.0	18.3	3.0	14.9	-->	-->	0.0	14.9	X	X	X	X	X	X
2	X	X	20.7	0.0	-->	-->	20.7	3.5	22.9	3.7	0.0	22.9	3.5	21.0	-->	-->	0.0	21.0	X	X	X	X	X	X
3	X	X	12.5	0.0	-->	-->	12.5	2.5	16.8	9.1	0.0	16.8	2.0	12.3	-->	-->	0.0	12.3	X	X	X	X	X	X
4	X	X	41.5	23.7	-->	-->	42.3	3.0	45.9	4.3	0.0	45.9	3.0	42.2	-->	-->	0.0	42.2	X	X	X	X	X	X
5	X	X	58.6	0.0	-->	-->	58.6	4.0	63.7	4.9	0.0	63.7	5.5	60.7	40.0	58.8	3.0	57.6	X	X	X	X	X	X
6	-1.1	100.0	-0.9	3.0	0.0	14.0	1.2	3.0	5.5	3.0	0.0	5.5	3.0	1.2	14.0	0.0	3.0	-0.9	200.0	-1.2	X	X	X	X
7	-5.6	3.0	-1.2	0.0	-->	-->	-1.2	3.0	0.5	5.0	8.0	1.1	3.0	-1.2	-->	-->	0.0	-1.2	100.0	-1.5	4.3	-0.2	-3.0	X
8	-3.4	3.0	-0.9	0.0	-->	-->	-0.9	3.0	1.1	3.0	0.0	1.1	3.0	-1.5	-->	-->	0.0	-1.5	180.0	-1.7	4.2	0.5	-3.5	X
9	0.0	90.0	1.1	0.0	-->	-->	1.1	3.0	2.7	3.0	0.0	2.7	3.0	0.0	20.0	-0.3	3.0	-0.9	2.7	-2.7	4.6	2.1	-2.4	X
10	X	X	142.6	0.0	-->	-->	141.8	4.0	146.9	3.0	0.0	146.9	5.0	144.1	6.0	142.4	3.0	141.5	X	X	X	X	X	X
11	X	X	143.6	0.0	-->	-->	143.6	4.0	148.0	3.0	0.0	148.0	5.0	145.1	20.0	144.5	3.0	143.6	X	X	X	X	X	X
12	X	X	220.2	0.0	-->	-->	220.2	3.0	230.6	3.0	0.0	230.6	4.0	227.7	65.0	227.4	3.0	225.6	X	X	X	X	X	X
13	X	X	1134.8	0.0	-->	-->	1139.3	3.0	1151.4	4.9	0.0	1151.4	3.0	1139.6	-->	-->	0.0	1139.6	X	X	X	X	X	X
14	X	X	122.7	0.0	-->	-->	122.7	4.0	131.7	3.0	0.0	131.7	4.0	122.0	-->	-->	0.0	122.0	X	X	X	X	X	X
15	X	X	118.2	26.0	--.>	-->	120.0	4.0	124.6	3.0	0.0	124.6	2.7	120.4	-->	-->	0.0	120.4	X	X	X	X	X	X
16	X	X	64.6	0.0	-->	-->	64.6	3.0	66.2	4.6	0.0	66.2	3.0	64.6	-->	-->	0.0	64.6	X	X	X	X	X	X

KEY AND NOTES

1 South Bank, American River
Near Sacramento, California

2 North Bank, Cache Creek
Near Yolo, California

3 East Bank, Feather River
Near Yuba City, California

4 North Bank, Upper Guadalupe River
Near San Jose, California

5 East Bank, Mississippi River
South of Memphis, Tennessee

6 South Lakefront, Lake Pontchartrain
New Orleans, Louisiana

7 East Bank, Metairie Outfall Canal Near Hammond Highway
New Orleans, Louisiana (Breached)

8 East Bank, London Avenue Canal Near Mirabeau Avenue
New Orleans, Louisiana (Breached)

9 East Bank, Inner Harbor Navigation Canal Near Lock
New Orleans, Louisiana (Breached)

10 East Bank, Mississippi River
Near East Hannibal, Illinois (Breached, Hydraulic Fill)

11 West Bank, Mississippi River
Near West Quincy, Missouri (Breached)

12 South Bank, Missouri River
Near Kansas City, Missouri

13 East Bank, Rio Grande
Near El Paso, Texas

14 South Bank, Trinity River
Dallas, Texas

15 East Bank, Wabash River Near Highway 64 Bridge
Near Mount Carmel, Illinois

16 Passaic River
Near Stirling, New Jersey

Figure 2.2 Geometries of Selected Flood Protection Levees and Floodwalls.

Table 2.1
Designated Functions of Levee Berms

TYPE	FUNCTION
Stability Berm	Increases total stresses acting to resist a massively-scaled failure of the levee section toward the protected side or flood side
Seepage Berm	Increases total stresses acting to resist upward components of water seepage through or underneath the levee
Wave Break	Alters the shape of wave forces or water runup on the flood side, and provides resistance to erosion from these waves
Scour Blanket	Provides resistance to scouring erosion of the protected side which may be produced by overtopping
Spoil Bank	Provides a convenient location for the stockpiling of emergency construction materials or excess/unusable earthen materials excavated from the footprint of the levee section

side toe and the protected side toe) is termed the levee "footprint." This footprint and its associated cross-sectional area (A_L) are maintained relatively constant over a given linear distance, termed a "reach."

Primary flood protection levees are typically constructed of compacted earth drawn from locally available sources. The central core of the levees is typically constructed of a silty clay or clay material (classified as "CL" or "CH" in the Unified Soil Classification System). However, to provide cost-effective flood protection, it is often necessary to permit levee construction with other, locally-available materials with which the levee owner has sufficient experience to judge their suitability. Common specifications for levee materials within federally-owned levee systems are shown in Table 2.2.

The material specifications shown in Table 2.2 include two standards. The "ideal" material for levee construction is commonly considered a silty clay. The permeability of silty clay is such that the moisture of the soil (and therefore its form, strength, and resistance to erosion) is relatively easy to control during construction. This high degree of workability ultimately results in a more uniformly-constructed levee section. The relatively low volume-change properties of silty clays do not typically introduce significant problems associated with shrinkage cracking or large-scale internal deformations. The permeability of silty clay further prevents its rapid degradation when inundated, as by a flood.

As mentioned previously, the use of a material other than silty clay is often deemed necessary to provide the advantages gained from using locally available or other readily accessible materials. This fact is reflected in Table 2.2 through inclusion of an expanded range of specifications which may be considered to judge the suitability of materials for use within the levee core. It should be noted that the "common extended ranges or added specifications" are not necessarily applied together. For example, it is unlikely that a material would be required to meet all three of the "added specifications" indicated for gradation. Instead, the material would typically be required to meet one or perhaps two of the added specifications, if at all. Furthermore, it is common for any additional specifications to be imposed upon a small set of material properties. As an

Table 2.2
Specifications for Materials
Within Core Sections of Levees

MATERIAL SPECIFICATION	IDEAL SPECIFICATION	EXTENDED RANGES OR ADDED SPECIFICATIONS
Soil Type, Unified System (USCS)	CL	CH, CL, GC, SC, SP, or SM
Atterberg Liquid Limit w_{LL}	$w_{LL} \leq 35$	$w_{LL} \leq 45$ to 60
Plasticity Index I_P	$10 \leq I_P \leq 25$	$10 \leq I_P \leq 35$
Gradation	Secondary Specification	Percent Sand and Silt ≤ 35 to 60 Percent Silt ≤ 15 to 60 Percent Silt and Clay ≥ 20
Organic Content	Secondary Specification	Percent Organics < 9 to 15
Soil pH	Secondary Specification	$5.5 \leq pH \leq 8.5$

example, the added specifications may include requirements for plasticity index and organic content, but may not include requirements for gradation and pH. Finally, it should be noted that CL, CH, and SC materials are strongly preferred. The inclusion of the additional soil types in Table 2.2 reflects the fact that these soils are often used, though their usage is often restricted to specific zones within the levee or by requirements that these materials be blended with more suitable ones prior to use.

Within the levee core, these materials are typically placed and compacted to create 20-cm (8-in) lifts. Each lift is compacted to a minimum density corresponding to 95 percent of the maximum dry density determined from a "Standard Proctor" laboratory compaction test (Method D698 of ASTM, 2000) relating water content to compacted dry density. When the silty clay is compacted, its moisture content is typically permitted to vary within a small range from the optimum moisture content, perhaps as large as +/-2 percent from the optimum moisture content interpreted from the compaction test.

The optimization of the berm design includes the selection of suitable materials to construct the berms and the development of proper specifications for constructing the berms. If the berm were required to function solely as a protected side stability berm, material specifications for the berm may permit a relatively large variability in material type (as the primary function of such a berm is to provide a counterbalancing weight against forces actuating instability). Construction specifications for protected side berms functioning solely as stability berms may also be more relaxed than those associated with levee core construction. It is common for berms functioning solely as protected side stability berms to be constructed in 30-cm to 38-cm (12-in to 18-in) lifts compacted to at least 90 percent of the maximum dry density from ASTM D698, with no specific requirements on the moisture content of the compacted material. In certain instances, project specifications for berms may require nothing more than conformance to plan dimensions, without compaction control. In these cases, some compaction is typically provided to place and shape the material and to minimize volume losses which might occur prior to measurement of in-place pay quantities. If the berm were required to provide the additional function of resistance to wave-induced or overtopping-induced erosion, the materials and construction specifications would be altered to reflect more stringent requirements associated with this additional function.

It is important to note that the descriptions provided above will not be common to all flood protection levees. Significantly-sized communities within the U.S. are protected by privately-owned levees, for which the construction and maintenance is financed by state-funded or regionally-funded levee districts, or by private development interests. These privately owned levees may or may not be subjected to the same level of rigor in design and construction as the primary flood protection levees described above. This introduces several sophisticated questions related to the party responsible for flooding disasters in which private levees are used to protect large numbers of citizens who may perceive their protection is provided by the federal government. Variations within levee design and construction are currently at the center of efforts to "standardize" levees to the extent possible. Such standardization would presumably form the basis for certifying levees as sufficient to provide specified levels of protection, thereby allowing property protected by the certified levees to be admitted into the National Flood Insurance Program. In any case, this report assumes levees are designed and constructed under the authority of the federal government for the purpose of large-scale flood control.

The community on the protected side of the levee may be represented by a physical area in which water would accumulate during a flood. The drainage boundaries of this area thus define a "polder" and the associated "polder area," A_P, as shown in Figure 2.3(a). The volume of water which would correspond to filling the polder's area to a specified "flood inundation depth," d_I, may be calculated as the product of the inundation depth and the polder area (at that inundation depth).

The "flooding source" is defined by the water levels on the flood side of the levee and by the volume of water available to flood the polder. When a flood source rises to overflow its banks (a "flood stage"), the flood side of the levee experiences a change in total stresses induced by the rising flood waters acting on the levee face. These stresses vary with time, according to the elevation (or "stage") of the flooding source. The pattern of flooding source stage with time is defined by a "flood side stage hydrograph" (FSSH) of the sort shown in Figure 2.3(b). This hydrograph represents the variation of total head on the Flood Side, as would be measured by a floating stream gauge positioned

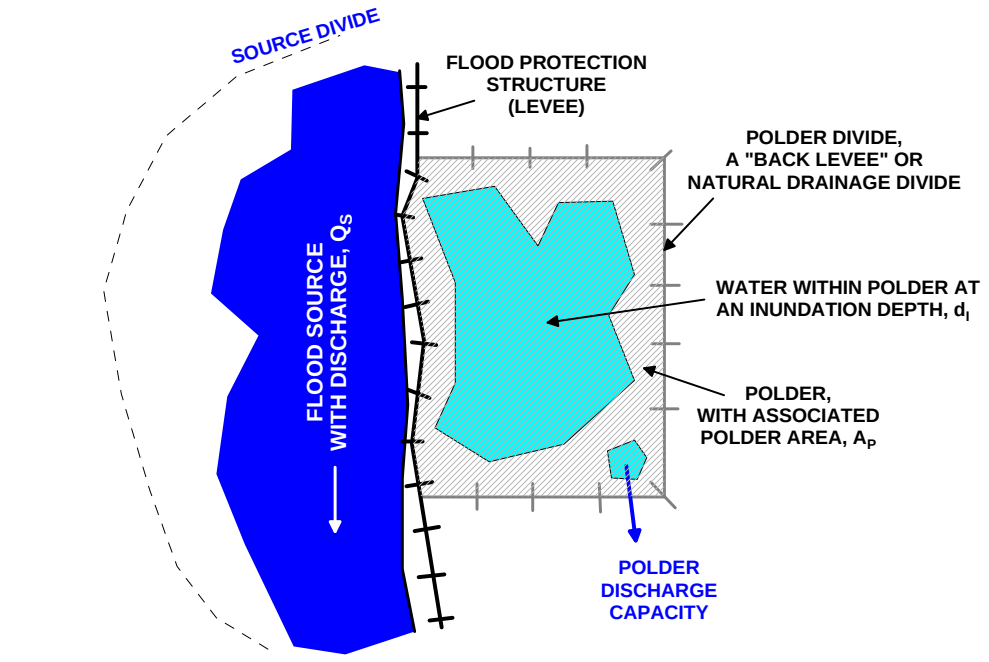

(a)

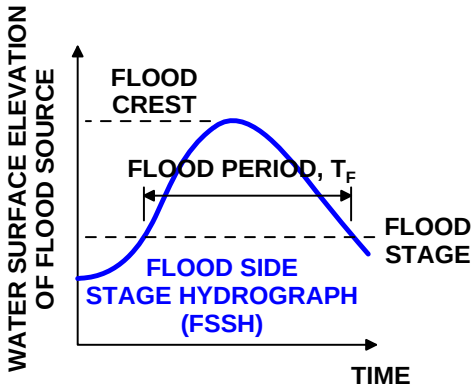

(b)

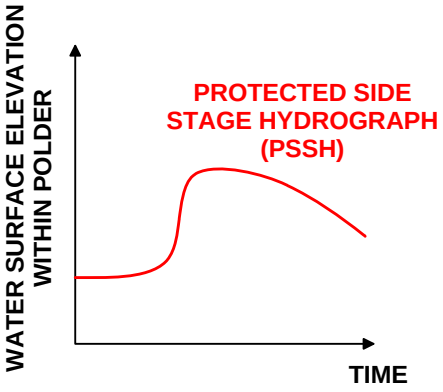

(c)

Figure 2.3 Definitions of Terms Associated with Floods. (a) Delineation of Polder Affected by Flood, (b) Flood Side Stage Hydrograph, and (c) Protected Side Stage Hydrograph.

on that side of the structure. The hydrograph depicts the variation of this total head as a function of time, and the time is most conveniently referenced to the instant at which the flooding source is at its highest elevation (i.e., the "flood crest"). The length of time over which the water surface resides above its flood stage defines the "flood period" (T_F). The

volumetric rate at which water is conveyed downstream by the flood source is measured by the "discharge capacity" (Q_S). While the discharge capacity may be related to the rate at which water flows through a breached levee, the discharge capacity is strictly a function of the flood source.

If a breach were to occur in the levee, water flow from the flood side toward the protected side would act to fill the volume contained within the polder. The rate at which floodwaters would rise within the polder could be defined by a "protected side stage hydrograph" (PSSH), as illustrated in Figure 2.3(c). This hydrograph represents the variation of total head conditions on the protected side of the levee as a function of time. In the event of breaching, this hydrograph is most conveniently referenced to the time at which the breach is initiated.

As shown in Figure 2.4, the flow of water through a breached levee would occur at a volumetric rate defined by the "breach discharge" (Q_D). The breach discharge is different from the discharge capacity (Q_S, defined previously), as the breach discharge quantifies that fraction of the discharge capacity which is flowing into the polder through the breach. The breach discharge occurs through an area defined by the "breach length" (B, a distance along the levee centerline) and the "breach depth (D, a depth at the apparent center of the breach). The discharge would be driven by a change in total head (Δh) from the water surface on the flood side (defined by the elevation, z_F, or by the height of water, h_W) to the water surface on the protected side (defined by the elevation, z_P, or by the tailwater height, h_T). The "breach width" (W_B) indicates that portion of the levee cross-section which has been eroded by the breach. This erosion may extend below the levee section and into the foundation soils, as indicated by the scour depth (d_S). As will be subsequently discussed, partial breaching of the levee (i.e., incomplete removal of the levee section by erosion) creates a weir shape within the levee defined by the breach length, breach depth, and the side slopes of the breached area (m_W).

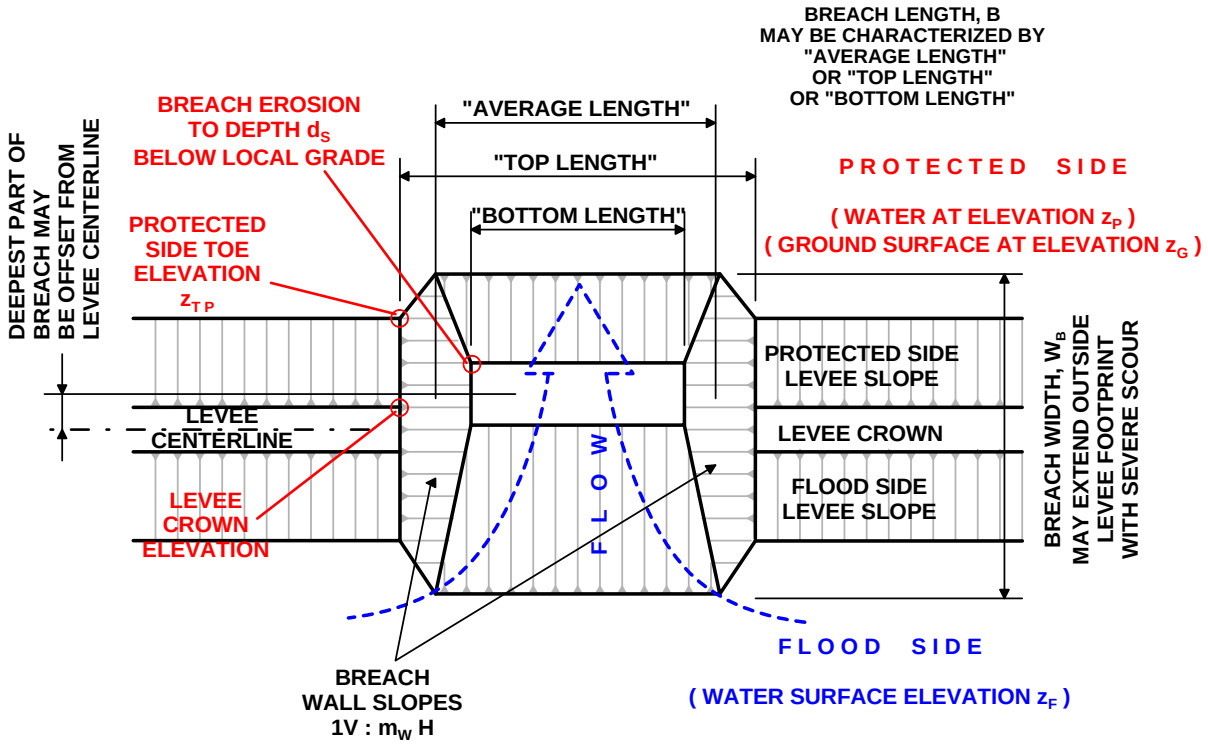

(a)

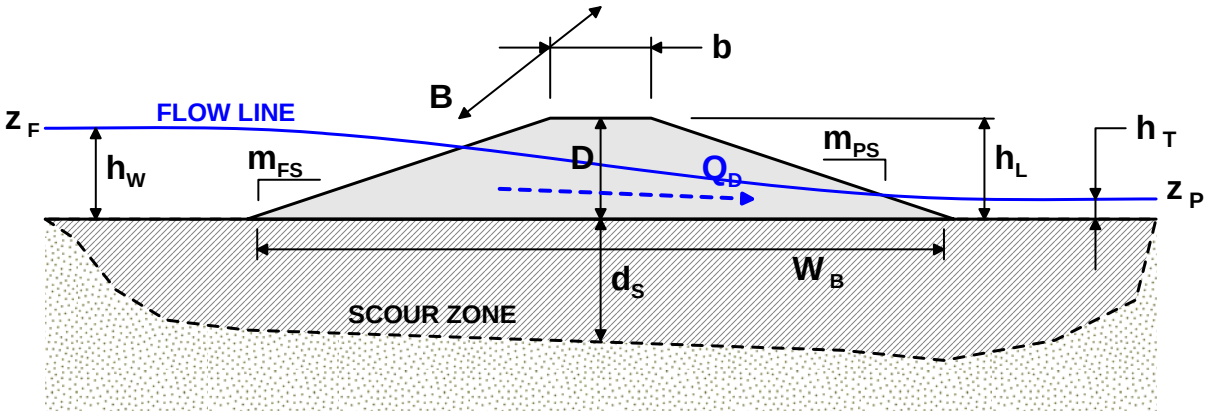

(b)

Figure 2.4 Definitions of Terms Associated with Breaches. (a) Plan View of Breach, and (b) Section View of Breach.

2.3 Considerations Within the Levee Breach Problem

In the event of levee breaching, it may seem obvious that immediate closure of the breach would be desirable. Assuming the source of flooding will continue indefinitely, breach closure would presumably prevent or minimize deeper inundation of the protected community, limit the influx of additional sediment or potential contaminants, and would permit the removal of floodwaters from the flooded community at the greatest possible rate. Furthermore, excluding the possibility of permanently relocating the affected community away from a breached levee, it is often understood that levee breaches will eventually be repaired to restore flood protection to the local community. However, the need to immediately achieve breach closure may be considered within the specific context of the flooding event and the polder being affected by the breach. In fact, it is occasionally desirable to intentionally create or lengthen a breach to provide a measure of protection for a polder downstream of the breach.

The decision to allocate resources to close a levee breach will clearly be influenced by a number of factors unrelated to the physical problem of breach closure (e.g., the availability of human resources, equipment, and closure materials; timely mobilization of these resources to the breach site; the toll of human loss or property loss associated with continued flow through the breach; impacts of breach closure upon the toll of human loss or property loss downstream of the breach; etc.). Assuming the decision is made to attempt breach closure and the resources are available to do so, first responders will likely be most interested in (a) the time available to close the breach, (b) the size of the breach, and (c) any characteristics of the breach that will influence logistics of the closure operations (e.g., flow velocities through the breach may impact equipment operation, rapid growth of the breach may impede the placement of equipment near the breach). The time available to achieve breach closure and the size of the breach may be related, though the two are discussed individually in this report. Operational logistics and safety in the vicinity of the breach (item c) are not explicitly considered in this report.

With regard to the time available to achieve closure (the “breach closure window”), a great deal may be learned by considering the hydrographs associated with

the flooding source and the polder. For riverine floods, the shape of the FSSH is influenced by the temporal and spatial distributions of additional water sources (e.g., meltwater or rainfall) relative to the hydrograph location, the water conduction properties of the ground surface and subsurface, and the interconnectivity and water conduction capacities of tributary streams. The combination of these variables often creates a FSSH which rises and falls at a relatively slow rate, at least for major river flooding events involving river drainage basins of 2500 ha or more.

A tabulation of recent hurricane-based flooding events within the U.S. is provided in Table 2.3. This table presents simplified storm surge patterns drawn from USGS tidal gage data in close proximity to the landfall location of each storm. In most cases, the tidal gage data has not been corrected for the influence of daily tidal cycles, so that the portion of the surge attributable to the storm may include a concurrent rise associated with the daily tidal fluctuation. Table 2.3 is intended to provide a reasonable sense of proportion for hurricane-based flooding events. With the exception of the hydrograph associated with Hurricane Ike, the data for the selected hurricane events indicates the FSSH rises at a rate varying from 20 to 60 cm/hr. Stage hydrographs associated with modeling surge impacts on coastal beach deposits have assumed similar rates of rise and fall (e.g., see Connell, Larson, and Kraus, 2007, wherein rise and fall rates are assumed to equal 25 cm/hr).

Table 2.4 similarly summarizes relevant features of ten selected riverine floods that have occurred within the United States in the past two decades involving drainage basins larger than 2500 ha. With the exception of the Guadalupe River flood, the tabulated events typically involve stage hydrographs which rise at a rate between 1 and 10 cm/hr. The hydrographs for the selected events were further seen to fall at a rate 1 to 3 times the rate of rise. While there are a number of variables affecting the shape of hydrographs for each of these events, Table 2.4 provides a sense of proportion for major riverine floods within the U.S.

While Tables 2.3 and 2.4 are not comprehensive in their analyses of surge patterns, the two tables demonstrate notable differences in the surge patterns of hurricane-borne floods and riverine floods. The stage hydrographs for the selected hurricane-borne floods appear rise and fall much more rapidly, though the ultimate surge

Table 2.3

Condensed Flood Side Stage Hydrograph Data For Several Recent Hurricane-Borne Floods in the United States (extracted from NOAA, 2009)

EVENT	PEAK SURGE (1) (m)	TIDE DIURNAL (m)	STORM PHASE	SURGE Δh (m)	TIME Δt (hrs)	RATE Δh / Δt (3) (cm/hr)
Hurricane Ike Galveston, Texas September 2008	2.9	+/- 0.4	Rise	1.9	25	8
			Fall	2.5	7	36 [0.2]
Hurricane Wilma Everglades City, Florida October 2005	1.7	0.0 (2)	Rise	1.5	4	38
			Fall	1.3	4	33 [1.2]
Hurricane Rita Cameron, Louisiana September 2005	4.1	+/- 0.6	Rise	3.3	10	33
			Fall	2.8	8	35 [0.9]
Hurricane Katrina New Orleans, Louisiana August 2005 (4)	3.5	0.0 (2)	Rise	2.6	8	32
			Fall	1.5	4	37 [0.9]
Hurricane Ivan Perdido Pass, Florida September 2004	2.1	+/- 0.6	Rise	2.1	10	21
			Fall	2.1	12	17 [1.2]
Hurricane Isabel Oregon Inlet, North Carolina September 2003	1.6	+/- 0.5	Rise	1.6	7	22
			Fall	1.3	10	13 [1.7]
Hurricane Opal Panama City, Florida October 1995	2.5	+/- 0.6	Rise	1.5	7	22
			Fall	1.5	9	17 [1.3]
Hurricane Hugo Charleston, South Carolina September 1989	4.3	+/- 0.6	Rise	2.9	5	58
			Fall	3.5	8	44 [1.3]
Hurricane Gloria Sandy Hook, New Jersey September 1985	1.9	0.0 (2)	Rise	1.9	8	24
			Fall	1.9	3	64 [0.4]
Hurricane Camille East Pearl River August 1969 (USACE-SAM, 1970)	2.5	+/- 0.5	Rise	1.8	3	60
			Fall	1.6	13	12 [5.0]

NOTES:
(1) Peak surge is shown for the location of the tidal gage identified in the "Event" column. Peak storm surge for the event may be significantly larger at locations away from available tidal gage stations.
(2) These data sets were previously corrected to remove the influence of tidal variations.
(3) Numbers within braces [#] indicate ratios of surge rise rates to surge recession rates. Numbers greater than unity indicate storm surge recedes over longer times than it rises.
(4) This item extracted from USACE, 2007a.

Table 2.4
Condensed Flood Side Stage Hydrograph Data For Several Recent Riverine Floods in the United States (extracted from USGS, 2009)

EVENT	FLOOD STAGE (m)	EVENT CREST (m)	PEAK FLOW (m^3/s)	FLOOD PHASE	SURGE Δh (m)	TIME Δt (hrs)	RATE $\Delta h / \Delta t$ (1) (cm/hr)
Susquehanna River Waverly, New York June 2006	230.2	233.8	2220	Rise	6.3	96	6.5
				Fall	4.6	139	3.3 [2.0]
Mississippi River Clinton, Iowa April 2001	176.7	178.8	7930	Rise	4.0	504	0.8
				Fall	2.6	540	0.5 [1.6]
Guadalupe River Cuero, Texas October 1998	46.5	53.9	9070	Rise	13.2	72	18.3
				Fall	10.4	168	6.2 [3.0]
Trinity River Crockett, Texas January 1998	55.5	56.8	1790	Rise	11.0	516	2.1
				Fall	5.6	300	1.8 [1.2]
Red River Grand Forks, N. Dakota April 1997	246.0	254.3	3690	Rise	11.4	444	2.6
				Fall	8.5	747	1.1 [2.4]
Ohio River Maysville, Kentucky March 1997	153.0	156.2	16100	Rise	8.1	89	9.1
				Fall	7.1	252	2.8 [3.3]
Sacramento River Colusa, California January 1997	21.3	20.9	1420	Rise	5.3	330	1.6
				Fall	5.3	500	1.1 [1.5]
Willamette River Oregon City, Oregon February 1996	6.0	8.7	11600	Fall	6.0	89	6.8
				Rise	3.3	158	2.1 [3.3]
Arkansas River Derby, Kansas September 1993	389.9	390.9	1200	Rise	3.7	276	1.3
				Fall	3.7	600	0.6 [2.2]
Missouri River Kansas City, Kansas July 1993	225.1	230.3	8200	Rise	8.5	960	0.9
				Fall	7.5	420	1.8 [0.5]

NOTES: (1) Numbers within braces [#] indicate ratios of river stage rise rates to river stage recession rates. Numbers greater than unity indicate longer times are required for a certain change in river stage to recede, when compared to the time over which the same change in river stage developed.

levels may be less than those of riverine floods. Stage hydrographs for hurricane-borne floods appear more symmetrical about their peak stages and recede at faster normalized rates (when recession rate is quantified as a ratio of the rise rate). The FSSH of a hurricane-based flood is affected primarily by the time-dependent distributions of storm surge and wave inundation, and these may occur over a relatively localized geographical area when compared to the drainage basin affected by a major riverine flood. The result is that hurricane-related stage hydrographs may rise and fall relatively quickly, having a flood period on the order of days. In contrast, major riverine floods have flood periods on the order of three to ten weeks (and may often be measured in months).

2.4 A Model Problem

To demonstrate the influence of the flood characteristics upon the breach closure problem, consider the case of a flood-susceptible community shown in Figure 2.5. The community is situated within an 800-ha polder protected by a levee system rising 2.4 m (8 feet) above the local ground surface. The community does not have any forced drainage systems, as may exist from a network of drainage canals and pumping stations. Let us further assume the community is threatened by the passage of a hurricane capable of creating a FSSH defined by a peak storm surge of 2.8 m (9.2 feet) that rises and falls at a rate of 40 cm/hr. Further assume this hydrograph is roughly symmetric about the peak stage, so that the FSSH may be approximated as shown in Figure 2.6(a). For the purposes of demonstration, we will assume the levee system is breached at a time coincident with the advent of the peak storm surge. We will also assume the breach develops to a length of 30 m (98 feet) within an hour, and permits an average discharge of 200 m^3/s (7060 cfs) from the flood source into the polder. Finally, local agencies have determined that an average flood inundation depth of 90 cm within the polder would constitute a worst-case scenario for recovery operations. This sort of "flood elevation" constraint may arise from actuarial evaluations motivated at limiting property damage or catastrophic loss of life. The average flood inundation depth, as used here, represents an acceptable flood storage volume within the polder, and this volume is typically not distributed equally over the polder area.

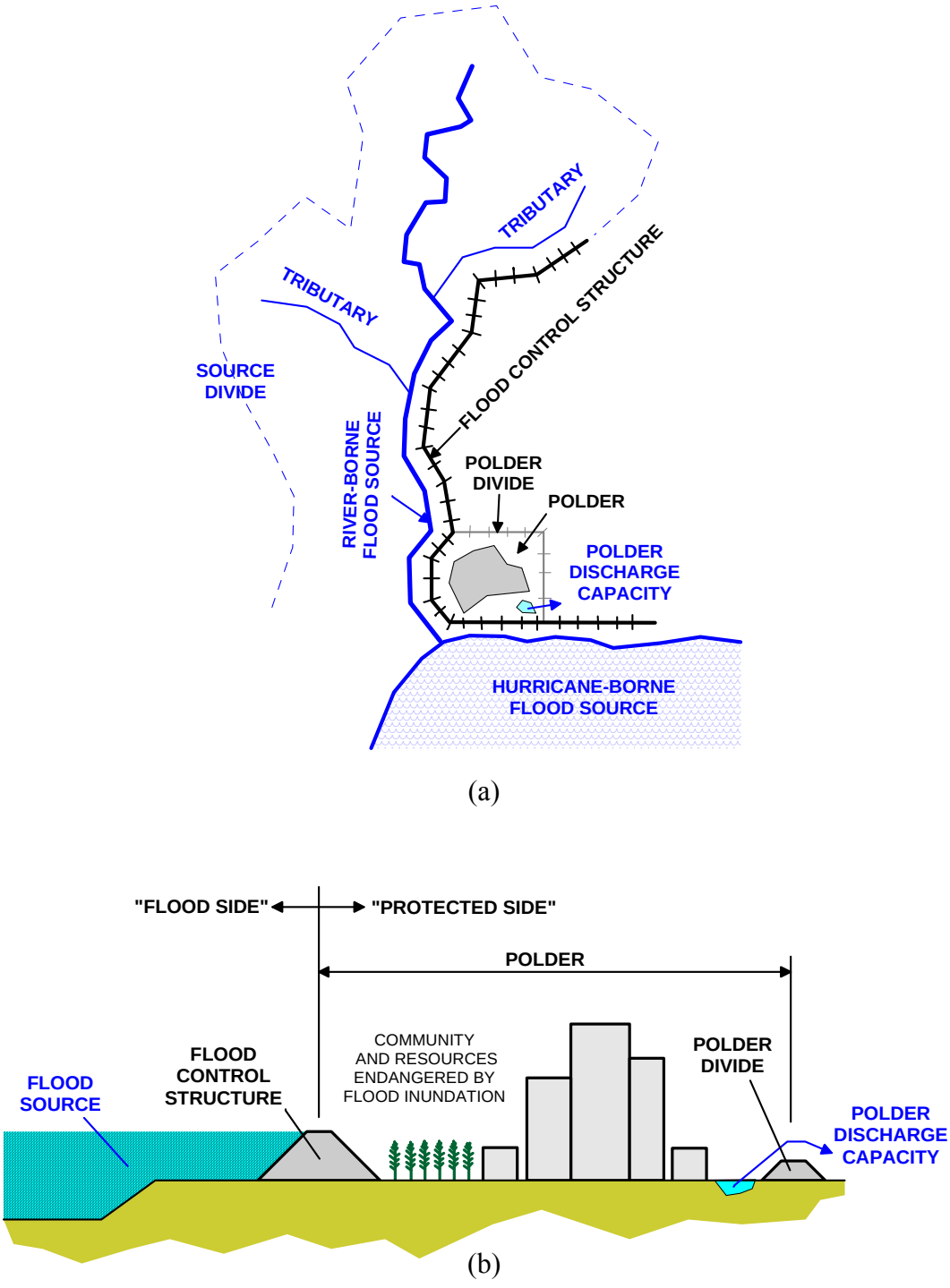

Figure 2.5 Model Problem of a Community Vulnerable to Flood Inundation: (a) Plan View, and (b) Section View.

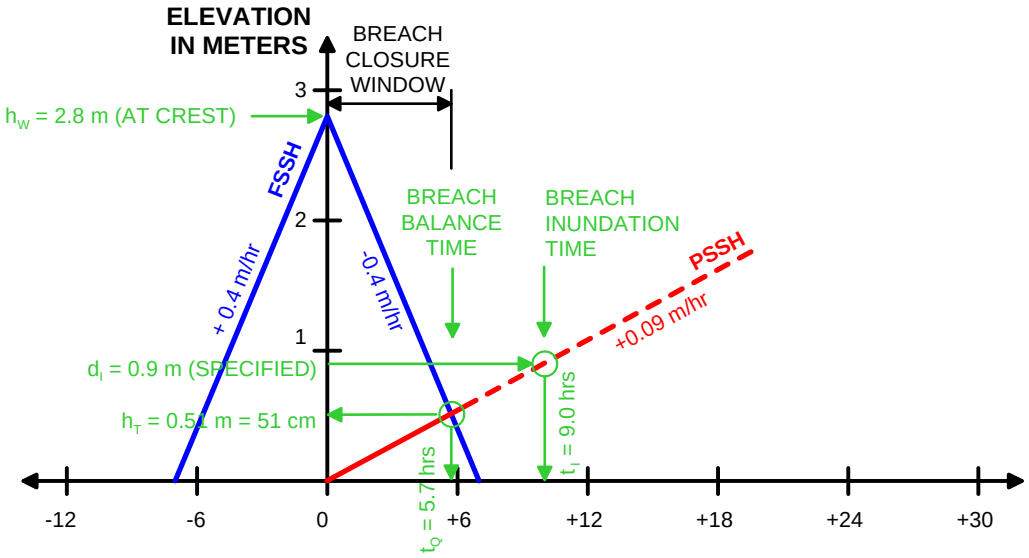

(a)

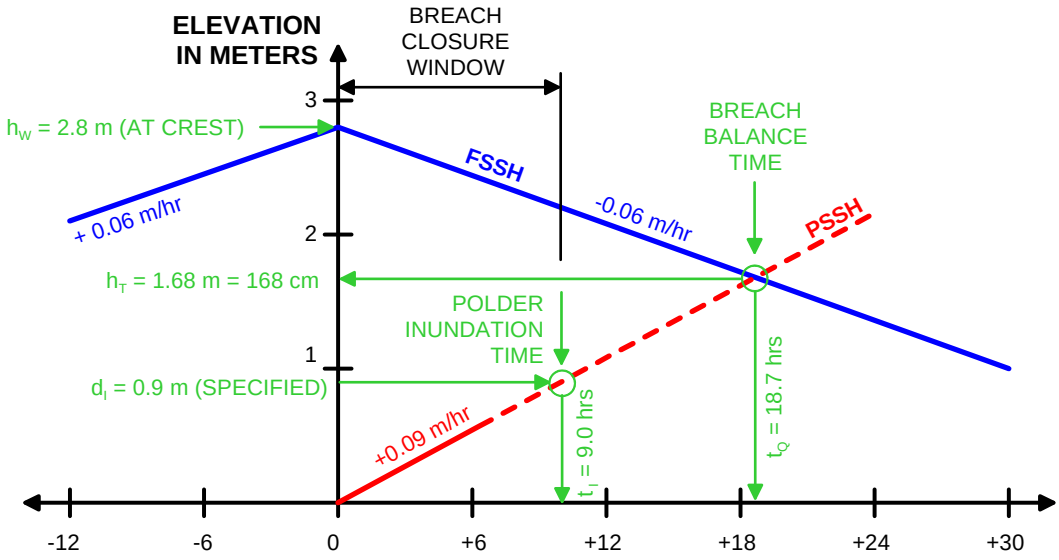

(b)

Figure 2.6 Stage Hydrographs for the Model Problem (a) For a Hurricane-Borne Flood, and (b) a Riverine Flood.

In this example, the breach is described as a fixed size, though subsequent sections of this report will provide some details regarding the evolution of breaches with time. With the breach size estimated, the window of time available to achieve breach closure (termed the "breach closure window" and identified as t_B) must be ascertained. The hydrograph for a small, flat polder may be crudely constructed by dividing the flow rate by the area of the polder. This simple calculation neglects the effects of lag times associated with overland flow of the breach discharge throughout the polder and variations in topography. For the current example, the PSSH would rise at a rate of 9 cm/hr (3.5 in/hr). As shown in Figure 2.6(a), the polder would fill to a level of 51 cm (1.7 ft) within 5.7 hours, just as the storm surge dissipates to the same level. A summary of these calculations is presented in Table 2.5.

In this example, emergency closure of the levee breach must be achieved in roughly five and a half hours to be effective in minimizing the impacts of the storm. If the breach were closed at a time after this window, water within the polder may linger at higher levels than the steadily-lowering water levels outside the polder. Emergency construction of a levee breach closure after the 5.7-hour breach window would effectively inhibit drainage of the polder in the short term (for the greatly simplified assumptions employed here regarding overland flow and polder topography). The intersection of the FSSH with the PSSH illustrated in Figure 2.6(a) thus represents a critical time, here termed the "breach balance time" (t_Q), after which the flow through the breach will reverse directions (moving from the polder toward the flood source).

Differences in polder-averaged stage hydrographs and local stage hydrographs (at specific locations within the polder during flooding) side are attributable to the necessity for the floodwaters to travel overland (through regions with varying topography) to fill the polder. For these reasons, the averaged rate of filling of the polder is a lower bound on the rate of rise for floodwaters within the polder. Localized rates of rise may more closely resemble "flash floods," for which the rate of rise may be one to three orders of magnitude larger than the averaged rate of filling for the polder, depending upon the specific characteristics of the flooding event and the polder. For large polders, the breach balance time is essentially predetermined by the maximum surge height and the rate of fall for that surge. The influences of overland flow and polder topography are greatly

Table 2.5
Calculations of the Breach Closure Window for the Model Problem

VARIABLE		VALUE IN HURRICANE FLOOD	VALUE IN RIVERINE FLOOD
Area of Polder, A_P	=	800 ha	800 ha
Height of Levee, h_L	=	2.4 m	2.4 m
Height of Water, h_W (Surge Height)	=	2.8 m	2.8 m
Rate of Rise, Flood Source	=	0.4 m/hr	0.06 m/hr
Rate of Fall, Flood Source	=	0.4 m/hr	0.06 m/hr
Breach Length, B	=	30 m	30 m
Breach Discharge, Q_D	=	200 m^3/s	200 m^3/s
Breach Failure Time, t_F	=	$t_F = 0$	$t_F = 0$
Flood Removal (Pump) Capacity, Q_P	=	0 m^3/s	0 m^3/s
Limiting Inundation Depth	=	90 cm	90 cm
Rate of Rise Within Polder	=	0.09 m/hr (1)	0.09 m/hr
Breach Balance Time, t_Q	=	5.7 hrs (2)	18.7 hrs
Breach Inundation Time, t_I	=	9.0 hrs (3)	9.0 hrs
Breach Closure Window, t_B	=	5.7 hrs (4)	9.0 hrs
Depth of Water at End of Window	=	51 cm (5)	90 cm

NOTES:

(1) Rate of rise within polder = $(Q_D - Q_P) / A_P$
{ (200 m^3/s) / (8.0 x 10^6 m^3) } x 60 s/min x 60 min/hr x 100 cm/m = 9.0 cm/hr

(2) At balanced condition, water surface elevation at flood source equals water surface elevation within polder:
2.8 m – (0.4 m/hr) x (t_B) = (0.09 m/hr) x (t_B), so that t_B = 5.7 hours

(3) Taken directly from PSSH at 90 cm inundation depth

(4) Lesser of breach balance time and breach inundation time

(5) Depth of water estimated from rate of rise within polder:
(0.09 m/hr) x (5.7 hrs) x 100 cm/m = 51 cm

reduced in this case, and the breach balance time reduces to a problem of waiting for the flood surge to fall below flood stage. For these reasons, the breach closure window estimated by the relatively crude techniques demonstrated here may not differ appreciably from reality, so long as the magnitude of surge and its rate of fall can be reasonably estimated and the breach closure time is governed by the breach balance time.

The existence of a breach balance time is evident in photographs of the floodwall breach at the Inner Harbor Navigation Canal in New Orleans immediately after the passage of Hurricane Katrina. One such photograph is presented in Figure 2.7(a), where water is seen discharging from the flooded Lower Ninth Ward into lower water levels of the Inner Harbor Navigation Canal before the breached floodwall was repaired. While the drainage patterns are more clearly evident in subsequent photos (see the inset to Figure 2.7a), this photograph was selected because it was captured very shortly after passage of the peak surge and the time of the photograph was documented. The photograph was reportedly captured approximately seven hours after occurrence of the peak storm surge (FEMA, 2005; USACE 2007b).

A second sort of constraint on the breach closure window may be imposed by establishing a limiting elevation for water within the polder (or, similarly, a limiting depth of inundation within the polder). The depth of inundation may be used to estimate a "polder inundation time" (t_I) obtained directly from the PSSH. In the case of the hurricane-borne flood problem presented in Table 2.5 and in Figures 2.5 and 2.6(a), the critical depth of inundation (as may be specified by flood mapping, a need to preserve critical facilities, or a need to minimize impact to a highly populated area, for example) was given as 90 cm. From the PSSH, this depth of inundation would occur at a time approximately 10.0 hours after the initiation of the breach if the flood period were long enough to continue the breach discharge into the polder. While the photograph presented in Figure 2.7(a) illustrates the existence of a breach balance time shortly after the passage of peak surge, the water depth in the photograph and in that of Figure 2.7(b) indicate inundation time controlled the breach closure window available in the Lower Ninth Ward polder during Hurricane Katrina.

(a)

Main Photo by Marty Bahramonde (FEMA), Inset by Jocelyn Augustino (FEMA)

(b)

Photo by Marty Bahramonde (FEMA)

Figure 2.7 Views of Floodwall Failures After Passage of Peak Storm Surge: (a) Inner Harbor Navigation Canal of New Orleans on 29 August 2005, 6:45 p.m., and (b) Metairie Outfall Canal (the 17th Street Canal) on 29 August 2005, 6:35 p.m.

The breach closure window (t_B) may be taken as the smaller of the elapsed times defined by (a) the difference between the breach initiation time and the breach balance time, or (b) the difference between the breach initiation time and the polder inundation time. When the breach closure window is limited by the breach balance time, it represents the maximum amount of time available to construct a breach closure so that the closure prevents flood damage that may occur if the flood were allowed to progress at its natural rate. When the breach closure time is limited by the polder inundation time, it represents the maximum amount of time available to construct a breach closure so that the closure provides a specified elevation of flood protection within the polder. For the particular case in which the initiation of breaching is coincident with the peak flood stage, the breach initiation time, t_F, is equal to zero and the breach closure window will equal the breach balance time or the polder inundation time (assuming these two times are referenced to occurrence of the peak flood stage).

A third storm-based constraint upon the breach closure window may be introduced by the presence of the hurricane wind field. Ship cranes are permitted to operate in wind speeds of 25 m/s, or 56 mph (Watson, 2004). However, conventional land-based are typically restricted to operate at wind speeds of approximately 13 m/s (30 mph). In either case, the wind field associated with passage of a hurricane may not provide safe operating conditions for a crane for several hours after the incidence of peak storm surge. This added consideration may further reduce the breach closure window. While consideration of the storm-related wind field introduces further uncertainty in predicting the breach closure window, but the topic is not developed further in this report.

The intense constraints of breach closure within a hurricane-borne flood may easily be verified using the considerable documentation now available for Hurricane Katrina. Figure 2.8 shows interpreted hydrographs for two locations in New Orleans during Hurricane Katrina. The blue-colored hydrograph represents the FSSH for locations near the discharge points of the Metairie Outfall Canal (the 17th Street Canal), the Orleans Avenue Canal, and the London Avenue Canal. These records were interpreted from a mixture of observed stream gauge data, eyewitness accounts, and video/photographic evidence recorded during and after the storm. The purple-colored hydrograph represents approximate conditions on the Flood Side of the city's protection

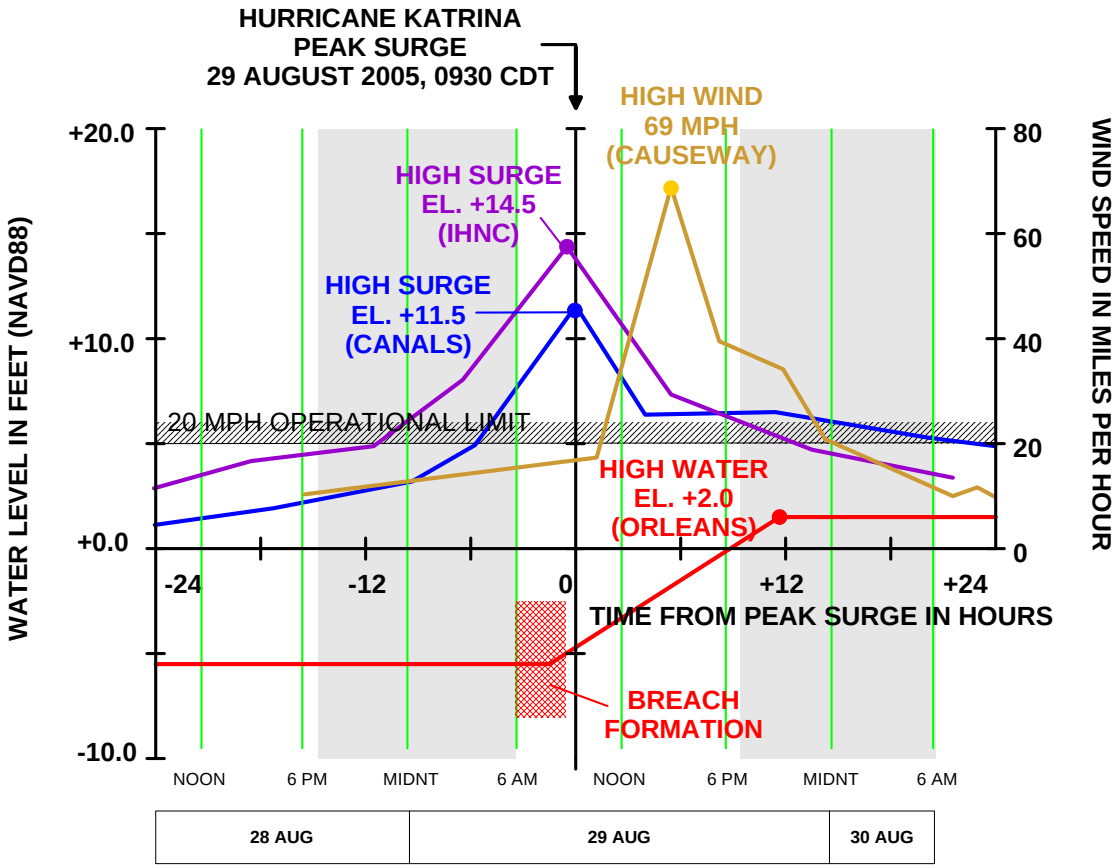

Figure 2.8 Interpreted Hydrographs for Hurricane Katrina (USACE, 2007a).

system near the southern end of the Inner Harbor Navigation Canal, also as interpreted from multiple data sources. Despite the variations in maximum water levels at these locations, both hydrographs show a relatively steep rise and fall of water levels, so that the entire event is associated with a "window" of time which appears to have extended no more than 12 hours from the time at which the peak water levels were observed.

Figure 2.8 further shows the PSSH of floodwaters accumulating within the protected polder of New Orleans due to several breaches. This particular hydrograph was interpreted from eyewitness accounts and observed gauge data in the vicinity of the Orleans Avenue Pumping Station. The PSSH indicates the water level rose approximately 7.5 feet in 12 hours at a relatively constant rate. The Orleans Avenue Pumping Station is located near the center of the polder, and is thus a reasonable representation of average filling of the polder. However, several accounts of more rapid water level rises were reported in the vicinity of the breaches. The difference between the average rate of rise within a polder and the rate of water level rise in the vicinity of a breach is attributable to the rate at which water flows overland within the polder and the overall size of the polder. Large and flat polders, characteristic of many flood-vulnerable areas, will exhibit greater differences between the average rate of water level rise and the rate of water level rise observed in the vicinity of the polder when compared to small and steeply-sloping polders.

Figure 2.8 also includes the history of wind speeds recorded at the center of the Lake Pontchartrain Causeway. To demonstrate the impact of the wind field, an operational limit of 13 m/s (30 mph) has been superposed on the hydrograph data. This operational limit introduces a delay to the time at which a breach closure operation may be initiated in the field. Under the set of constraints including wind speed, breach closure attempts would only be initiated at times later than that associated with maximum flooding. Even with a perfect staging of resources and an instantaneous mobilization of human resources, equipment, and material to the breach site, an attempt at breach closure may have been ineffective (at least for the purpose of minimizing additional flooding from that storm). In the case of Hurricane Katrina, the urgency for breach closure persisted beyond the dissipation of the flood threat, as floodwaters hampered rescue efforts and several additional tropical storms were developing to pose further threats to

the area. The flooding events associated with Hurricane Katrina have provided many valuable lessons regarding the circumstances existing in large, urban floods, but the event can not be considered representative of all flood events. The circumstances associated with a particular flooding event may be largely unique, and the particular amount of time available to achieve closure must be defined by a set of problem-specific parameters. However, this case indicates the time available to achieve breach closure, at least for hurricane-borne floods, may be very small, and could be completely expended within hours of the passage of peak surge levels.

In contrast to the severe time constraints of hurricane-borne flood events, riverine flood events may provide greater opportunities for damage mitigation via breach closure. As a demonstration of this statement, let us consider the case of a riverine flooding event for the same community. The FSSH for the flooding river, illustrated previously in Figure 2.6(b), is taken to rise at a rate of 1.5 cm/hour and fall at a rate of 0.6 cm/hour (0.6 in/hr and 0.24 in/hr, respectively). In this case, we will assume a levee breach develops from overtopping erosion associated with a river crest 0.3 m above the levee crest to initiate the breach. That is, the river crest (and thus, the peak surge) is equal to the sum of the 2.5 m levee height and the 0.3 m overtopping, or 2.8 m (9.2 feet) above local grade. The levee breach is coincident with the river flood crest (so that t_0 is zero, when referenced to the occurrence of peak surge) and again permits a flow of 200 m^3/s (7060 cfs) into the polder. By the same approximation method used for the hurricane-based flood, the PSSH would rise at a rate of 9 cm/hr (3.5 in/hr). In this case, the polder would fill to a level of 261 cm (8.6 ft) over approximately 29 hours, during which time the river stage would fall to the same level. However, inundation within the polder would rise to the specified 90-cm inundation depth within 10 hours, so that the criterion for polder inundation governs the response time. These calculations are summarized in Table 2.5, alongside those presented previously for the hurricane-based flood event.

For the riverine flood in the model problem, emergency responders would have ten hours to achieve breach closure, as compared to the five- to six-hour response timeline associated with the hurricane event. Within the model problem presented herein, the differences in response times are associated with two factors: the characteristic time associated with the flood event (defined by the rate of fall for the flood surge); and the

criteria used to define the maximum tolerable flooding level (i.e., by "breach balancing" or "polder inundation"). In general, the characteristic time for a hurricane-borne event is considerably smaller than the characteristic time associated with a riverine flood (for riverine floods which may affect a large polder). The relatively protracted flood periods of riverine floods may permit sufficient time to preposition flood-fighting resources (though these resources may be dispersed over a fairly large region in riverine flood fights). Finally, riverine floods may not suffer from restrictions on construction operations imposed by high winds.

Differences in the breach closure window associated with various types of floods are illustrated in Table 2.6. This table was developed from the simple, linearized stage hydrograph procedure used in the model problem. Two different flood surge heights were assumed to represent a "high surge" of 3.5 m (11.5 ft) and a "low surge." Two different flood periods were also assumed, corresponding to a "rapid fall" of the peak surge (as may be associated with a hurricane-borne flood) and a "slow fall" of the peak surge (as may be associated with a riverine flood). The rates of stage falling for "rapid fall" and "slow fall" were 30 cm/hr and 2 cm/hr, respectively, and these rates are reasonably representative of hurricane-borne floods and riverine floods (see Tables 2.3 and 2.4).

For each flood surge height and flood period in Table 2.6, three sizes of breaches were considered: a large breach (70 m long), a medium-sized breach (25 m long), and a small breach (10 m long). Flow through each breach was assumed to occur at an average velocity of 3 m/s (10 ft/s) so that the breach discharge could be estimated from the area of the breach (the product of the surge height and the breach length) multiplied by this average velocity. While the instantaneous flow in the vicinity of the breach may vary widely (from 0.5 m/s to 6.0 m/s or more), the assumed velocity of 3 m/s was considered as a reasonable representation of the average velocity across the changing area of the breach over the entire duration of inundation. The characteristics of the polder are also considered in Table 2.6 by inclusion of the polder area. Small, medium, and large polders are represented by 100 ha, 500 ha, and 4000 ha areas being inundated at an

Table 2.6
Breach Closure Windows For Several Combinations
Of Flood Surges, Breach Sizes, and Polder Areas

			Small Polder 100 ha (0.4 mi^2)		**Medium Polder** 500 ha (1.9 mi^2)		**Large Polder** 4000 ha (15.4 mi^2)	
			Shallow Inundation $d_I \le 0.5$ m (1.6 ft)	**Deep Inundation** $d_I \ge 1.5$ m (4.9 ft)	**Shallow Inundation** $d_I \le 0.5$ m (1.6 ft)	**Deep Inundation** $d_I \ge 1.5$ m (4.9 ft)	**Shallow Inundation** $d_I \le 0.5$ m (1.6 ft)	**Deep Inundation** $d_I \ge 1.5$ m (4.9 ft)
High Flood Surge h_W = 3.5 m (11.5 ft)	**Rapid Fall (Hurricane)** 30 cm/hr 12 in/hr)	**Large Breach** B = 75 m (246 ft)	1.1 hrs 0.2 hrs **0.2 hrs**	1.1 hrs 0.5 hrs **0.5 hrs**	4.0 hrs 0.9 hrs **0.9 hrs**	4.0 hrs 2.6 hrs **2.6 hrs**	9.4 hrs 7.1 hrs **7.1 hrs**	9.4 hrs 21.2 hrs **21.6 hrs**
		Medium Breach B = 25 m (82 ft)	2.8 hrs 0.5 hrs **0.5 hrs**	2.8 hrs 1.6 hrs **1.6 hrs**	7.2 hrs 2.6 hrs **2.6 hrs**	7.2 hrs 7.9 hrs **7.2 hrs**	10.2 hrs 21.2 hrs **10.2 hrs**	10.2 hrs 63 hrs **10.2 hrs**
		Small Breach B = 12 m (40 ft)	4.6 hrs 1.1 hrs **1.1 hrs**	4.6 hrs 3.3 hrs **3.3 hrs**	9.0 hrs 5.5 hrs **5.5 hrs**	9.0 hrs 16.5 hrs **9.0 hrs**	11.2 hrs 44 hrs **11.2 hrs**	11.2 hrs 132 hrs **11.2 hrs**
	SlowFall (Riverine) 2 cm/hr (0.8 in/hr)	**Large Breach** B = 75 m (246 ft)	1.2 hrs 0.2 hrs **0.2 hrs**	1.2 hrs 0.5 hrs **0.5 hrs**	6.0 hrs 0.9 hrs **0.9 hrs**	6.0 hrs 2.6 hrs **2.6 hrs**	39 hrs 7.1 hrs **7.1 hrs**	39 hrs 21.2 hrs **21.2 hrs**
		Medium Breach B = 25 m (82 ft)	3.6 hrs 0.5 hrs **0.5 hrs**	3.6 hrs 1.6 hrs **1.6 hrs**	16.7 hrs 2.6 hrs **2. 6 hrs**	16.7 hrs 7.9 hrs **7.9 hrs**	88 hrs 21.2 hrs **21.2 hrs**	80 hrs 63 hrs **63 hrs**
		Small Breach B = 12 m (40 ft)	7.4 hrs 1.1 hrs **1.1 hrs**	7.4 hrs 3.3 hrs **3.3 hrs**	32 hrs 5.5 hrs **5.5 hrs**	32 hrs 16.5 hrs **16.5 hrs**	112 hrs 44 hrs **44 hrs**	112 hrs 132 hrs **132 hrs**
Low Flood Surge h_W = 1.0 m (11.5 ft)	**Rapid Fall (Hurricane)** 30 cm/hr (12 in/hr)	**Large Breach** B = 75 m (246 ft)	0.9 hrs 0.6 hrs **0.6 hrs**	0.9 hrs 1.9 hrs **0.9 hrs**	2.2 hrs 3.1 hrs **2.2 hrs**	2.2 hrs 9.3 hrs **2.2 hrs**	3.1 hrs 25 hrs **3.1 hrs**	3.1 hrs 75 hrs **3.1 hrs**
		Medium Breach B = 25 m (82 ft)	1.7 hrs 1.9 hrs **1.7 hrs**	1.7 hrs 5.6 hrs **1.7 hrs**	2.8 hrs 9.3 hrs **2.8 hrs**	2.8 hrs 28 hrs **2.8 hrs**	3.3 hrs 74 hrs **3.3 hrs**	3.3 hrs 222 hrs **3.3 hrs**
		Small Breach B = 12 m (40 ft)	2.3 hrs 3.9 hrs **2.3 hrs**	2.3 hrs 11.6 hrs **2.3 hrs**	3.1 hrs 19.3 hrs **3.1 hrs**	3.1 hrs 58 hrs **3.1 hrs**	3.3 hrs 154 hrs **3.3 hrs**	3.3 hrs 463 hrs **3.3 hrs**
	Slow Fall (Riverine) 2 cm/hr (0.8 in/hr)	**Large Breach** B = 75 m (246 ft)	1.2 hrs 0.6 hrs **0.6 hrs**	1.2 hrs 1.9 hrs **1.9 hrs**	5.5 hrs 3.1 hrs **3.1 hrs**	5.5 hrs 9.3 hrs **5.5 hrs**	25 hrs 25 hrs **25 hrs**	25 hrs 75 hrs **25 hrs**
		Medium Breach B = 25 m (82 ft)	3.4 hrs 1.9 hrs **1.9 hrs**	3.4 hrs 5.6 hrs **3.4 hrs**	13.5 hrs 9.3 hrs **9.3 hrs**	13.5 hrs 28 hrs **13.5 hrs**	37 hrs 74 hrs **37 hrs**	37 hrs 222 hrs **37 hrs**
		Small Breach B = 12 m (40 ft)	6.7 hrs 3.9 hrs **3.9 hrs**	6.7 hrs 11.6 hrs **6.7 hrs**	21.8 hrs 19.3 hrs **19.3 hrs**	21.8 hrs 58 hrs **21.8 hrs**	43 hrs 154 hrs **43 hrs**	43 hrs 463 hrs **43 hrs**

times shown in blue text indicate elapsed time associated with breach balance time, t_Q
times shown in green text indicate elapsed time associated with polder inundation time, t_I
times shown in **boldfaced black** text are the lesser of these two times, and thus the breach closure window, t_B

average rate defined by the polder size and the breach discharge into the polder. Inundation limits of 0.5 m (1.6 ft) and 1.5 m (4.9 ft) were assumed to represent conditions of "shallow inundation" and "deep inundation."

The simple analyses collected in Table 2.6 qualitatively illustrate the various influences upon the breach closure window. These analyses are presented without the benefit of a complete discussion of the underlying rationale associated with the selected breach sizes, breach discharges, hydrograph characteristics, etc. These factors are discussed in subsequent sections of this report.

2.5 The Mechanics of Levee Breaches

The simplistic discussions of levee breach behaviors presented in the prior section of this report hint at the complexity of levee breach behaviors. In general, the geometry of a levee breach may be affected by more than a dozen factors, as shown in Table 2.7. The large number of variables influencing the breach geometry hints at the complexity of the breach development problem and the unique nature of each breach. Each of the parameters identified as an influencing factor may, in turn, be affected by its own set of uniquely varying parameters. For example, the strength of the levee in resisting erosive effects of breach flows has been demonstrated to be a function of the dominant grain-size of the levee material, the interparticle friction of the material, the permeability and pore water characteristics, the homogeneity of the material in the levee section, and the degree of compaction achieved in the material during levee construction.

In addition, the possibility exists that the relative importance of one or more of the variables shown above may be altered by the values of another variable, so that the geometry of a levee breach may changed radically during its history through changes in the interdependent variables governing its geometry. While ongoing research seeks to clearly define the roles of these various parameters in determining breach geometry, these roles are poorly understood at present.

Table 2.7
Factors Influencing Flow Through a Levee Breach (Q_D)

FACTOR	SYMBOL(S)	INFLUENCE
Flood Surge Height	h	Greater flood height increases flow through breach. Greater velocities of flow associated with higher surge height contribute to greater rates of levee erosion.
Flood Period	T_F	Longer flood period increases flow through breach.
Stream Discharge	Q_S	Greater stream discharge permits greater flow through breach.
Elapsed Time	t	Greater elapsed time (measured from breach initiation) permits greater flow through breach.
Breach Size	B, D, m_S	Larger breach permits greater flow through the breach.
Sediment Concentration	C_S	Greater sediment concentration in breach discharge is thought to decrease the rate at which the eroded levee materials may be transported, thereby decreasing flow through the breach (though this is poorly understood).
Slope of Breach	S	Greater slopes through the breach increase flow through the breach.
Levee Geometry	W_B, b, m_F, m_P	Larger levee footprints reduce the rate at which the breach grows, thereby reducing flow through the breach.
Levee Strength	c, □, τ_S, u, u_S	Greater levee strength reduces the rate of levee erosion, thereby reducing the flow through the breach. In addition, vegetation appears to contribute significantly to minimizing erosion.
Tailwater Height	h_P	Greater tailwater heights reduce flow through the breach.
Polder Area	A_P	Smaller polder areas flood quickly, but contain the influence of the breach discharge and minimize breach development.
Polder Topography	none	Gently sloping polders cause the generation of tailwater effects, thereby reducing the flow through the breach.

Several models have attempted to incorporate various combinations of these factors to describe the geometry of breaches developing in earthen levees and dams. These models have historically developed as empirical approximations to observed behaviors of the levees and dams during breaching. Even in cases of models developed from first principles, a degree of empirical data is often introduced regarding the shape of the breach (e.g., the ratio of its length to height). For this reason, observations and physical measurements made during actual levee breaches are critical to understanding the process of levee breaching and its simulation with currently available tools. These observations include studies involving full-scale breaches, large scaled models of breaches, and smaller laboratory-scale models.

Research regarding experimental observation and prediction of levee and dam breaches is highly active and dispersed among a variety of governmental agencies, universities, and private corporations. However, the most significant volumes of current research regarding breach development appear concentrated at five locations: the United States Department of Agriculture's Agriculture Research Service Hydraulic Engineering Center (ARS-HEC); the United States Army Corps of Engineers Engineering Research and Development Center (USACE-ERDC); the United States Bureau of Reclamation (USBR); the Deltares Hydraulics Laboratory (formerly known as the Delft Hydraulics Laboratory and abbreviated here as "DHL"); and H.R. Wallingford Ltd, in Wallingford, England. These five entities collaborate under a cooperative agreement between the United States Association of Dam Safety Officials and the European Union Dam Safety Office (Hanson and Temple, 2007).

Prior research regarding dam failures indicates earthen dams are most likely to fail from overtopping and subsequent external erosion of the dam material or from "internal erosion" processes through which excessive seepage gradients remove dam materials to create cavities (Foster et al, 2000). These two general sources of failures have been found to account for approximately 85 percent of large embankment dam failures. Current research efforts within the USACE to calibrate failure probabilities of earthen levees have found these two mechanisms are likely the most significant contributors to levee failures, as well (Sills, 2009).

Conclusive descriptions of the processes thought to be associated with internal erosion are elusive, as observation of the phenomenon is inherently difficult. In contrast, the observation of external erosion is relatively straightforward and may provide insight into the processes associated with both internal and external erosion. External erosion may begin from any of several processes (Powledge et al, 1989): the development of turbulence fields at the protected side slope transition point, the occurrence of critically high velocities on the protected side slope, the plunging of a jet created as the floodwater crosses the levee crown, or the first occurrence of high scouring velocities along the levee crest. Once scouring is initiated, it may grow by deepening to a scour trench or it may appear as a hole on the downstream levee face. Shortly after the initiation of scour, a vertical drop will be evident, and cascading water will form a localized jet in the vicinity of the scour pit which acts to expand the scour hole. The scour hole grows by progressive movement upslope (toward the flood side) with a simultaneous expansion of its width parallel to the levee alignment. The upward growth of the scour hole is a convenient measure to describe the stages of breach development.

The results of two studies of levee breach development are shown in Figure 2.9. In each of these studies, scaled physical models of levees were subjected to constant overtopping. The study in Figure 2.9(a) employed a laboratory-scale levee constructed within a hydraulic flume (Zhu et al, 2006). The results shown in Figure 2.9(b) were obtained from a 1:4 scale embankment constructed adjacent to an outdoor reservoir (Hanson et al, 2005). In each study, the cross-sections of the eroding levees were measured at several times during the overtopping. The time at which the erosion progressed to the flood side of the levee crown was taken as a critical point in the erosion process, identified as the time to failure (t_F) on Figure 2.9. The levee cross-sections shown in Figure 2.9 were then referenced to these failure times. The progress of erosion shown in Figure 2.9 has been confirmed in several additional studies (see, for example, Pugh, 1985; Davletshin, 2001; Visser et al, 2006).

On the basis of the physical observations shown in Figure 2.9(a), the DHL team developed a system to describe the stages of levee breach development associated with overtopping of levees and subsequent erosion of the levee section (Visser et al, 2006).

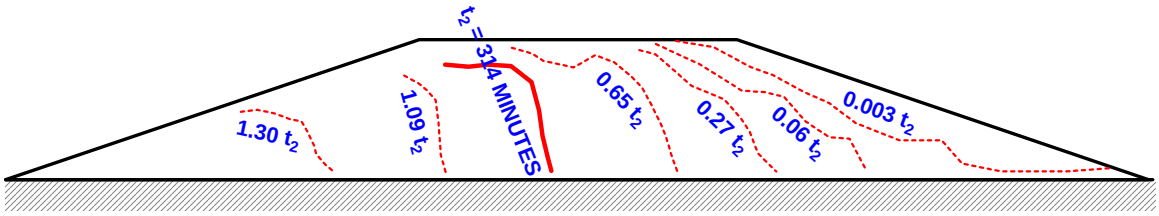

(a)

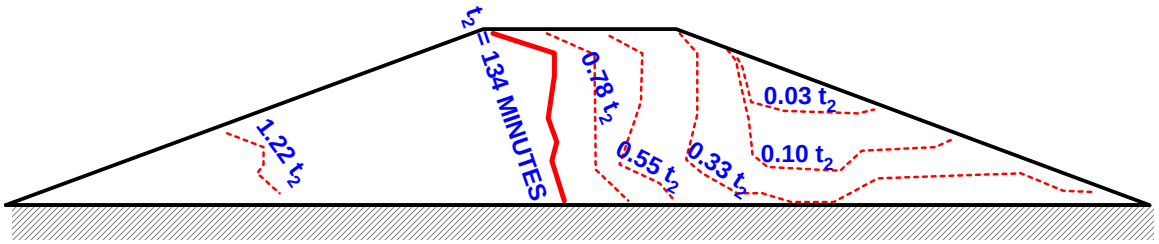

(b)

Figure 2.9 Observations of Breach Formation and Development in Physical Models (a) at Laboratory Scale of 1:30, and (b) at Field-Constructed Scale of 1:8.

These stages of breach development have generally been adopted in the U.S. and E.U., and they are summarized in Figure 2.10. The systematic description shown in that figure was initially developed to describe breaches initiated by levee overtopping from a constant head flood surge. However, analogous stages of breach evolution may also be identified in breaches initiated by underseepage or through-seepage, as shown in Figure 2.11.

In Stage 1 of breach development for overtopping (see Figure 2.10), the downstream face of the levee is being eroded. When the scour hole has progressed to meet an imaginary vertical plane coincident with the protected side of the levee crown, the scour is said to move from Stage 1 into Stage 2. In Stage 2, erosion continues in much the same manner as Stage 1, but a large, sheer vertical face is often present in the cross-section. The eroding levee begins to resemble a broad-crested weir with a drop on the downstream face. Growth of the scour hole continues until this sheer face encounters the vertical plane coincident with the flood side edge of the levee crown. A levee section which exists in Stage 1 or Stage 2 of erosion is obviously in danger of subsequent failure. However, in these two stages, the levee section continues to provide some resistance to flow through the breach, as floodwaters must overcome the weir height defined by the original levee crown elevation.

The mechanisms driving erosion in Stages 1 and 2 appear to be largely driven by high shear stresses imparted by high flow velocities and momentum changes associated with slope transitions or water jets falling into the levee section over its crown. The progress of these mechanisms is typically estimated by conventional scour equations developed in sediment transport modeling. Ongoing studies of these scour mechanisms have focused on the role of impinging jets on the generation of locally high turbulent velocities which would contribute to erosion of the section. Additional research has focused on the additional resistance to erosion that is provided by vegetation or soil treatments on the downstream face of the levee. Finally, a third research thrust has developed to investigate the influences of compaction water content, wetting front migration, and soil suction upon the erosion resistance of soils forming the levee.

As the levee section is further eroded into Stage 3, the eroding scour pit develops a higher degree of “connection” with the flood source, and the remainder of the levee

STAGE 0

BREACH INITIATION FROM INTACT LEVEE SECTION

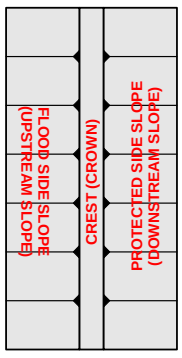

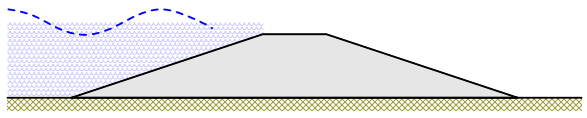

Photo by Dallas Flood Control District

STAGE 1 EROSION

PROGRESSION ON PROTECTED SIDE OF LEVEE

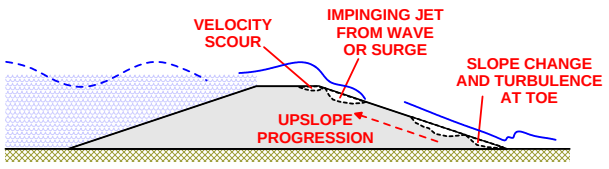

Photo by Cyndi Beanblossom

END OF STAGE 1

EROSION HEADCUT REACHES LEVEE CROWN ON PROTECTED SIDE

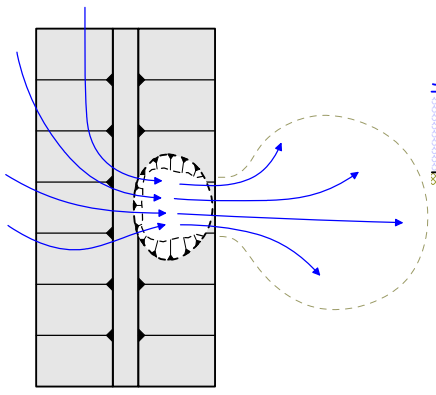

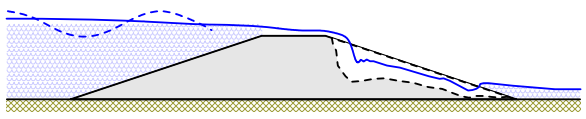

Photo by Chris Saucier

STAGE 2 EROSION

PROGRESSION TOWARD DIRECT CONNECTION WITH FLOOD SOURCE

END OF STAGE 2

BREACH IS DIRECTLY CONNECTED TO FLOOD SOURCE

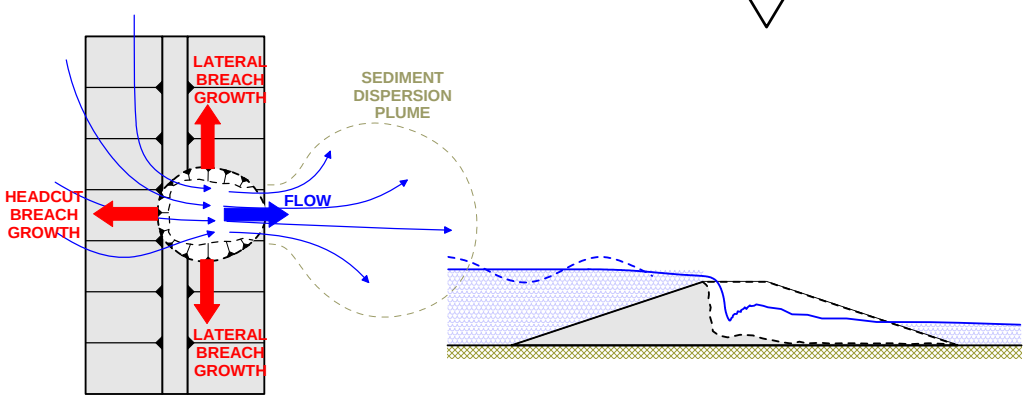

Photo Source Unknown

Photo by Brent Perrot

STAGE 3 EROSION

REMOVAL OF FLOOD SIDE LEVEE SECTION

END OF STAGE 3

LEVEE SECTION EFFECTIVELY ERODED, FLOW THROUGH BREACH IS UNIMPEDED

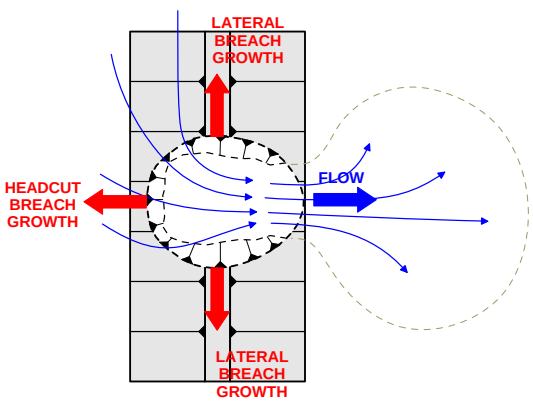

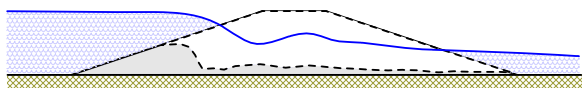

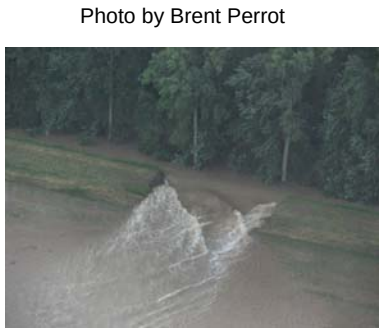

Photo by Brent Perrot

STAGE 4 EROSION

GROWTH OF BREACH PARALLEL TO LEVEE ALIGNMENT

END OF STAGE 4

BREACH GROWN TO MAXIMUM EXTENT

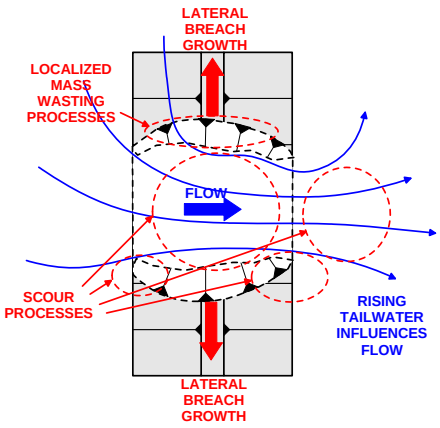

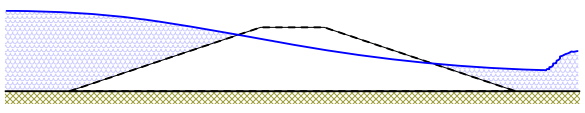

Photo by Dean Lockhart

Photo by George Sills

Figure 2.10. Stages of Breach Growth Sequence for Breaches Initiated by Overtopping (after Hanson, Cook, and Hunt, 2005).

STAGE 0

BREACH INITIATION FROM INTACT LEVEE SECTION

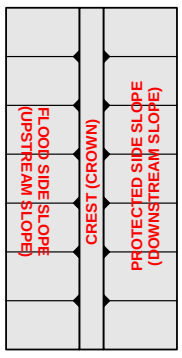

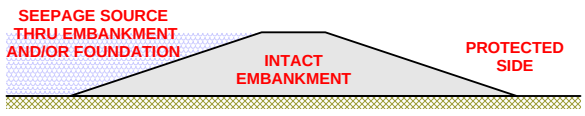

Photo by Dallas Flood Control District

STAGE 1 EROSION

PROGRESSION ON PROTECTED SIDE OF LEVEE

Photo from FEMA, 2005

END OF STAGE 1

EROSION PIPE ENCROACHING UPON LEVEE CROWN

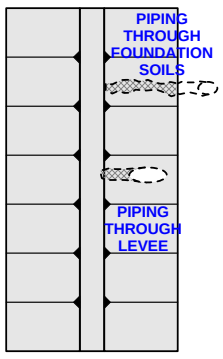

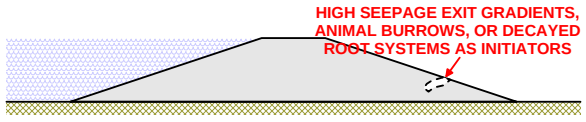

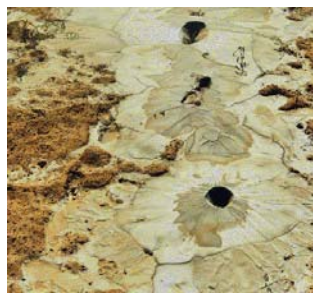

Photo by Richard Barnitz

STAGE 2 EROSION

PROGRESSION TOWARD DIRECT CONNECTION WITH FLOOD SOURCE

Photo by USACE-MVM

END OF STAGE 2

EROSION PIPE BECOMES DIRECTLY CONNECTED TO FLOOD SOURCE

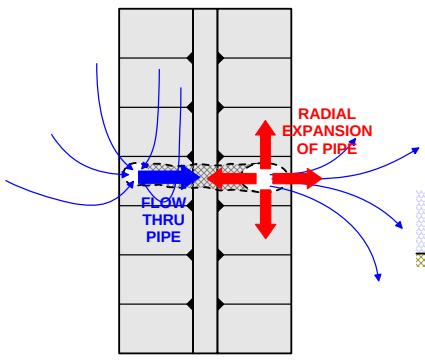

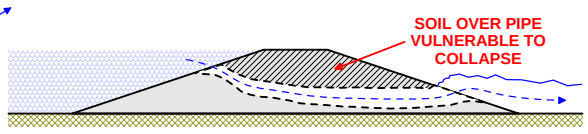

Photo by KCBS-2 TV, Los Angeles

STAGE 3 EROSION

COLLAPSE OF SOIL OVER SEEPAGE PIPE AND RAPID REMOVAL OF LEVEE SECTION

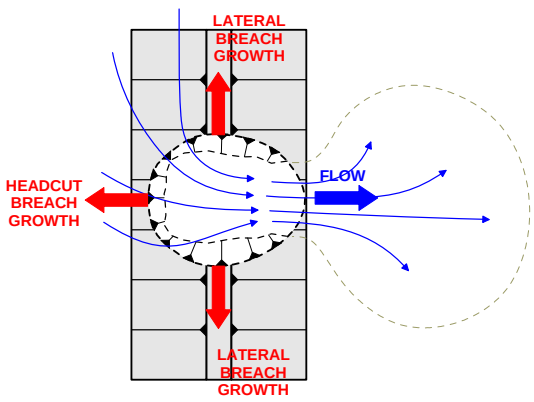

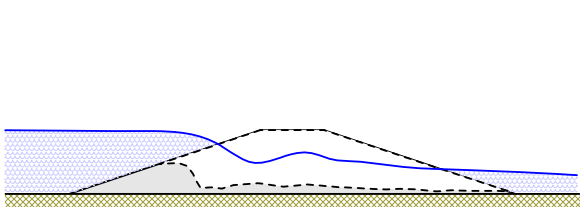

Photo by KCBS-2 TV, Los Angeles

END OF STAGE 3

LEVEE SECTION EFFECTIVELY ERODED, FLOW THROUGH BREACH IS UNIMPEDED

STAGE 4 EROSION

GROWTH OF BREACH PARALLEL TO LEVEE ALIGNMENT

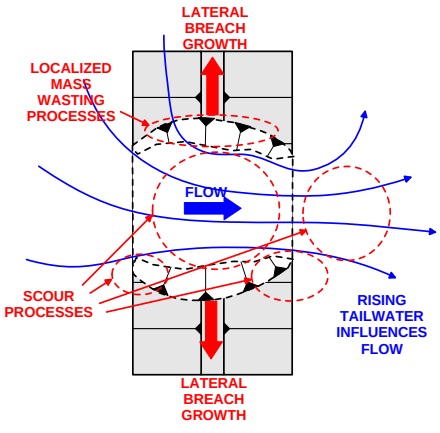

Photo by California Department of Water Resources

END OF STAGE 4

BREACH GROWN TO MAXIMUM EXTENT

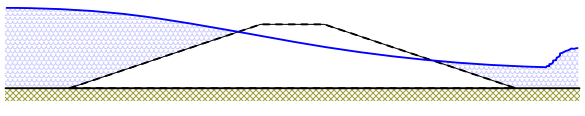

Photo by California Department of Water Resources

Figure 2.11. Stages of Breach Growth for Breaches Initiated by Piping.

cross-section is eroded during this stage. At the end of Stage 3, flow through the levee becomes unabated. The progress of erosion during Stage 4 is one of expansion of the breach (increasing length of the breach along the levee's alignment centerline). In Stage 4, the levee section is typically completely eroded entirely across the former cross-section for the entire length of the breach, though some researchers have noted that a small portion of the levee section may remain near the levee flood side toe throughout the erosion process, including Stage 4 (Nagy, 2006). The flow-diminishing effects of this small "bench" at the flood side toe of the former levee section are negligible.

The transition from Stage 2 to Stage 3 may be marked by a change in the geometric proportions of the levee breach. Prior to Stage 3, the width of the breach appears to be reasonably proportional to the drop height through the breach (in Figure 2.4, the breach width "B" is proportional to the breach depth "D"). However, with the onset of Stage 3 and the effective removal of the levee section, the breach appears to lengthen so that the proportions between breach length and breach depth change considerably with time. The nature of these changes have not been clearly captured and described to date, so that certain simplifying assumptions regarding the breach geometry (e.g., a relationship between the ratio of breach length to depth as a function of time) are often retained.

The processes at work to grow the breach during Stage 3 may also differ somewhat from those present during Stages 1 and 2. Erosive growth of the breach in its early stages appears to be largely dominated by local scour processes in which tractive stresses applied by the flowing water exceed shearing resistance between soil grains at the exposed levee surface. In concept, a "grain-by-grain" removal of the levee material results, though the erosion may occur by the removal of flocculated groups of particles in the case of fine-grained soils (McAnally and Mehta, 2001). After Stage 2, however, this local scour mechanism appears to be supplemented by significant contributions from mass wasting processes.

Observations of scale models indicate that breach growth in Stages 3 and 4 is largely affected by the removal of large blocks of the levee section in addition to ongoing scour mechanisms. These blocks spall from the levee section into the flow and are subsequently broken down and transported through the breach. The blocks appear to fail

into the breach along rupture surfaces that appear much like those which would be predicted from conventional slope stability analyses. The mechanisms at work include the release of total horizontal stresses, strain-softening of brittle compacted materials, and the release of soil suction acting (the release of which contributes to a loss of strength along a potential failure surface). The role of advancing wetting fronts and associated release of soil suction in these failures is a subject of current research and may be the dominant process in breach growth in Stages 3 and 4.

The shape of the eroded levee section in Stages 3 and 4 has led to the common characterization of the breach discharge in terms of weir equations during these stages. As illustrated in Figure 2.12, the flow pattern through a levee in Stage 3 erosion closely resembles that of a compound, broad-crested weir. Similarly, Figure 2.13 illustrates a likeness between a levee in Stage 4 erosion and the flow patter through weir representations of spill-through abutments. The close resemblance between the eroded levee section and the familiar concept of a weir has led to the inclusion of weir equations in many breach growth models (Wahl, 1998; Fritz and Hager, 1998).

The water flowing through a breach may be represented by a breach discharge hydrograph of the sort shown in Figure 2.14. In theory, the time associated with a given size of levee breach includes two components, the magnitudes of which are related to the mechanics of breaching described above. First, there is the "time to failure" (t_F), representing the time over which the failure itself developed from the first indications of breach initiation (visual or otherwise) to the point at which the breach is fully developed via direct connection with the flood source. Second, there is the elapsed time beyond this initial "time to failure."

According to the descriptions of levee breaching stages provided, the eroding levee becomes "directly connected" to the flood source at the end of Stage 2. The transition from suppressed flow to free flow through the breach, corresponding to the end of Stage 2 is clearly identifiable in breach discharge hydrographs observed during laboratory and field-scale physical model experiments. Because of the rapid degradation of the dam or levee section after this point and the commensurately rapid increase in breach discharge, the end of Stage 2 erosion is commonly taken as a critical marker of

(a)

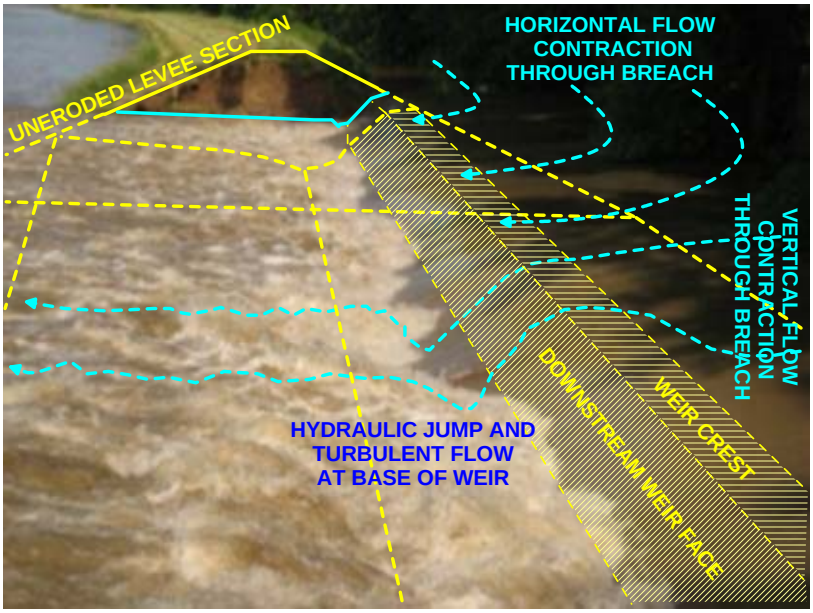

(b)

Figure 2.12 Conformance of Developing Breach to Shape of Hydraulic Weir: (a) Unmodified Photograph by Cyndi Beanblossom, and (b) With Weir Shape Superposed.

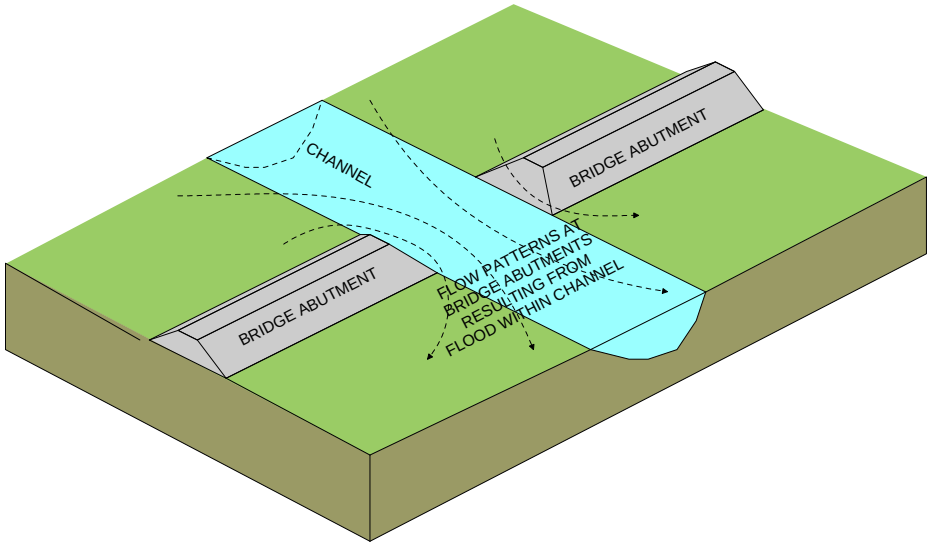

(a)

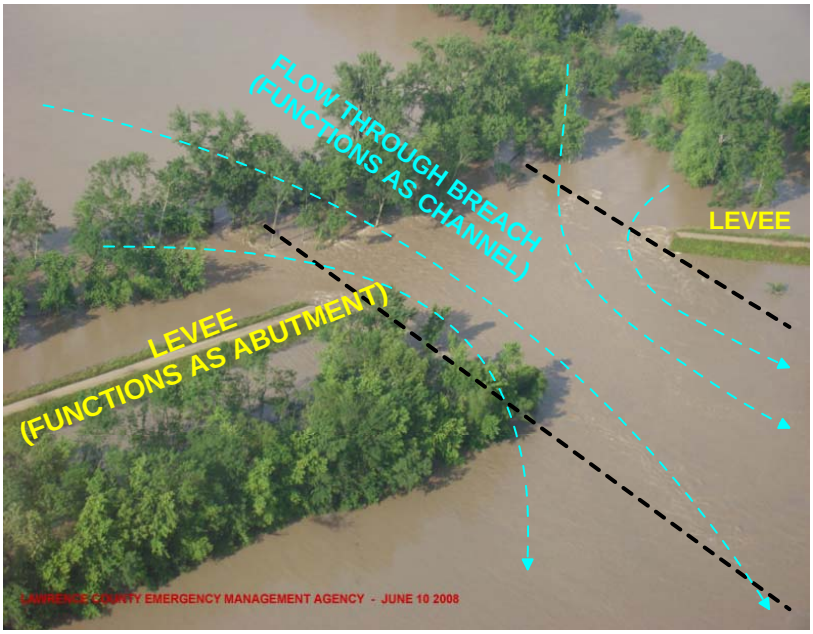

(b)

Figure 2.13 Conformance of Fully-Developed Breach to Shape of Spill-Through Abutment: (a) Model Shape Used in Spill-Through Bridge Abutment Design, (b) Photograph of Fully Developed Levee Breach (photo by Brent Poirot).

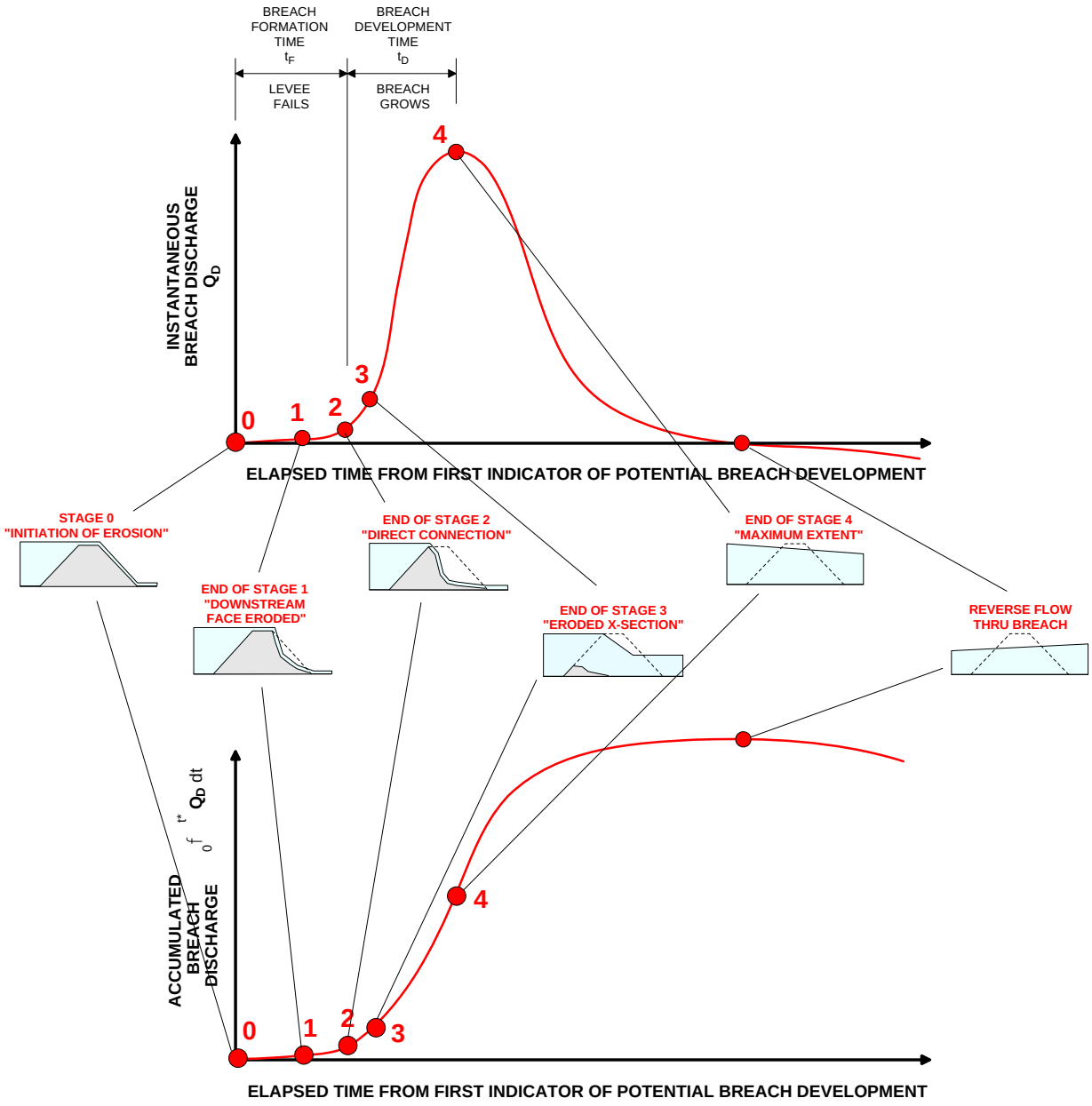

Figure 2.14 Typical Breach Discharge Curves.

breach development. The elapsed time corresponding to the end of Stage 2 erosion is termed the "failure time," (t_F) or the "breach initiation time" (Wahl, 1998).

As described previously, the breach grows rapidly from the end of Stage 2 to create a fully eroded section of levee which then begins to lengthen. This latter increment of time, during which the levee grows across its width and then expands along the levee alignment, is termed the "breach formation time" or "breach development time" (t_D). The breach development corresponds to elapsed time beyond the time to failure, t_F, and thus represents the length of time for which Stages 3 and 4 of erosion have been occurring. The time which has elapsed from the initiation of the breach (marked via some indicator, visual or otherwise) is then the sum of the breach initiation time (i.e., the time to failure) and the breach development time (i.e., the breach development time):

$$t = t_F + t_D \qquad or \qquad t_D = t - t_F \tag{2.1}$$

To date, the majority of formulas employed to characterize breach geometry have been developed from observations of dam failures (MacDonald and Langridge-Monopolis, 1984; von Thun and Gillette, 1990; Froehlich, 1995). These equations were developed to aid the routing of dam-breach floods through a downstream river system or downstream basin. In the context of dam-breach routing, the primary motive of the dam breach equations is to characterize the times associated with large-scale discharges of water into the downstream reach. In a comprehensive review of these approaches, Wahl states the time associated with failure of the dam is typically not of interest in dam-breach flood routing, as the volumes of water released during the failure itself are relatively small when compared to the subsequent discharge through the breach (Wahl, 1998).

Because it is very difficult to distinguish between water volumes released during the failure itself and those released after failure, some simplifications of the dam-breach simulation are generally required, and water volumes released from a dam breach are often considered to begin after the failure has occurred (i.e., t_F=0 for purposes of hydrograph calculation and $t=t_D$). That is, the time to failure is often not explicitly considered in the analysis of dam breaches, although some confusion appears to exist in the professional community regarding the appropriate reference time from which breach hydrographs should be developed.

The time to failure is clearly useful to first responders in estimating the time available to evacuate personnel from the vicinity of a growing breach. However, it is much less useful as an indicator of the size of a Stage 4 levee breach for which a closure will be attempted. Furthermore, breaches developed from underseepage or a catastrophic collapse mechanism may appear to occur almost instantaneously from the perspectives of first responders. For these reasons described here, the time to failure is assumed to be zero (i.e., "instantaneous breaching") in this report, and the breach development times used to calculate breach size do not provide any account of the breach initiation time.

The breach development time for a dam-breach flood simulation is typically estimated using one of three approaches. The first, and simplest, approach is a "curve-fit" in which a number of case histories have been studied and the associated breach geometry has been found to have a statistical relationship to one or more parameters of the dam (e.g., water volume retained by the dam, the height of water retained by the dam, and/or the width of the dam). At the other end of the spectrum of complexity in breach growth modeling is the second approach, for which first principles of physics are used to describe the interaction of the eroding flow and the dam materials. Certain fundamental laws, defined to describe the mechanics of breach growth, are then used in combination the specific conditions present during a given breach event to simulate the developing breach geometry. A third approach is a hybrid, in which empirical observations are mated with certain physical conditions of the flow.

2.6 Empirical Predictions of Breach Size And Breach Development Time

Among the approaches used to estimate the size of a breach, the "purely empirical approach" appears to enjoy the most widespread usage to date. The use of empirical equations reflects their reliance upon easily understood parameters and the potential errors associated with more scientifically rigorous approaches. Given the profession's relatively crude understanding of breach mechanics, many engineers may feel the use of more sophisticated techniques is simply not justified. However, many equations for breach development times suffer from their own weaknesses, as many were derived from

curve fittings applied to observations of dam failures. Several empirical expressions for estimating breach size from development time are shown in Table 2.8.

Many of the purely empirical equations often involve failures of both concrete dams and earthen dams, where levees are only constructed from earthen materials. Concrete dam structures should not be expected to fail by the same mechanisms as earthen dams, and both the time to failure and breach development time for a concrete dam could be radically different from that associated with an earthen levee. In addition, empirical equations for dam breach geometries and dam breach development times implicitly consider the fact that dams retain a finite volume of water which is exhausted during flow through the breach. The fact that the dam retains a finite volume amounts to the specification of a flux boundary condition, and solution of the boundary value problem representing breach growth relies upon this condition. The use of empirical equations including the dam volume is thus implicitly related to a particular solution of the breach problem in which the breach development time is coupled to the breach discharge.

The coupling of breach development time and breach discharge conflicts with the conditions present during major flood events from storm surge or large rivers. In these events, total head conditions remain essentially constant on the flood side of the breach, and the volume of water available to flow through the breach may be essentially unbounded (at least for major floods). In this case, the breach geometry and breach development time exist as independent variables. Solution of the boundary value problem for levee breaches relies upon entirely different boundary conditions, so that the particular solution for a levee breach should not be expected to be the same as that obtained for a dam breach. Furthermore, the empirical equations developed from dam breach observations typically limit the progression of erosion so that the breach does not proceeded into the foundation soils (or rocks) present beneath the dam. In the case of major levee failures, scour of the foundation soils may be a significant contributor to increasing the area through which water may flow into the polder.

Despite these limitations, empirical equations for dam breaching may provide some useful insights into levee breach geometries and the associated time to develop the breach. The majority of the studies found that the fully developed breach assumed a

Table 2.8
Empirical Relationships for Estimating Breach Growth

Compacted Soils	$B = \frac{63075 t_D^{2.747}}{A_L}$	(2.2)	after MacDonald and Langridge-Monopolis, 1984
Fuse-Plug Embankments (h_W/W_b) ≤ 0.12	$B = \overline{K}(4.02 h_L + 45.7) t_D$ $\overline{K} = 0.8039\left(\frac{h_W}{h_L}\right)^2 - 0.003\left(\frac{h_W}{h_L}\right)$	(2.3a) (2.3b)	after Pugh, 1985
Earthen Embankment Dams	$B = 91 t_D$	(2.4)	USBR, 1988
Erosion-Resistant Soils	$B = 4 h_W t_D$	(2.5)	von Thun and Gillette, 1990
Erodible Soils	$B = (4 h_W + 61) t_D$	(2.6)	vonThun and Gillette, 1990
Compacted Clays	$B = 13.4\sqrt{t_D}$	(2.7)	after Verheij, 2002
Compacted Sands	$B = 37.2 t_D^{0.51}$	(2.8)	after Verheij, 2002

where:

B = Breach Length, in meters (measured along levee centerline alignment)
t_D = Breach Development Time, in hours
A_L = Levee Cross-Sectional Volume (represented by cross-sectional area, in m^3/m)
h_W = Water Height, in meters (at location of breach)
h_L = Levee Height, in meters

trapezoidal shape, for which the breach width was generally 0.5 to 5.0 times the depth of the breach. The breach width was most commonly observed to be 2.0 to 4.0 times the breach depth, with an upper bound on this ratio approximately equal to 10.0. These studies further concluded that the side slopes of the breach area (m_S, see Figure 2.4) typically varied from essentially vertical to 1V:1H, with the most common slope corresponding to approximately 2V:1H. Finally, the studies indicate the breach development time for dams is typically between 0.1 and 1.0 hour. This finding is a stark contrast to case studies of levees constructed of compacted clay, for which the initiation of downstream erosion may occur for 10 to 20 hours prior to breaching (Gilbert and Miller, 1989). The dam studies found that the rate of breach development for poorly compacted materials may be two or more times faster than well compacted materials.

From the available dam-breach studies involving empirical equations, the set of equations shown in Table 2.9 is considered further. Each of these equations provides an empirical relationship between the breach formation time (representing the time over which a failed levee has had time to grow) and the breach length. The first three sets of equations were specifically developed for data sets involving earthen dams, and thus suffer from the restrictions mentioned previously regarding extension of these equations to levees. The fourth set (Verheij, 2002) was developed specifically for rapid estimates of breach length in levees, and the levee construction is assumed to correspond to either compacted sand levees or compacted clay levees. No distinctions are made regarding the mechanism initiating the failure (e.g., piping, overtopping, or global instability), levee heights, or total head differentials across the levee.

With the exception of the equations from Verheij, the empirical relationships shown in Table 2.9 appear to indicate the dike breach may continue to grow indefinitely, so long as the flood event continues. In reality, the natural flood period and inundation of the polder impose certain limits on breach growth. Table 2.9 includes several equations developed to characterize the usual maximum size of breached levees. Equations 2.9 and 2.10 were developed from studies of embankment dams, where a finite reservoir volume likely influences conclusions regarding the maximum dike length. Equation 2.11 was developed from observation of 142 failures of compacted clay levees along the Tisza River. The maximum breach lengths estimated from these equations vary between 30 m

Table 2.9
Empirical Equations for Estimating Maximum Breach Length

Earthen Embankment Dams	$B = 10\,h_w$	(2.9)	after Macdonald and Langridge-Monopolis 1984
Earthen Embankment Dams	$B = 2.5\,h_w + 54.9$	(2.10)	von Thun and Gillette, 1990
Tisza River Levees (Compacted Clay)	$B = 5.19\,e^{\,0.75\,h_w}$	(2.11)	Nagy, 2006

where:

B = Maximum Breach Length, in meters
h_W = Water Height, in meters
e = Basis of Natural Logarithms, e = 2.7812

and 51 m (98 ft and 167 ft) for a 10-ft high levee and between 46 m and 160 m (150 ft to 525 ft) for a 15-ft high levee.

Prior research with large embankment dams in the United States estimated the maximum breach length for these structures as approximately 150m (MacDonald and Langridge-Monopolis, 1984). As further context regarding a "usual" maximum breach size, breach simulations within the California Delta System have employed 30-m to 90-m (98-ft to 300-ft) breach to represent a "narrow breach" and 152-m to 228-m (500-ft to 750-ft) breach to represent a "wide breach" in flood routing simulations. Similar flood-routing simulations for clay levees along the Mississippi River have employed 41-m (135-ft) breaches and 122-m to 153-m (400-ft to 500-ft) breaches to represent a small and large breaches, respectively.

Breach lengths associated with each of the equations in Table 2.8 are plotted as a function of breach development time in Figure 2.15. As some of the equations in Table 2.8 require estimates of the levee geometry, Figure 2.15 presents ranges of breach growth corresponding to a 3.0-m (10-ft) levee height (h_L) and a 4.6-m (15-ft) high levee. Crown widths (b) of 3.0 m (10 ft) and side slopes of 1V:3H (m_P=m_F=3) were further assumed. The water height (h) was assumed to equal the levee height (h_L) for all calculations represented in Figure 2.15. This assumption causes the upper bound of breach lengths for each equation to be associated with the taller levee cross-section.

The erosion rates of several levees were characterized in recently completed research within the SERRI initiative (Resio et al, 2009) using a selected number of case histories of controlled dike failures in Norway and those contained within a database of embankment dams maintained by the U.S. Bureau of Reclamation (Wahl, 1998). From this dataset, the researchers concluded that rates for lateral growth of levee breaches would reasonably vary from 9 m/hr in (30 ft/hr) erosion-resistant soils to 60 m/hr (200 ft/hr) in erodible soils. Trendlines for linear breach growth at 9 m/hr and 60 m/hr are superposed on Figure 2.15.

Data associated with several additional case studies, presented in Figure 2.16, generally confirms this range. Rates of erosion estimated in Figure 2.16 for the Inner Harbor Navigation Canal floodwall failure were significantly higher, and the erosion mechanisms at this failure were likely altered by the presence of a large vertical drop at

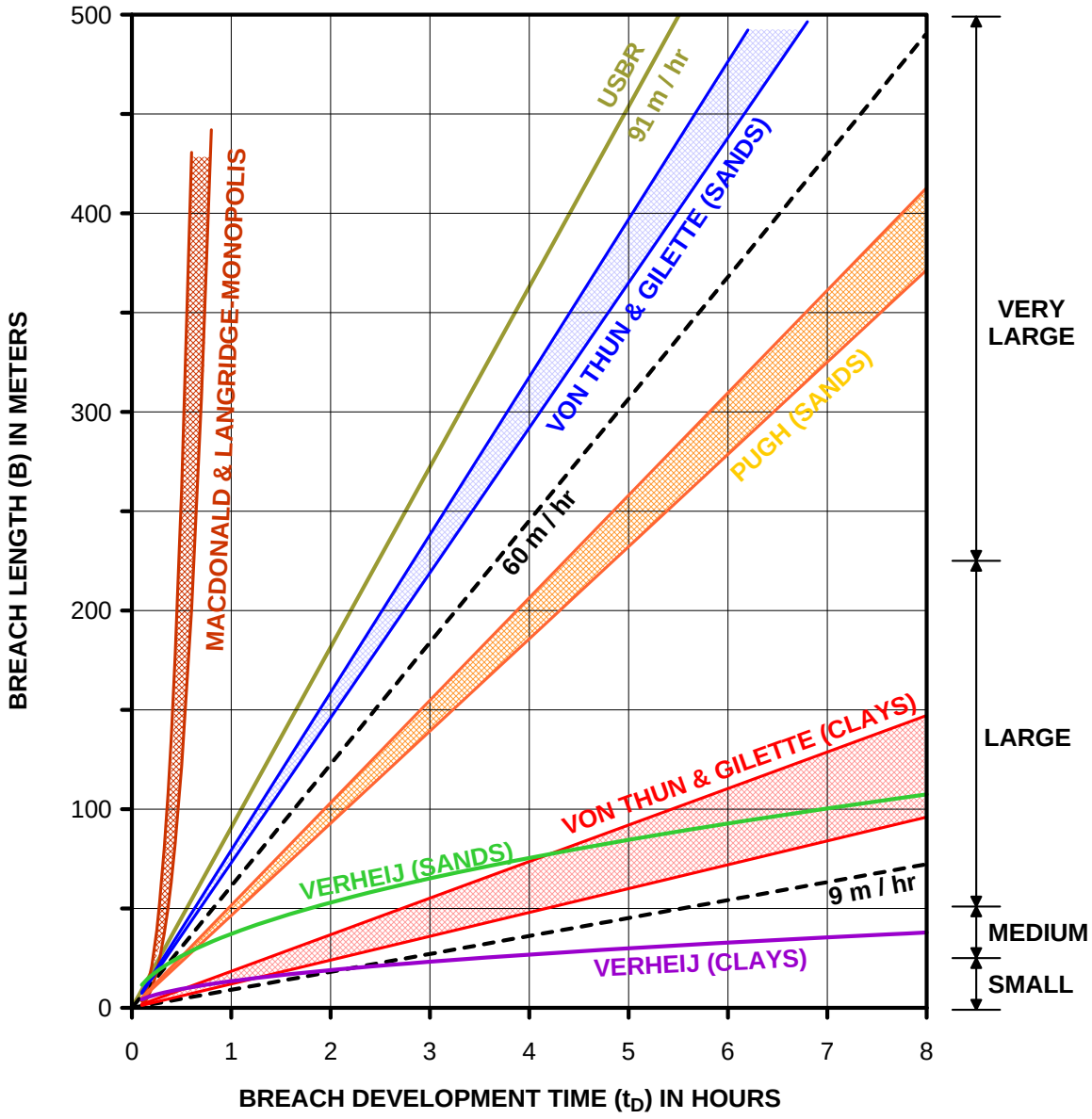

Figure 2.15 Rates of Levee Breach Growth Predicted by Empirical Equations.

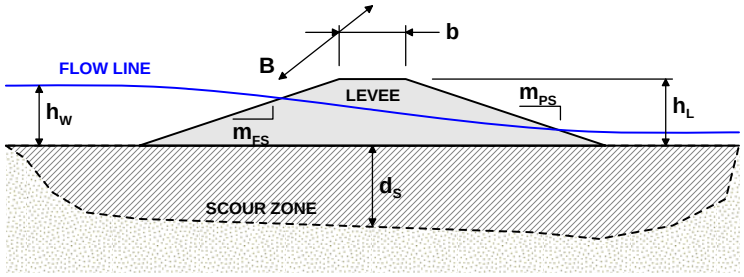

LOCATION AND DATE	Flood Source	Levee Height h_L (m) (1)	Flood Side Slope m_{FS} (1V : #H)	Crest Width b (m)	Protected Side Slope m_{PS} (1V : #H)	Water Height h_W (m)	River Flow Q_S (m^3/s)	Breach Length B (m)	Scour Depth d_S (m)	Breached Levee Volume (m^3) (2)	Erosion Rate (m^3/hr) [m/hr] (3)
Olivehurst-Arboga Levee on Feather River Near Arboga, California (January 1997)	River	8.5	2.0	6.1	3.0	7.6	8,500	190	17.2	44,500	N/A (4)
Pin Oak Levee on Mississippi River Near Winfield, Missouri (June 2008)	River	3.7	3.0	3.0	3.0	3.4	12,200	46	- -	2,500	1,300 [23]
Truckee Irrigation Canal Levee Near Fernley, Nevada (January 2008)	River	2.9	2.0	4.6	1.5	2.0	21	15	3.3	430	150 [17]
Jones Tract Levee on Middle River Near Stockton, California (June 2004)	River	4.8	3.0	8.5	3.0	2.8	180 (5)	105	- -	19,700	4,000 [71]
Russell-Allison Levee on Wabash River Near Westport, Illinois (June 2008)	River	2.4	3.0	3.0	3.0	1.5	2,800	53	- -	1,360	50 [2]
Cap au Gris Levee on Mississippi River Near Winfield, Missouri (June 2008)	River	2.8	3.0	3.0	3.0	3.3	12,200	107	- -	3,300	1,800 [53]
Floodwall on Metairie Outfall Canal New Orleans, Louisiana (August 2005)	Hurricane	3.4 + 2.3	3.0	3.0	3.0	5.2	N/A	137	4.6	10,100	N/A
Floodwall on London Avenue Canal New Orleans, Louisiana (August 2005)	Hurricane	2.7 + 2.4	3.0	3.0	3.0	4.0	N/A	38	6.4	3,020	N/A
Floodwall on Inner Harbor Navigation Canal New Orleans, Louisiana (August 2005)	Hurricane	4.3 + 1.8	3.0	3.0	3.0	6.7	N/A	280	1.5	9,000	9,000 [280]

NOTES

(1) Added heights show additional vertical height contributed by floodwalls (concrete wall section above the earthen levee section).

(2) Breached levee volume excludes scour of foundation soils. Estimates shown are averaged eroded volumes over a minimum elapsed time of 2 hours. These rates may not correspond to instantaneous erosion rates occuring at the initiation of breaching or at full development of breach.

(3) Erosion rates are for breached levee volume (without foundation scour). Values in braces [##] are rates of breach expansion in terms of distance along levee centerline.

(4) Erosion rates for "instantaeous" breaches involving massive failure volumes are not computed.

(5) Estimated peak flow through breach via back-calculated matching of local hydrographs (Meirzwa and Suits, 2005).

Figure 2.16 Observed Breach Geometries and Growth Rates for Several Recent Levee Breaches in the United States.

the floodwall. Finally, a suite of tests involving scaled physical models of compacted clay, silty clay, and silty sand embankments indicated lateral breach growth rates between 0.5 and 20.7 m/hour (Hanson et al, 2008). The majority of these breaches grew at approximately 3 m/hr during the tests, which were typically performed over a period of 3 hours or less.

2.7 Physically-Motivated Models and Hybrid Models of Breach Development

Empirical observations of breach geometries provide great insight into the geometries which may generally be anticipated at a breach location and the time required to develop that breach size. However, application of empirical equations to a given breach may be inappropriate if the characteristics of the breach and the mechanisms of its development do not conform to those for which the empirical equations were developed. For this reason, a strong motivation exists to understand the basic properties influencing breach growth and the specific mechanisms involved in the growth. The characteristics of the breach may include all of the factors identified in Table 2.8, and the various degrees of influence of these factors may change as the breach evolves. Similarly, one or more mechanisms of breach erosion and growth may be at work at any given time, and a breach model would ideally uncover which mechanisms dominate each phase of breach development and identify bifurcation points at which the relative influences of various mechanisms are changed. This sophisticated characterization of the breach size and development is the goal of breach growth models (Wahl et al, 2007).

The use of purely physically based models may be viewed as one in which several modes of levee failure are explicitly investigated at any time. Assuming the flow field through the breach may be adequately characterized at a particular instant during the levee breach development, an analyst may wish to consider where the levee is being eroded by the fluid flow, by comparing estimates of the tractive stress rate imposed by the flow to erosion rates of the soil obtained from laboratory testing performed at various tractive stress rates. This comparison may be done at every point along the levee and local ground surface at the instant in time for which the flow conditions have been characterized. Furthermore, based on the laboratory characterization, highly localized

estimates of instantaneous erosion rates could be obtained at all points along the levee and local ground surface (Faeh, 2007). In addition, modelers may wish to update estimates of the local soil strengths for the current flow conditions (e.g., by increasing pore water pressures or decreasing total stresses due to the removal of material). Based upon the field of local erosion rates, the volume of soil eroded during a small increment of time may be calculated, so that the entire topography of the ground surface could be altered. The revised ground surface could then be fed back into a redefined hydrodynamic model to update estimates of the fluid flow field.

Through successive applications of this technique, high-resolution estimates of the levee breaching and erosion process are conceivable. These estimates would be permitted to vary by very natural physical laws applied to a discretized physical space and time. However, the computational sophistication of these concepts may be difficult to justify when limited data are available for model calibration.

Due to the complexity of breach models developed from fundamental principles and due to the computationally intensive nature of their use, breach growth is often simulated by using a greatly simplified set of physical rules in combination with certain empirical observations. This hybrid approach is employed in the simulations developed from BREACH (Fread, 1987), BEED (Singh, 1985), and DEICH-P (Broich, 2005). These models typically incorporate calculation routines similar to those shown in Figure 2.17. In general, the modeler will assume an initial breach, which represents the reach of levee overtopped (in the case of a "sagging" crown) or the first erosion trench across the levee (in the case of levee erosion initiated at a specific location). Hydraulic conditions in the vicinity of the breach are commonly defined to fit the assumptions of a weir equation. This weir is typically assumed to be a broad-crested weir for which the weir coefficient, C_D, is generally observed to vary between 3.0 and 3.2 (Fread, 1996). For an assumed overtopping height, the modeler uses the weir coefficient to estimate the discharge through the breach over a particular increment of time. The discharge velocity through the breach may then be calculated.

The rate at which the levee is removed (also, the rate at which the breach grows) may be governed by the rate at which soil is sheared away from the exposed surface of the levee or by the rate at which the flow through the breach is able to transport materials

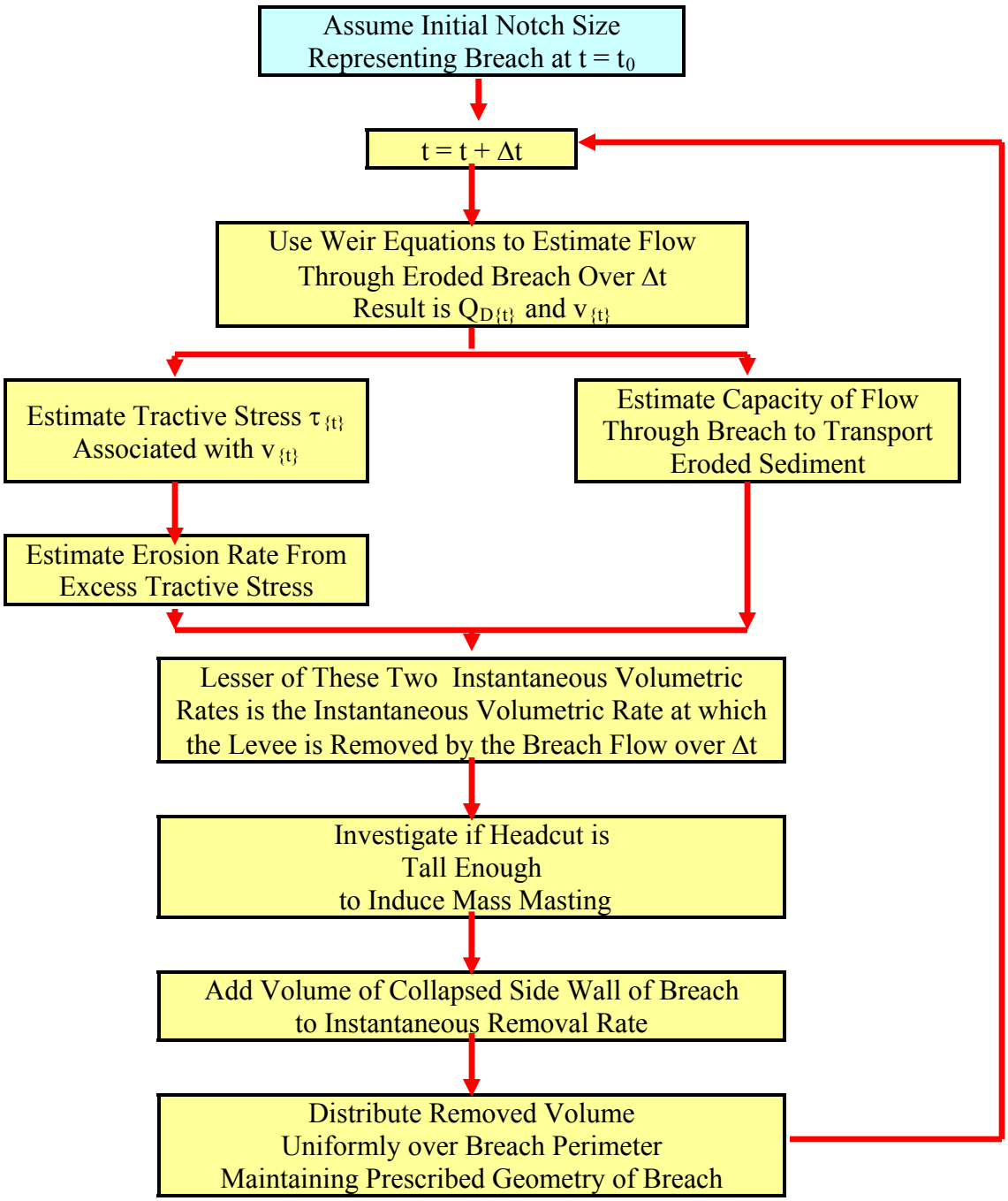

Figure 2.17 Calculation Cycles Employed by Hybrid Breach Growth Models.

away from the breach. In open-channel hydrology, the depth-averaged flow velocity is commonly employed to compare the tractive stresses acting on the flow boundary to the erosion resistance of the soil forming the bed. This approach is also employed in levee breach simulations by using the average flow velocity through the breach to estimate the rate of tractive stresses acting on the exposed levee surfaces. This applied stress rate is compared to an estimate of the shear stress rate which is capable of eroding the levee material (Briaud et al, 2008). The erosion rate of the flow through the breach may be estimated from an equation employing the "excess shear stress rate" (the quantity, τ^*-τ_S, from Ariathurai and Arulandan, 1974). This erosion rate is then coupled with an estimate of the porosity of the levee material to approximate the volumetric rate at which the levee is removed by tractive stresses.

Several breach models, including the widely used BREACH model, supplement the volumetric erosion rate through investigating mass wasting mechanisms such as the collapse of the side walls of the breach. This condition is evaluated by comparing the depth of the breach to the "critical height" of an unsupported cut. This critical height may be estimated from classical soil mechanics using the unit weight and the undrained shearing strength of the compacted levee soil. If the depth of the breach is larger than the critical height of the levee soil, then a triangular prism of soil is instantly removed from the levee section and added to the volumetric erosion rate over the time increment. The volume of this prism is defined by the depth of the breach and the angle of a planar failure surface defined by the soil's angle of internal friction.

The volumetric transport rate must also be considered. This quantity represents the rate at which the water flowing through the breach is capable of transporting eroded materials away from the breach area. This rate may be calculated from a conventional sediment transport equation, such as the Meyer-Peter-Muller equation. As with the volumetric erosion rate, the volumetric transport rate must be converted to an equivalent rate of levee removal through use of the soil porosity.

The rate at which material is removed from the levee section may then be taken as the larger of the volumetric erosion rate and the volumetric transport rate amounts. The change in the volume of the breach is estimated by multiplying the governing volumetric rate of erosion by the increment of time used in the calculation cycle. The incremental

increase in the breach volume is often assumed to result in the removal of a uniform thickness from the sides and bottom of the breach. Several alternative empirical geometric constraints on the breach geometry (e.g., the breach width is maintained at twice the breach depth) are also commonly employed. In this way, the hybrid approach incorporates equations describing certain physical processes and empirically-justified constraints.

Hybrid breach models are widely used in practice, as they give some account of the physical mechanisms governing breach growth while retaining computational simplicity and an adherence to anecdotal observations of breach geometry. Hybrid breach models have been successfully calibrated. These calibrations are performed by minimizing the error between a model-generated routing of a levee-breach flood hydrograph and an actual flood hydrograph observed at a known point downstream from an actual levee breach (Kamrath et al, 2006; Davies et al, 2007). These exercises do not constitute validation of the model mechanisms, but they do provide strong indicators regarding the utility of such dam and levee break simulations in predicting the size of levee breaks.

To perform simulations of levee breaching or back-calculations of breach parameters employing purely physically based and/or hybrid approaches, modelers must know a reasonably high level of information a-priori. Certain sets of these properties may be estimated with reasonable accuracy (e.g., basic strength parameters for levee soils, levee geometries, flood side water elevations, tail water elevations, and flow competency for sediment transport). However, several additional factors required as breach model input parameters in more sophisticated models may be substantially more difficult to evaluate, especially within the severe time constraints associated with levee breach closure. These factors include the spatial distributions of soil permeability and matric suction, local channel geometries, polder areas, and polder topographies.

For this reason, significant value may be achieved by completing breach simulations of all vulnerable polders in advance of a flooding event, as part of a systemic study of risks and potential damages associated with flooding of a particular river system or shoreline community. These studies could easily incorporate appropriate, polder-specific models of topography, land use, and geotechnical conditions to develop a-priori estimates of breach size, polder inundation, and breach flow conditions with time. In the

near term, these simulations may be performed with existing hybrid breach models, though a higher quality understanding of breach mechanisms may be simultaneously gained from geotechnical investigations conducted during completion of these simulations. The basic capabilities exist today, and could be of significant value to first responders tasked with breach closure.

2.8 The "Typical" Levee Breach Used In This Study

Previous sections of this report have demonstrated a wide variety of conditions which may be encountered by first responders to an active levee breach. Because of severe constraints upon the time available to achieve closure of an active breach, the greatest advantages appear to be gained from techniques which apply to large levees, protecting large polders from long-period flood events. In these cases, the protraction of the flood hydrograph implies a stronger possibility that breach closure may be achieved in sufficient time to provide effective relief from further flood damages. For this reason, a large levee section, rising 7.6 m (25 ft) above the local grade, was selected for this study. The levee section was assumed to have side slopes of 1V:3H and a crown width of 15 feet. The flood source was assumed to rise to the levee crest, without a large overtopping height and without waves.

We have further assumed the "typical breach" will develop from flood sources providing sufficient flow that the elevations of the flood source are not significantly altered by the presence of the breach. This amounts to a requirement that the discharge through the breach (Q) must be essentially constant for a given breach width (B), length (L), and head differential ($H = z_F - z_P$), implying linearity of these relationships in the mathematical sense. This requirement excludes the consideration of small breaches for which the breach is sufficient to drain the flooding source, thereby mitigating the potential for further breach development. The use of a large levee section (and a commensurately large flooding source) provides additional advantages of providing estimates of breach discharge and flow velocities representing the upper end of conditions which may be encountered.

While breaches of sand levees have been observed to grow more rapidly than those occurring in clay levees, the researchers judged that a clay levee would provide a better representation of the majority of primary flood protection levees in the United States. No data exists to clearly support any assumption regarding the time required to mobilize a particular repair technology to the site of a breached levee. For this reason, a "target response time" was assumed of 3 to 4 hours after the breaching of a levee, with the goal of achieving full closure of the breach within 4 to 24 hours after mobilization to the breached levee. This aggressive goal for a response time is somewhat arbitrary and clearly excludes the application of many existing technologies. The use of a very short response time reflects the objective of investigating alternatives to many conventional technologies requiring much more time to mobilize. The rapid response time used herein is also supported by several existing case studies of active levee breaches discussed in this report.

It was assumed that the levee breach be 62.5 m (200 ft) in length at the time breach closure is initiated. This estimate incorporates the stated assumptions regarding the assumed levee section, flood source, and response time. The assumed length is within the range of estimates which would be obtained from empirical equations for the breaching of clay levees, and is supported by a number of case histories mentioned in this report.

CHAPTER 3

TECHNIQUES IN SIMULATION OF BREACH CLOSURE

3.1 Levee Breach Repair – Physical Modeling

As with the initiation of levee breaches, the closure of these breaches is a familiar problem. Expertise in closing active levee breaches has historically developed from the experiences of a relatively small number of levee district personnel, emergency responders, and construction contractors. This expertise has remained within this relatively small community, with little definition or scientific characterization (e.g., USACE, 1966). In addition, little engineering research has been conducted regarding the techniques associated with emergency closure of levee breaches, predictive methods for determining the success of a proposed closure alternative, or appropriate techniques for modeling breach closure. The paucity of available research in this area is being addressed, in part, through ongoing research efforts sponsored by DHS research initiatives within the same program as the work described in this report. Interested readers are referred to recent scale model studies of the efforts undertaken to close the breach at the 17th Street Canal in New Orleans immediately after Hurricane Katrina (Sattar et al, 2008) and to model demonstrations of water-filled, cylindrical bladders used to seal breached levees (Resio et al, 2009).

3.2 Levee Breach Repair – Computational Simulation

3.2.1 Hydrodynamic Modeling

Having defined a set of conditions (levee geometry, flood period, flood height, and breach length) reasonably representative of a typical levee breach, the research team then investigated the flow conditions existing in the vicinity of the breached levee. These conditions represent the ambient field through which any mass must flow during an attempted breach closure. Investigation of the flow conditions in the vicinity of the levee breach also provides some indicators of the types of materials which may be deposited onto

the local ground surface by a levee crevasse. These materials are of interest, as they could provide the most easily accessible raw materials for constructing a breach repair.

The flow conditions in the vicinity of the breach were developed from a numerical simulation of a fully developed (Stage 4) breach. This representation does not capture the complex dynamics involved in development of the breach to Stage 4, but rather provides a representation of the conditions which could be encountered by first responders attempting to seal the breach.

Numerical simulations (based upon either finite differences or finite element techniques) seek to solve four sets of equations derived from the application of conservation laws to elementary volumes which are assumed to represent conditions present at every point within a region of interest. In particular, these simulations are generated based upon three physical requirements—conservation of mass, conservation of momentum, and conservation of energy. A general form of the conservation of mass (the so-called "Continuity Equation") over a representative elementary volume (Shames, 1982) may be written as:

$$\frac{Dm}{Dt} = \oiint_{CS} \rho \underline{v}.\underline{n}\, dA + \frac{\partial}{\partial t} \iiint_{CV} \rho\, dV \qquad (3.1) \qquad \text{(scalar)}$$

The conservation of linear momentum (i.e., the combined statement of Newton's First and Second Laws of Motion) for this same volume may be written as:

$$\underline{f} = \oiint_{CS} (\underline{\underline{T}}\,\underline{n}).(\underline{n}.dA) + \iiint_{CV} \underline{b}.dV \qquad (3.2) \qquad \text{(vector)}$$

and the associated conservation of energy (i.e., the First Law of Thermodynamics) may be written as:

$$\dot{H} + P_S + \oiint_{CS} \underline{\underline{T}}\,\underline{n}.\underline{v} - \iiint_{CV} \underline{b}.\underline{a}\, dV = \oiint_{CS} \left[\frac{|v|^2}{2} + |g|z + \frac{p|g|}{\gamma} \right] (\rho \underline{v}.\underline{n}\, dA) + \frac{\partial}{\partial t} \iiint_{CV} \left[\frac{|v|^2}{2} + |g|z + \frac{p|g|}{\gamma} \right] \rho\, dV \qquad (3.3) \qquad \text{(scalar)}$$

These equations correspond to fluid motion through the elementary volume which may itself be in motion. Integrations associated with a flux quantity are made with respect to the surface of the elementary volume (the "CS" subscript), and these integrations will typically be performed in a piecewise sense, with the differential area of the surface aligning with the fixed directions of a basis vector system defining the three directions of physical space. Integrations associated with quantities varying within the volume (the "CV" subscript) are made over the element's volume. In this Lagrangian framework, the velocity

vector must be taken as the spatial velocity. Where the velocity appears as a scalar value, the velocity norm |v| is used. The first two terms of the energy balance in Equation 3.3 represent the heat flux through the control volume and any point sources of work supplied to the control volume (e.g., as by pumps).

Equations 3.1 through 3.3 thus represent a system of five equations to be satisfied by five primary unknowns corresponding to the components of specific energy (kinetic specific energy of velocity having components in three spatial directions, potential specific energy of position, and potential specific energy of unit pressure) present at each spatial position in the problem. Several assumptions must be made for the system to be properly constrained and made tractable. Through exclusion of the three equations describing angular momentum of the flow from the set of equations presented above, we have implicitly assumed the condition of "irrotational flow". While this is not strictly true, the problem was modeled at a characteristic length scale considerably larger than that associated with vorticity influencing incipient motion of eroded particles. The effects of vorticity are only given account through a mass-averaging, in which velocities over the entire depth of flow at a given location are empirically related to velocities causing erosion. This technique provides a computational efficiency while providing some consideration of the effects of vorticity.

In addition, the researchers have assumed the flow is "isothermal," implying that variations in the primary measure of heat energy (i.e., the temperature) do not occur in the problem. This assumption is justified by the fact that temperature variations within this problem should not be significant over the relatively small regions involved in the flow. The assumption of "isothermal" flow has the effect of eliminating the heat flux term (□)from consideration in Equation 3.3. The term related to externally supplied power (P_S) permits the inclusion of pumping capacity from a polder subject to inundation. This term was also neglected to provide a conservative estimate of behaviors in the vicinity of the breach. Considering the large volume of flows typically associated with a breached levee, it is unlikely that pumping capacity within the polder would significantly alter the problem, at least in the vicinity of the breach itself.

The fourth term within the energy balance represents body forces on the elementary volume. A comparable set of equations may be arranged to include the self weight of the fluid as a body force. However, the fluid self-weight has been considered within the energy

balance (via the "pressure head" terms on the right side of the equation, so that the body forces on the left hand side are neglected. In addition, the flow field has been assumed to be a "steady" flow which does not vary with respect to time. Clearly, the problem of a levee breach is one which does vary in time. To accommodate this likelihood, the "steady flow" is assumed to exist over a very small increment of calculation time, and an overall record of time-varying flow may be constructed by assembling a sequence consisting of the increments of steady flow. The effect of this assumption is that the terms in Equations 3.1 and 3.3 associated with time derivatives over the elementary volume may be neglected within a single calculation cycle.

The remaining terms of these equations are related to each other through a constitutive law which is assumed to provide a reasonable relationship between the spatial velocity field and the spatially-varying set of stresses. Within the field of hydraulic modeling, it is common to assume the fluid flow is viscous and incompressible. The assumption of incompressibility is justified by the fact that hydraulic flows typically occur at very low Mach Numbers (i.e., at $\mathbf{M} < 0.3$ to 0.8) for which mean stresses are suitably low relative to the bulk compressibility of the fluid. Assuming flow velocities through the breach will not exceed 10 m/s, the associated Mach Number of the breach flow ($\mathbf{M} = 0.05$) indicates the fluid would exhibit a very stiff bulk compressibility response at the relatively low mean stress levels associated with the levee breach closure problem. The assumption of incompressibility simplifies the equations in two ways. First, kinematic constraints are placed upon the flow velocity field, as the third term in Equation 3.1 and the last term in Equation 3.3 vanish (through a lack of dependency between the density and time). These simplifications are thus a duplicate of prior assumption of steady flow over a small time increment. Second, a constraint is placed upon the possible forms of the constitutive law. Considering the fluid as viscous and incompressible, the constitutive law assumes the following form (the so-called "common Newtonian" fluid):

$$\underline{T} = -p\underline{I} + \mu\left[\nabla\underline{v} + (\nabla\underline{v})^T\right] \qquad (3.4) \qquad \text{(tensor)}$$

The energy balance shown in Equation 3.3 may be used to place limits upon appropriate values of the dynamic viscosity (μ) of Equation 3.4. Under the various assumptions previously stated for the flow (e.g., "isothermal, steady, irrotational, and

incompressible, without externally-supplied work") this restriction permits equivalence between the statements related to the balance of energy and the balance of momentum, further simplifying the equation set. One final simplification may be made by considering only two dimensions of the flow instead of three. This is the simplification utilized in the "shallow water equations" for which the elementary volume is integrated in one spatial direction to produce a specific depth of flow. The velocities in the two remaining spatial directions (those corresponding to "plan view" coordinates in the shallow water equations) represent depth-averaged velocities. When the averaged flow velocities are related to eddying stresses at the ground surface through the kinematic eddy viscosity (μ_e*), the complete set of conservation equations may be cast in the following form (Berger and Stockstill, 2004):

$$\frac{\partial}{\partial t}(v_1 h)+\frac{\partial}{\partial x_1}\left(v_1^2+\frac{1}{2}g h^2-2h\mu_e^*\frac{\partial v_1}{\partial x_1}\right)+g h\frac{\partial z}{dx_1}+\frac{h}{\rho}\frac{\partial u}{\partial x_1}+\frac{n^2 g v_1|v|}{C_0^2\sqrt[3]{h}}=0 \qquad (3.5) \qquad \text{(scalar)}$$

$$\frac{\partial}{\partial t}(v_2 h)+\frac{\partial}{\partial x_2}\left(v_2^2+\frac{1}{2}g h^2-2h\mu_e^*\frac{\partial v_2}{\partial x_2}\right)+g h\frac{\partial z}{dx_2}+\frac{h}{\rho}\frac{\partial u}{\partial x_2}+\frac{n^2 g v_2|v|}{C_0^2\sqrt[3]{h}}=0 \qquad (3.6) \qquad \text{(scalar)}$$

$$\frac{\partial h}{\partial t}+\frac{\partial}{\partial x_1}(v_1 h)+\frac{\partial}{\partial x_2}(v_2 h)=0 \qquad (3.7) \qquad \text{(scalar)}$$

Equations 3.5 through 3.7, represent a system of three equations, with the first two representing the balance of linear momentum, and the last representing the conservation of mass. These equations vary in two physical dimensions (the directions $\underline{e}_1$ and $\underline{e}_2$, corresponding to "plan view" dimensions of shallow water flow) and vary with respect to time. The third physical dimension is simply represented by the depth of flow (h). The equations are used to find the two components of velocity (v_1 and v_2) and the depth of flow (h) at every point within a region at every instant over a prescribed simulation time. The flow depth is to be determined over the entire region being modeled, though specific values of the flow depth are prescribed along the flood side of the levee (h_F). The elevation of the ground surface (z) must also be prescribed at all locations and times throughout the region represented in the simulation.

A finite element approximation for these three unknowns has been implemented within the Adaptive Hydraulics (ADH) computer code developed by the USACE (Berger and Howington, 2002; Berger and Lee, 2004). The region for which a simulation is to be developed is discretized (in plan view) to create elements for which the height varies (according to the height of water), as shown in Figure 3.1. Within ADH, the location of the advancing water front is considered in every element at every calculation increment, with the element integrations reduced to zero where there is no depth of flow. This contrasts with schemes in which the problem domain is dynamically modified by assuming an extent of inundation prior to a calculation cycle and "turning elements on or off." This may cause some computational expense within each calculation cycle, but it is has been judged to provide a better representation of the location of the water surface during a simulation.

The ADH code employs the well-accepted technique of the Newton-Raphson scheme to develop estimates of the primary solution variables for subsequent calculation cycles within each increment of real time. ADH employs a Petrov-Galerkin scheme in which weighting functions constructed from a combination of the polynomial interpolation functions and their derivatives. These weighting functions are dynamically modified during each calculation cycle to dampen the propagation of rapidly-traveling and very steep gradients in flow depth. These types of variations often cause oscillation of the approximate solution and an associated loss of convergence at locations where there truly exists a highly local variation in the energy. These strong variations should be expected to exist near the boundaries of the flow or in areas where there is a rapid dissipation of energy. In the case of a levee breach, the overland flow of the flood wave (after it has passed through the breach and begins to cover formerly dry terrain) or the development of a hydraulic jump (likely where the breach flow falls through a weir-like drop) would constitute conditions for which this oscillation might occur.

To employ ADH within a levee breach simulation, the levee breach geometry must be assumed to be "fixed" at a particular configuration. The levee is represented in the simulation as a boundary similar to the local ground surface, across which no flow is permitted, though shear stresses may be generated by flow parallel. The breach discharge is represented by the specification of the depth of water (h) at locations around the problem where the flood will persist. This depth of water will presumably be known from existing

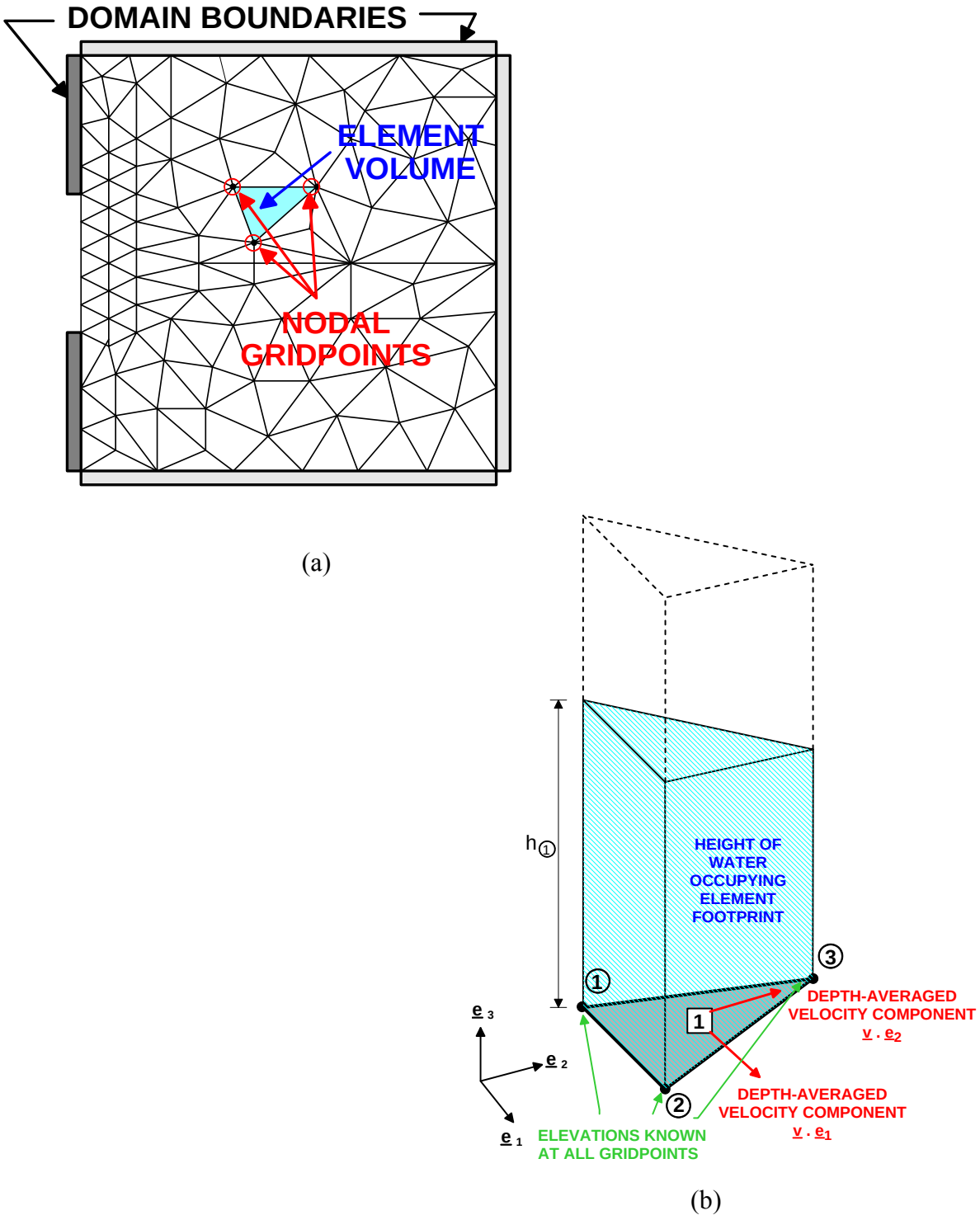

Figure 3.1 Discretization of Problem Doman for Hydrodynamic Modeling via Shallow Water Equations: (a) Plan View, and (b) Isometric Section of a Single Element.

terrain maps (to define the ground surface, z) and from predictions of the flood crest and flood period generated for the breach location (to define the water surface elevation of the flood source as a function of time). These predictions of the flood crest and flood period would presumably be generated from a separate set of analyses performed prior to the breach simulation. Such predictions could be generated using ADH or any other computer code having similar features for flood routing (e.g., HEC-RAS).

With the boundary conditions defined to represent the flood source, and any boundaries defining the polder under inundation (including the levee, the breach opening, the ground surface throughout the polder, and any secondary levees or polder drainage systems), the simulation begins with the release of the flood into the breach. In each increment of time, the flow conditions reach an equilibrium defined by an acceptably small change in the flow velocities and the water height between any two calculation cycles (approximation steps within the time increment). The equilibrium conditions at the end of one increment of time are then employed as the initial conditions over the next very small increment of time. Eventually, for the user-defined boundary conditions (i.e., those defined for the flood water heights at the source and the zero-flux boundaries corresponding to the ground surface and levee) the approximation of the flow will proceed through a sufficiently long record of time to reach a steady-state condition. At this steady-state, the variations in flow velocities and water height will be imperceptibly small over an increment of time (as opposed to variations over a calculation cycle completed within one of the time increments).

The results of one such ADH simulation are provided in Figure 3.2. This figure illustrates the variation in depth-averaged flow velocities throughout a polder adjacent to a breached levee. The levee and the breach correspond to the "prototypical levee breach" described previously. The water surface elevation for the flood source was assumed to rise to the top of the levee along the high-side of the flood (represented by the blue-shaded region forming the upper left corner of Figure 3.2). The water surface elevation dropped slightly along the flood channel (along the left edge of Figure 3.2) to an elevation 0.09 m (0.3 ft) feet lower along the downstream end of the flood source (the lower left corner of Figure 3.2). The distance along the channel of the flood source (along the left edge of the problem) is 1890 m (6200 ft). The region included in the model (along the top and bottom edges of Figure 3.2) extends from a point 385 m (1262 ft) on the flood side of the levee centerline to a

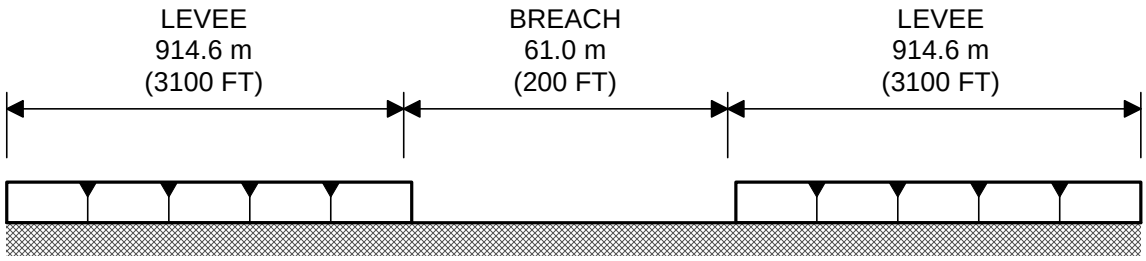

(a)

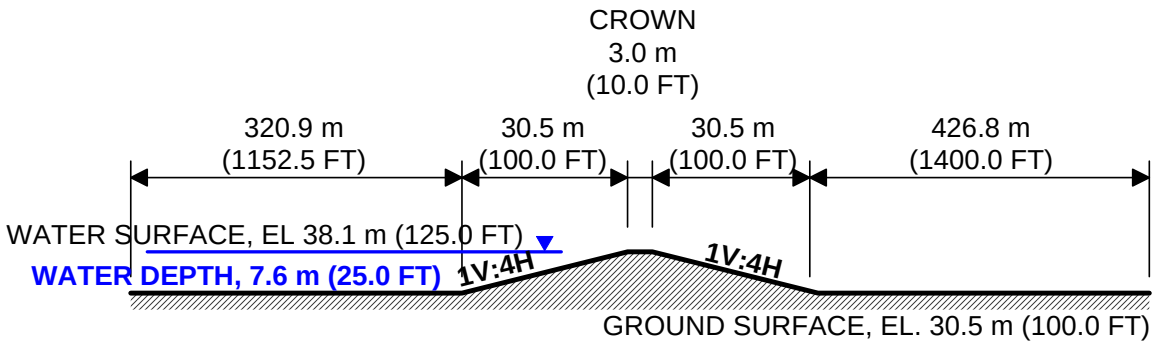

(b)

Figure 3.2 Simulation of Hydraulic Boundary Value Problem in Vicinity of a Typical Levee Breach: (a) Elevation View of Breached Levee, As Modeled, (b) Section Through Breach, As Modeled, and (c) Solution for Fluid Velocity Field Obtained from Shallow-Water Simulation.

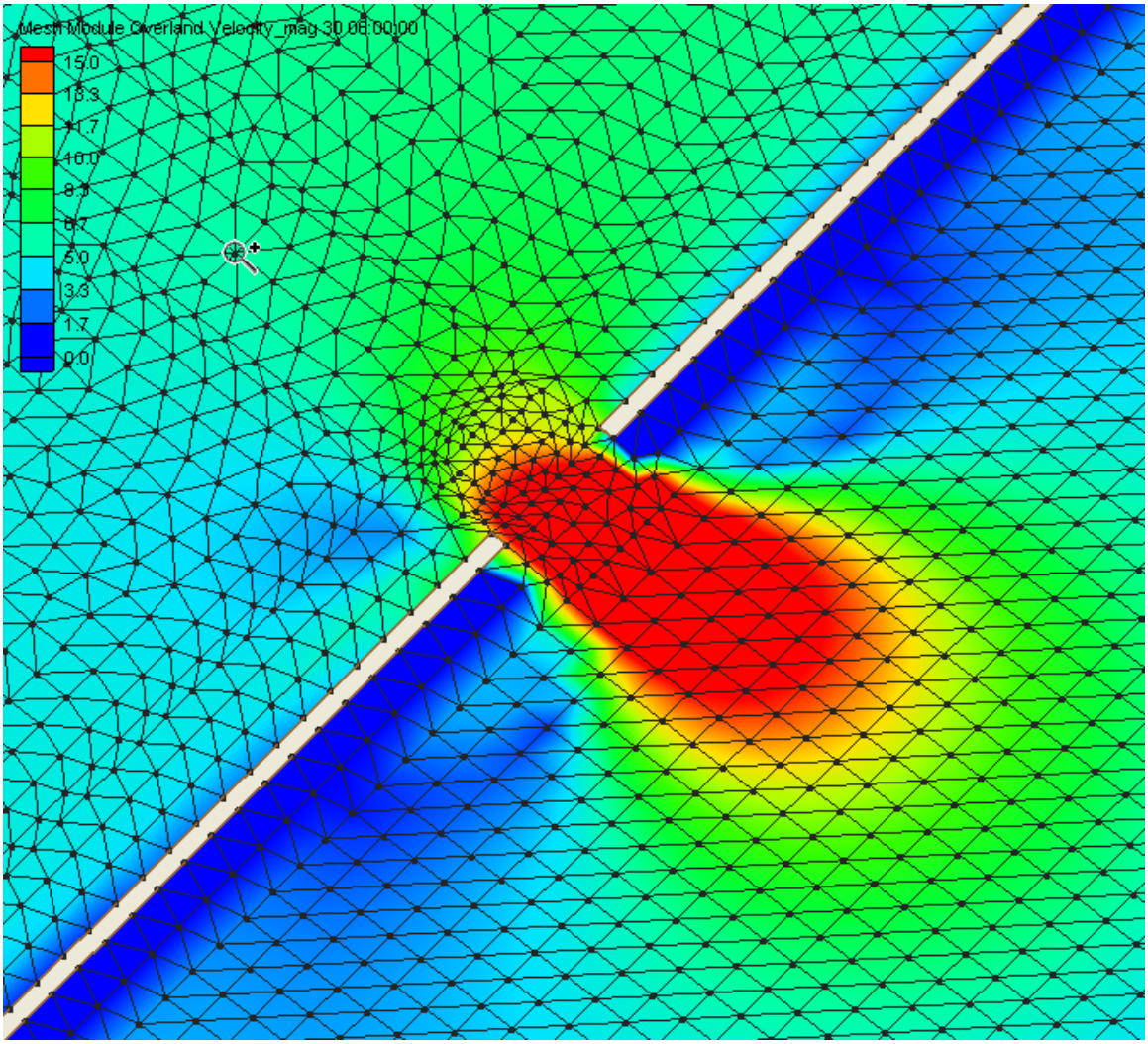

Figure 3.2 (continued) Simulation of Hydraulic Boundary Value Problem in Vicinity of a Typical Levee Breach: (a) Elevation View of Breached Levee, As Modeled, (b) Section Through Breach, As Modeled, and (c) Solution for Fluid Velocity Field Obtained from Shallow-Water Simulation.

point 488 m (1600 ft) on the protected side of the levee centerline. The ground surface defining the polder was assumed to drop with increasing distance from the levee at a slope of 1V:4800H. Natural levees adjacent to major rivers often exhibit slightly steeper slopes between 1V:200H to 1V:1200H.

The ground surface friction (represented by Manning's Roughness, n, within Equations 3.5 and 3.6) is known to be a function of the surface roughness and the depth of flow. Water flowing through a levee breach may traverse ground conditions varying from heavily-vegetated levee surfaces to smoothly-scoured ground surface. The flow depth may vary from several meters in the vicinity of the former levee centerline (even tens of meters when scour occurs) to several centimeters near the front of the advancing flood wave. These conditions were judged to correspond to Manning's coefficients generally remaining within the range defined by $0.015 \leq n \leq 0.035$. Within the simulations presented in Figure 3.2, Manning's n was assumed to equal 0.025.

Errors may be generated in later stages of the simulation from the assumption that the polder drains freely at the edges of the model region. This assumption inhibits the development of a tailwater on the protected side of the simulation. At the early simulation time depicted in Figure 3.2, these effects do not exist. Some simulation error may be generated through the assumption that the ground surface remains uneroded in the vicinity of the breach. The results in Figure 3.2 are thus more representative of conditions which may exist at breaches of levees constructed over medium to stiff silty and clayey soils or at the very early times after levee failure.

By virtue of the assumed boundary conditions, the results of the ADH simulations described herein are more representative of the early stages of a relatively large breach of a mainline flood protection levee during a riverine flood of a large polder. The approach described herein does not include breach development up to the point at which the simulation is initiated. That is, the processes of breach initiation and development are not reproduced for any times between the instant of levee failure and the instant at which breach closure is attempted. While these processes may be crudely approximated by an arranged sequence of "steady-state" analyses of the sort described here, the time involved with such a simulation may render the information of little use unless it the simulation is performed well in advance of the breach. These limitations may not be important, so long as a reasonable geometry for

the flood source, the levee breach (including the eroded ground surface) may be defined. Considering the current state of understanding of the processes involved in breach growth, greater accuracy in the breach development was not warranted for the current study.

The estimated profile of depth-averaged flow velocities is shown in Figure 3.3 for a line perpendicular to the levee alignment through the center of the breach. These velocities correspond to a relatively early simulation time, for which the advancing front of the flood wave is relatively rounded (an indicator of stability in the solution) but the tailwater has not developed to a constant pool elevation within the polder. As may be anticipated, the estimated flow velocities in the vicinity of the former levee are very high, varying between The assumed boundary conditions caused the velocity profiles to be essentially symmetric about the breach centerline, though deviations from this profile should be anticipated (e.g., see the photographs in Figure 2.11), as indicated by Kelley et al, (2008).

The sizes of particles which may be eroded by the flow in the vicinity of the breach are a reflection of the relatively high velocities existing at the breach location. Figure 3.3(b) illustrates grain diameters which would be eroded by the flow conditions (i.e., flow depth and velocity) corresponding to the velocities depicted in Figure 3.3(a). These grain diameters were estimated by considering each discretized element in the model solution as a control volume. The boundary stress at the ground surface of any element may be estimated as the stress acting over the plan area of each element to maintain the equilibrium of the element at a given instant. These stresses may be related to the diameter of an idealized spherical grain at incipient motion through the experimentally observed Shields Parameter, τ^*_C, defined in Equation 3.8.

$$\tau_C^* = \frac{\tau_{EQ}}{(G_S - 1)\, D} \qquad (3.8) \qquad \text{(scalar)}$$

where τ_{EQ} = the shearing stress required to balance the flow momentum,

G_S = the specific gravity of soil solids

D = the grain diameter

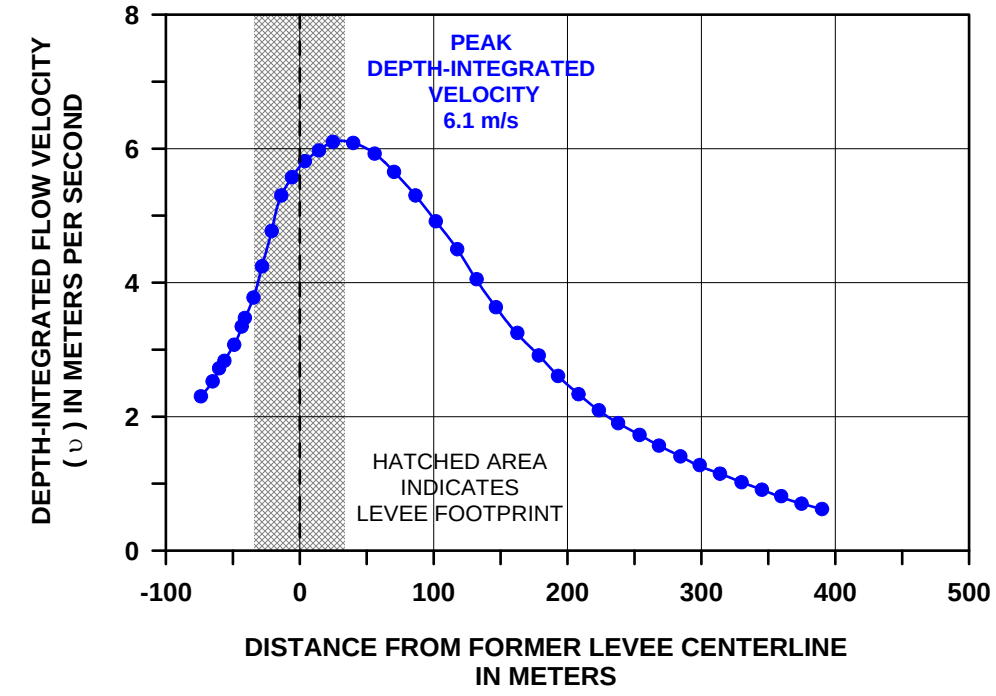

(a)

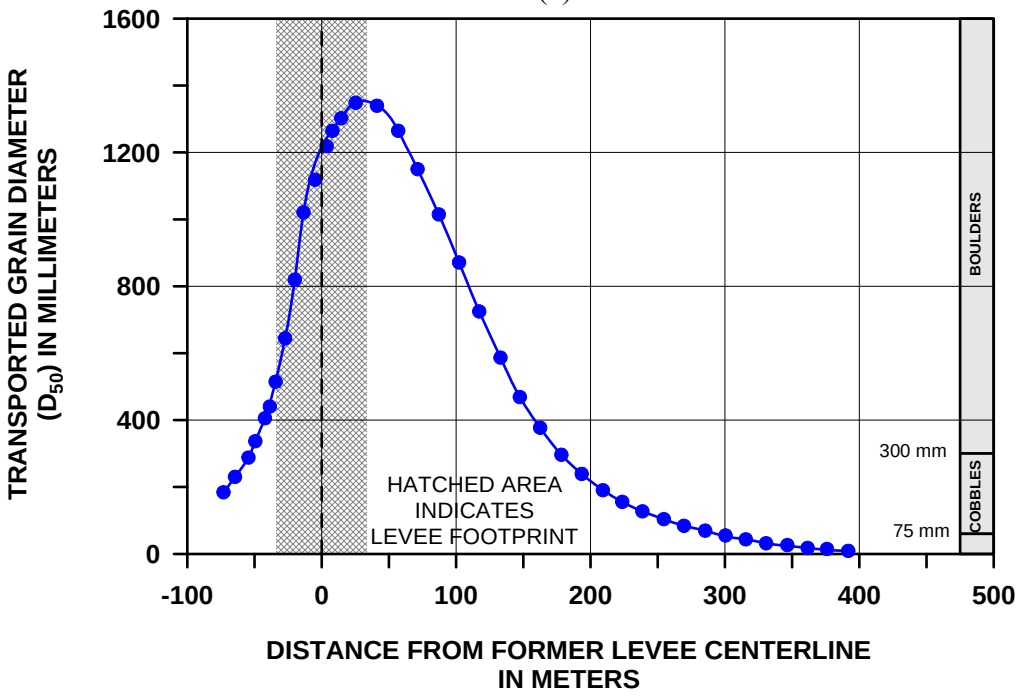

(b)

Figure 3.3 Characteristics of Fluid Velocity Field in Vicinity of a Typical Levee Breach: (a) Depth-Averaged Flow Velocities and (b) Transported Grain Diameters in Vicinity of Modeled Levee Breach.

Because it is strongly preferable to achieve any possible reductions in the emergency response time, it may also be preferable to employ materials existing in the vicinity of the breach to create the breach closure. This may be achieved, for example, through stabilizing the locally available soils into masses which may be used to seal the breach. For this potential use, responders may have an interest in the types of soil particles (as measured by grain diameter) existing near the breach. Through the usage of the Shields Diagram, the grain sizes shown in Figure 3.3 correspond to incipient motion. These grain sizes simultaneously represent the diameters of particles which would be eroded by slightly more competent flows or deposited by slightly weaker flows. The distribution of grain sizes shown in Figure 3.3(b) may thus be representative of grain diameters which could be deposited by the flow conditions illustrated in Figure 3.2, corresponding to a particular instant after levee failure. Deposition of these grain sizes by the breach discharge is contingent upon the presence of these grains within the breach discharge.

Figure 3.3(b) indicates that the particles as large as boulders may exist at a state of incipient motion in the vicinity of the former levee centerline. Gravel-sized particles are seen to be at a state of incipient motion as far away as 450 m (1500 ft) from the former levee centerline. For conditions represented by the modeled levee breach, first responders may expect that any sedimentation deposited in the vicinity of the breach will consist of coarse-grained soils. In general, these soils would be well-suited to stabilization. However, it is unlikely that substantial accumulation of coarse-grained soils would occur in the vicinity of the breach as a result of sediment deposition from the breach discharge, at least at times shortly after levee failure. In consideration of the relatively large velocities depicted in Figure 3.3(a), scouring of the existing ground surface will likely occur during the hours immediately after breaching, and this scour may eventually extend to considerable distances from the levee during the hours immediately after breaching. In this case, soils within the vicinity of the breach may generally be assumed to be those foundation soils present prior to the levee breach.

3.2.2 Modeling via the Conventional Discrete Element Method

The discrete element method (DEM, also termed the “distinct element method”) is a computational technique by which the motions of particles within an assembly may be traced

through time as the boundaries of the assembly are altered. The method was conceived jointly by researchers at the University of Minnesota and Cambridge University in the late 1970s (Cundall and Strack, 1979) as an application of discrete particle kinematics described in classical mechanics from the 1700's.

As shown in Figure 3.4(a), an assembly of particles is generated to represent a natural physical system. Natural systems which may be so represented include soil masses, grain stockpiles, refuse or mineral storage piles, and containers of industrial powders. The boundaries around the assembly must also be defined. Figure 3.4(a) illustrates an assembly with three defined boundaries—two immoveable boundaries preventing movement of the assembly downward and to the right, and a single upper boundary which may be moved vertically. As the upper boundary is moved downward at a velocity, v_B, the boundary eventually contacts Particle 1 of the assembly.

At any time (indicated by subscript {t=1}) after the contact between the upper boundary and Particle 1 the forces acting on Particle 1 are illustrated in Figure 3.4(b). These forces result from the particle's contact with the boundary and with the adjacent Particles 2, 3, and 4. In addition to the forces applied by the boundaries and by adjacent particles, the particle is subjected to the force induced by gravitational acceleration and by an inertial damping force, $\underline{f}_{D\{t=1\}}$, acting in direct opposition of the particle's velocity at time t=1. The vectorial sum of the externally applied forces, gravitational force, and damping force is calculable, as is the vectorial sum of moments of these forces about the particle's center of gravity at $\underline{x}_{(1)\{t=1\}}$.

In conformance with Newton's Second Law, the summations of all forces and moments acting on Particle (i=1) at {t=1} will produce linear and angular accelerations of the particle. These accelerations may then be integrated twice over a very small increment of time, Δt (see Cundall, 1978), to provide an estimate of the "new" position and orientation of Particle 1 at time {t=2}, shown in Figure 3.4(c). In this manner, the position and orientation of Particle 1 may be calculated at any time. In fact, the positions and orientations of all particles in the assembly may be similarly calculated, so that the positions and orientations of all particles are known at all times in the simulation. The behavior of the assembly is then affected by the specified behaviors of the boundaries, by the mass and damping

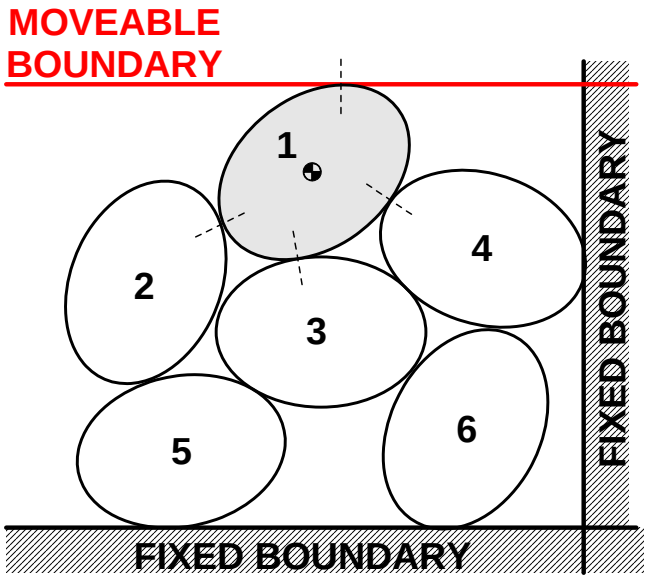

(a)

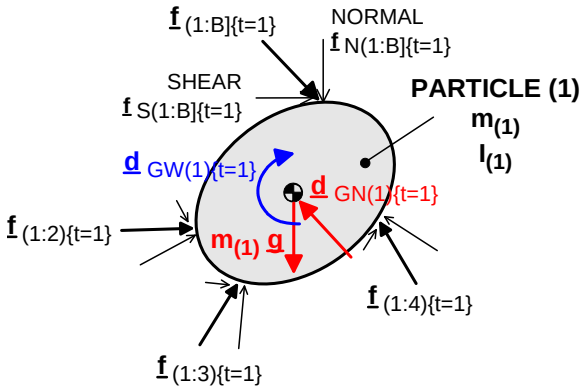

(b)

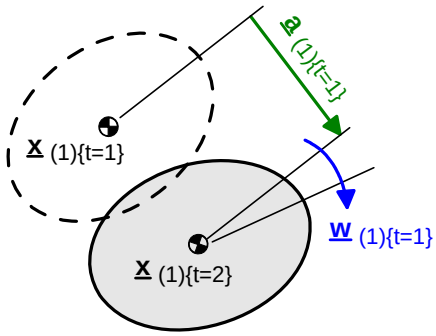

(c)

Figure 3.4 The Discrete Element Method: (a) An Assembly of Particles and Boundaries in Motion, (b) Forces Acting on a Typical Particle, and (c) Motion of a Typical Particle Over a Time Increment.

characteristics of the particle, and by the laws which are used to estimate the forces generated by particle-to-particle and particle-to-boundary interactions.

A typical calculation cycle for the motion of the assembly is shown in Figure 3.5 for a "pseudo-static" application, in which the boundaries of the assembly contain a constant number of particles. The assembly is first generated by placing individual particles, one by one, inside the specified boundaries. This initial particle placement may be randomly generated to conform to any user-specified distributions for particle sizes, particle orientations, or particle shapes, as these distributions are often of interest in studies of the behaviors of granular assemblies. The user may also choose for the assembly to permit variations in particle densities, particle frictional characteristics, and particle damping characteristics, though these additional specifications are less common. The set of user-defined parameters required to generate a particle assembly is shown in Table 3.1.

In subsequent paragraphs, the equations of motion are cast in terms of the motion of a typical particle, Particle (i). By the conventions of this report, Particles are represented by parentheses (i), boundaries are represented by rectangular braces [k], and times are represented by brackets {}. The equations of motion potentially involve the interactions between Particle (i) and several other particles (Particles $j=1,2.3...N_j$), as well as the interactions between Particle (i) and several boundaries (Boundaries $k=1,2,3...N_k$). In fact, the equations of motion are being evaluated for every particle in the entire assembly (i=1,2.3...) at every increment of time (t={t},{t+1},{t+2}...). Each Particle (i) retains a particular number, $N_{k(i)}$, to represent the number of boundaries in contact with Particle (i). Similarly, each particle has its own number, $N_{j(i)}$, to represent the number of other particles in contact with Particle (i).

The number of contacts influencing the behavior of a given particle is permitted to change throughout the simulation as each particle loses contacts with certain particles and gains contacts with other particles. In fact, the majority of the computing effort in discrete element simulations is associated with the detection of contacts within the assembly (Nezami et al, 2006). This efficiency of this effort is increased by maintaining specific information regarding those boundaries and particles in the neighborhood of a specific particle within the assembly. The locations of boundaries and particles within the vicinity of Particle (i), along with parameters used to model the contact between the particle and these neighbors, are

STEP 1
GENERATE ASSEMBLY (SEE TABLE 3.1)
INITIALIZE ALL VALUES IN TABLE 3.1 AND SET $t = t_0$

STEP 2
MOVE BOUNDARIES
$\underline{x}_{[k]\{t\}} = \underline{x}_{[k]\{t-1\}} + \underline{v}_{[k]}\,\Delta t$

STEP 3A UPDATE "NEAREST NEIGHBOR LISTS"
$[\,(\underline{x}_{(i)\{t\}} - \underline{x}_{(j)\{t\}})\cdot(\underline{x}_{(i)\{t\}} - \underline{x}_{(j)\{t\}})\,]^{-1/2} \le 3\varepsilon_{(i)}$
STEP 3B DETECT ALL CONTACTS FOR ALL PARTICLES
Contacts Between Particle (i) and Particles (j)
Contacts Between Particle (i) and Boundaries [k]

STEP 4 SELECT PROPERTIES FOR CONTACTS BETWEEN PARTICLE (i) AND PARTICLE (j) AND BETWEEN PARTICLE (i) AND BOUNDARY [k]

$\alpha_{(i:j)} = \mathrm{MIN}[\alpha_{(i)}, \alpha_{(j)}]$ & $\alpha_{(i:k)} = \mathrm{MIN}[\alpha_{(i)}, \alpha_{[k]}]$
$\beta_{(i:j)} = \mathrm{MIN}[\mu_{(i)}, \mu_{(j)}]$ & $\beta_{(i:k)} = \mathrm{MIN}[\mu_{(i)}, \mu_{[k]}]$
$k_{N(i:j)} = \mathrm{MIN}[k_{N(i)}, k_{N(j)}]$ & $k_{N(i:k)} = \mathrm{MIN}[k_{N(i)}, k_{N[k]}]$
$k_{S(i:j)} = \mathrm{MIN}[k_{S(i)}, k_{S(j)}]$ & $k_{S(i:k)} = \mathrm{MIN}[k_{S(i)}, k_{S[k]}]$
$c_{CN(i:j)} = \mathrm{MIN}[c_{CN(i)}, c_{CN(j)}]$ & $c_{CN(i:k)} = \mathrm{MIN}[c_{CN(i)}, c_{CN[k]}]$
$c_{CS(i:j)} = \mathrm{MIN}[c_{CS(i)}, c_{CS(j)}]$ & $c_{CS(i:k)} = \mathrm{MIN}[c_{CS(i)}, c_{CS[k]}]$
$c_{CF(i:j)} = \mathrm{MIN}[c_{CF(i)}, c_{CF(j)}]$ & $c_{CF(i:k)} = \mathrm{MIN}[c_{CF(i)}, c_{CF[k]}]$

STEP 5A
RELATIVE VELOCITIES AND DISPLACEMENTS AT CONTACTS BETWEEN EACH PARTICLE (i) AND BOUNDARIES [k]

$v_{N(i:k)\{t\}} = (\,\underline{v}_{(i)\{t\}} - \underline{v}_{[k]\{t\}}\,)\cdot\underline{n}_{[k]\{t\}})$
$v_{S(i:k)\{t\}} = (\,\underline{v}_{(i)\{t\}} - \underline{v}_{[k]\{t\}}\,)\cdot\underline{s}_{[k]\{t\}}) + \tfrac{1}{2}\,w_{(i)\{t\}}\,D_{(i)}$
$u_{N(i:k)\{t\}} = u_{N(i:k)\{t-1\}} + v_{N(i:k)\{t\}}\,\Delta t$
$u_{S(i:k)\{t\}} = u_{S(i:k)\{t-1\}} + v_{S(i:k)\{t\}}\,\Delta t$

STEP 5B RELATIVE VELOCITIES AND DISPLACEMENTS AT CONTACTS BETWEEN EACH PARTICLE (i) AND PARTICLES (j)

$\underline{n}_{(i:j)\{t\}} = (\underline{x}_{(j)\{t\}} - \underline{x}_{(i)\{t\}})[\,(\underline{x}_{(j)\{t\}} - \underline{x}_{(i)\{t\}})\cdot(\underline{x}_{(j)\{t\}} - \underline{x}_{(i)\{t\}})\,]^{-1/2}$
$\underline{s}_{(i:j)\{t\}} = \underline{R}\,\underline{n}_{(i:j)\{t\}}$ where $\underline{R}$ is defined as rotation through $\pi/2$ radians
$\underline{v}_{(i:j)\{t\}} = [\,\underline{v}_{(j)\{t\}} - \underline{v}_{(i)\{t\}} - \tfrac{1}{2}\,(|w_{(j)\{t\}}|D_{(j)} - |w_{(i)\{t\}}|D_{(i)})\cdot\underline{s}_{(i:j)\{t\}}\,]$
$v_{N(i:j)\{t\}} = (\,\underline{v}_{(i:j)\{t\}}\cdot\underline{n}_{(i:j)\{t\}})$
$v_{S(i:j)\{t\}} = (\,\underline{v}_{(i:j)\{t\}}\cdot\underline{s}_{(i:j)\{t\}})$
$u_{N(i:j)\{t\}} = u_{N(i:j)\{t-1\}} + v_{N(i:j)\{t\}}\,\Delta t$
$u_{S(i:j)\{t\}} = u_{S(i:j)\{t-1\}} + v_{S(i:j)\{t\}}\,\Delta t$

STEP 6A FORCES ON PARTICLE (i) FROM CONTACTS WITH BOUNDARIES [k]

$\underline{f}_{N(i:k)\{t\}} = u_{N(i:k)\{t\}}\,k_{N(i:k)}\,\underline{n}_{[k]\{t\}}$
$\underline{d}_{CN(i:k)\{t\}} = (v_{N(i:k)\{t\}}\,c_{CN(i:k)})\,\underline{n}_{[k]\{t\}}$
$\delta_{S(i:k)\{t\}} = (\,\alpha_{(i:k)} + \beta_{(i:k)}\,u_{N(i:k)\{t\}}\,k_{N(i:k)}\,)\,/\,k_{S(i:k)}$
$f_{S(i:k)\{t\}} = k_{S(i:k)}u_{S(i:k)\{t\}} - k_{S(i:k)}(u_{S(i:k)\{t\}} - \delta_{S(i:k)\{t\}})\,\text{Ħ}\langle u_{S(i:k)\{t\}} - \delta_{S(i:k)\{t\}}\rangle$
$d_{CS(i:k)\{t\}} = (v_{S(i:k)\{t\}}\,c_{CS(i:k)})(1 - \text{Ħ}\langle u_{S(i:k)\{t\}} - \delta_{S(i:k)\{t\}}\rangle)$
$d_{CF(i:k)\{t\}} = (v_{S(i:k)\{t\}}\,c_{CF(i:k)}(\text{Ħ}\langle u_{S(i:k)\{t\}} - \delta_{S(i:k)\{t\}}\rangle)$

STEP 6B FORCES ON PARTICLE (i) FROM CONTACTS WITH PARTICLES (j)

$\underline{f}_{N(i:j)\{t\}} = u_{N(i:j)\{t\}}\,k_{N(i:j)}\,\underline{n}_{(i:j)\{t\}}$
$\underline{d}_{CN(i:j)\{t\}} = (v_{N(i:j)\{t\}}\,c_{CN(i:j)})\,\underline{n}_{(i:j)\{t\}}$
$\delta_{S(i:j)\{t\}} = (\,\alpha_{(i:j)} + \beta_{(i:j)}\,u_{N(i:j)\{t\}}\,k_{N(i:j)}\,)\,/\,k_{S(i:j)}$
$f_{S(i:j)\{t\}} = k_{S(i:j)}u_{S(i:j)\{t\}} - k_{S(i:j)}(u_{S(i:j)\{t\}} - \delta_{S(i:j)\{t\}})\,\text{Ħ}\langle u_{S(i:j)\{t\}} - \delta_{S(i:j)\{t\}}\rangle$
$d_{CS(i:j)\{t\}} = (v_{S(i:j)\{t\}}\,c_{CS(i:j)})(1 - \text{Ħ}\langle u_{S(i:j)\{t\}} - \delta_{S(i:j)\{t\}}\rangle)$
$d_{CF(i:j)\{t\}} = (v_{S(i:j)\{t\}}\,c_{CF(i:j)}(\text{Ħ}\langle u_{S(i:j)\{t\}} - \delta_{S(i:j)\{t\}}\rangle)$

STEP 7 FIRST APPROXIMATION OF ACCELERATION OF PARTICLE (i) AT TIME {t}

$\underline{a}_{(i)\{t\}} = [\rho_S\,m_{(i)}\underline{g} + \Sigma_j\underline{f}_{N(i:j)\{t\}} + \Sigma_j\underline{d}_{CN(i:j)\{t\}} + \Sigma_k\underline{f}_{N(i:k)\{t\}} + \Sigma_k\underline{d}_{CN(i:k)\{t\}}\,]\,/\,m_{(i)}$
$\omega_{(i)\{t\}} = \tfrac{1}{2}D_{(i)}\,[\Sigma_j f_{S(i:j)\{t\}} + \Sigma_j d_{CS(i:j)\{t\}} + \Sigma_j d_{CF(i:j)\{t\}} + \Sigma_k f_{S(i:k)\{t\}} + \Sigma_k d_{CS(i:k)\{t\}} + \Sigma_k d_{CF(i:k)\{t\}}\,]\,/[\dot{I}_{(i)}$
$\underline{v}_{(i)\{t+1/2\}} = \tfrac{1}{2}\,(\underline{v}_{(i)\{t\}} + \underline{v}_{(i)\{t-1\}}) + \underline{a}_{(i)\{t\}}\,\Delta t$
$w_{(i)\{t+1/2\}} = \tfrac{1}{2}\,(w_{(i)\{t\}} + w_{(i)\{t-1\}}) + \omega_{(i)\{t\}}\,\Delta t$

STEP 8
INCORPORATE GLOBAL DAMPING
$\underline{d}_{GN(i)\{t\}} = -\,(\underline{v}_{(i)\{t+1/2\}}\,c_{GN})\,/\,2$
$d_{GW(i)\{t\}} = -\,(w_{(i)\{t+1/2\}}\,c_{GW})\,/\,2$

STEP 9 REFINED ACCELERATION OF PARTICLE (i) AT TIME {t}

$\underline{a}_{(i)\{t\}} = [\rho_S\,m_{(i)}\underline{g} + \underline{d}_{GN(i)\{t\}} + \Sigma_j\underline{f}_{N(i:j)\{t\}} + \Sigma_j\underline{d}_{CN(i:j)\{t\}} + \Sigma_k\underline{f}_{N(i:k)\{t\}} + \Sigma_k\underline{d}_{CN(i:k)\{t\}}\,]\,/\,m_{(i)}$
$\omega_{(i)\{t\}} = D_{(i)}[d_{GW(i)\{t\}} + \Sigma_j f_{S(i:j)\{t\}} + \Sigma_j d_{CS(i:j)\{t\}} + \Sigma_j d_{CF(i:j)\{t\}} + \Sigma_k f_{S(i:k)\{t\}} + \Sigma_k d_{CS(i:k)\{t\}} + \Sigma_k d_{CF(i:k)\{t\}}\,]/\,[2\dot{I}_{(i)}]$
$\underline{v}_{(i)\{t+1\}} = \underline{v}_{(i)\{t\}} + \underline{a}_{(i)\{t\}}\,\Delta t$
$w_{(i)\{t+1\}} = w_{(i)\{t\}} + \omega_{(i)\{t\}}\,\Delta t$

STEP 10 UPDATE VELOCTY, POSITION & ORIENTATION OF PARTICLES (i)

$\underline{v}_{(i)\{t+1\}} = \underline{v}_{(i)\{t\}} + \underline{a}_{(i)\{t\}}\,\Delta t$
$w_{(i)\{t+1\}} = w_{(i)\{t\}} + \omega_{(i)\{t\}}\,\Delta t$
$\underline{x}_{(i)\{t+1\}} = \underline{x}_{(i)\{t\}} + \underline{v}_{(i)\{t+1\}}\,\Delta t$
$\theta_{(i)\{t+1\}} = \theta_{(i)\{t\}} + w_{(i)\{t+1\}}\,\Delta t$

STEP 11
EVALUATE ERROR
$\mathrm{MAX}\,\|\,(\underline{x}_{(i)\{t+1\}} - \underline{x}_{(i)\{t\}})\cdot(\underline{x}_{(i)\{t+1\}} - \underline{x}_{(i)\{t\}})\,\| < \mathbf{E}_{TOL}$? **OR**
$\Sigma_i\,\|\,(\underline{x}_{(i)\{t+1\}} - \underline{x}_{(i)\{t\}})\cdot(\underline{x}_{(i)\{t+1\}} - \underline{x}_{(i)\{t\}})\,\| < \mathbf{E}_{TOL}$?

NO (ERROR LARGE)

YES (ERROR SMALL)

STEP 12
$t = t + \Delta t$
$\{t\} \rightarrow \{t+1\}$

(STEP 13
STOP

Figure 3.5. Calculation Cycle for Conventional Discrete Element Method.

Table 3.1
User-Defined Parameters in the Distinct Element Method

PARAMETERS WHICH MUST BE DEFINED BY USER
PRIOR TO END OF ASSEMBLY GENERATION PROCESS

FOR EACH PARTICLE (i)	FOR EACH BOUNDARY [k]	FOR ENTIRE ASSEMBLY
Density * $\rho_{(i)}$	**Position** $\underline{x}_{B(k)}$	**Time Increment** Δt
Size * $D_{(i)}$	**Orientation** $\underline{n}_{[k]}$	**Error Tolerance** $\mathbf{E}_{TOL}$
Position and Orientation $\underline{x}_{(i)}$, $\underline{\theta}_{(i)}$	**Surface Adhesion and Friction** $\alpha_{[k]}$, $\beta_{[k]}$	**Global Damping** $c_{GN(i)}$, $c_{GW(i)}$
Shape * $f(\underline{x}_{(i)}, \psi_{1(i)}, \psi_{2(i)}, \psi_{3(i)} \ldots) = 0$ For example, circular shape: $[\underline{\psi}_{(i)}(\underline{x} - \underline{x}_{0(i)})] \cdot [\underline{\psi}_{(i)}(\underline{x} - \underline{x}_{0(i)})] - \psi_2 = 0$	**Contact Stiffness** $k_{N[k]}$, $k_{S[k]}$	**Hydrodynamic Model**** $\rho(\underline{x})$, $\upsilon(\underline{x})$, $h(\underline{x})$, $\mu(\underline{x})$
Surface Adhesion and Friction $\alpha_{(i)}$, $\beta_{(i)}$	**Contact Damping** $c_{CN[k]}$, $c_{CS[k]}$, $c_{CF[k]}$	**Apparent Mass Coefficient**** κ
Contact Stiffness $k_{N(i)}$ and $k_{S(i)}$	**Type** Displacement-Controlled Force-Controlled	**Global Distributions** Particle Densities Particle Sizes Particle Orientations Particle Shapes Particle Surface Strengths Particle Contact Stiffnesses Particle Contact Damping
Contact Damping $c_{CN(i)}$, $c_{CS(i)}$, $c_{CF(i)}$	**Velocity** $\underline{v}_{[k]}$ (Displacement Controlled)	
Averaging Neighborhood $\varepsilon_{(i)}$	**OR**	
	Force $\underline{f}_{[k]}$ (Force-Controlled)	

***** Prescription of these parameters permits the calculation of several additional parameters associated with the particle: $m_{(i)}$, $V_{(i)}$, $\dot{I}_{(i)}$, $A_{(i)}$

** These additional parameters must be extracted from the results of a completed hydrodynamic model to permit coupling between the DEM and fluid flow as described in this report.

maintained in "nearest neighbor lists." These lists are updated for each particle at every time step of the simulation.

Once the assembly is generated, the boundaries are moved over a distance defined by the user-specified boundary velocities acting over a small increment of time, Δt. This motion will eventually force the boundaries to contact one or more particles in the assembly. A subroutine (identified as Step 3 in Figure 3.5) is undertaken at the outset of each calculation to investigate which particles and boundaries contact each particle in the entire assembly. A contact is assumed to exist when the boundary of a particle (defined as a mathematical surface referenced to the particle's center of gravity) is "penetrated" by the plane or surface representing an assembly boundary or adjacent particle, respectively. That is, over relatively small distances, a spatial overlap is permitted to exist, where portions of two particles may occupy the same space. This simplification is illustrated in Figure 3.6(a)

This spatial overlap violates strict application of the conservation of mass at the particle level. In reality, a compression contact of two particles would function as a tractive stress. A portion of the energy of the tractive stress on the particle boundary would then be store in the strain energy associated with distortion of the particle, as shown in Figure 3.6(b). This distortion would permit the particle centers to become closer. The discrete element method thus uses the distance between two contacting particles (i.e., the particle "overlap") as a proxy for the combined distortion of the two particles induced by the compressive force acting at the particles' shared contact. Because the overlap distance between particle centers represents particle distortion induced by forces at the contact, the behavior at the boundary may be simplified to a relationship between the particles' overlap distance and the force acting at the contact. Through this rationale, conservation of mass may be assumed to remain valid for the assembly, though it is not precisely enforced upon each particle.

The means by which contacts are detected and the magnitudes of any overlaps are evaluated is a relatively complex geometrical problem. This problem is undertaken six or seven times for each particle in the assembly at each increment of time in the simulation. This "contact detection algorithm" represents the most computationally intensive portion of most discrete element simulations. The number of detection calculations scales exponentially with the number of particles in the simulation, and "pseudo static" simulations typically involve a minimum of 1,000 particles. To minimize the computational effort

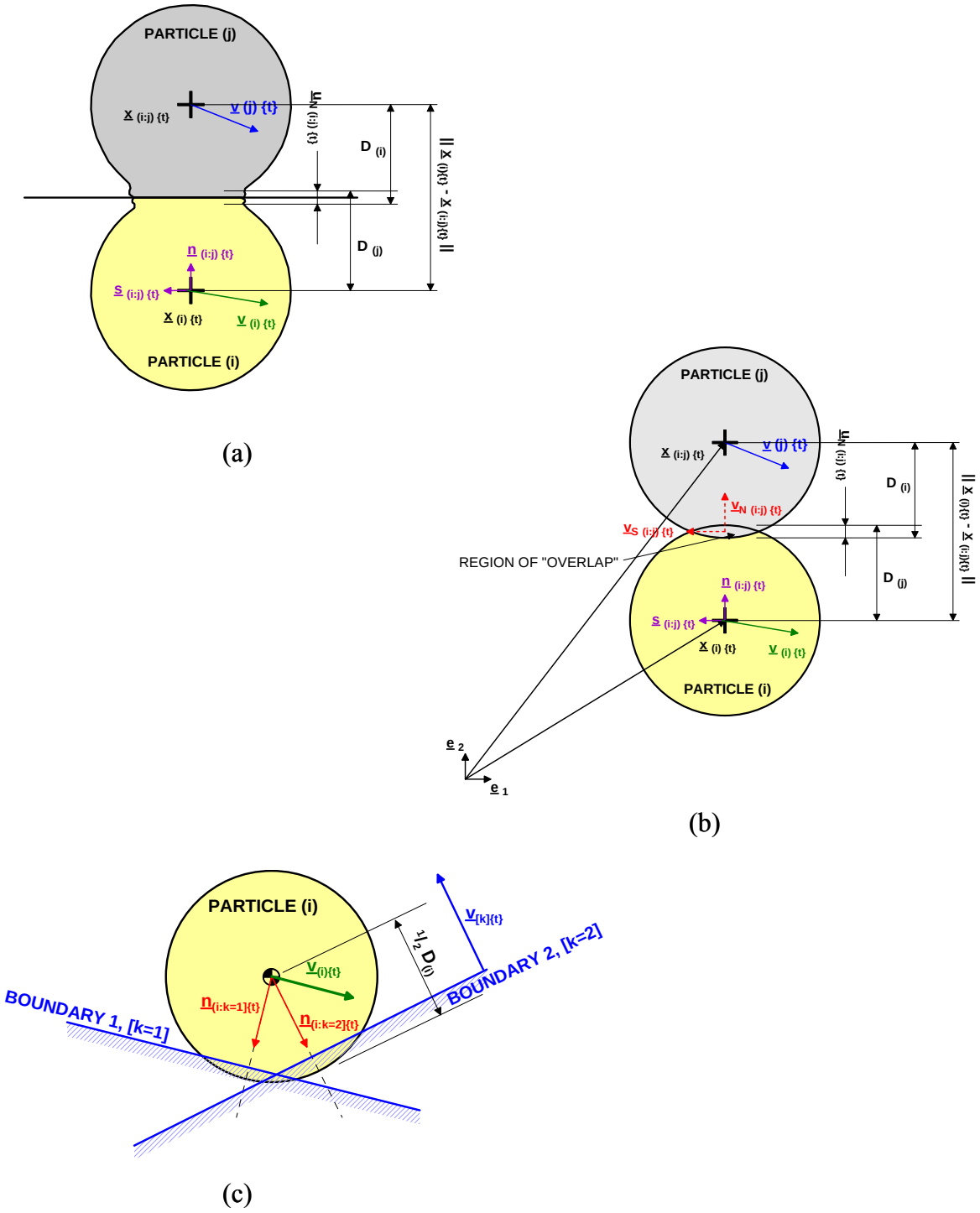

Figure 3.6 Particle Contact Behaviors for (a) Actual Geometry at Particle-to-Particle Contact, (b) Idealized Geometry at Particle-to-Particle Contact, and (c) Idealized Geometry at Particle-to-Boundary Contact.

required for discrete element simulations, several contact-detection algorithms have been developed. These routines generally incorporate some technique for partitioning the overall assembly into subregions and for maintaining lists of particles and boundaries within a certain neighborhood (defined by an appropriate length scale, ε) around each particle's center of gravity. Once all contacts are known for all particles, a set of physical properties is then assigned to represent the behaviors at each of the contacts (Step 4 of Figure 3.5) existing for a given particle. These properties are generally taken as the smaller of the values assigned to the particle or those assigned to the contacting boundaries or particles.

The forces acting on each particle, through its contact with one or more boundaries and/or its contacts with one or more adjacent particles, are then estimated (in Step 5 of Figure 3.5). This step amounts to a prescription of the microscopic constitutive behaviors. Discrete element models commonly rely upon relatively simple constitutive models to represent the particle-to-particle and particle-to-boundary interactions. The normally-directed component of each contact between a particle and a neighboring particle or boundary is assumed to be represented by the simple rheological models shown in Figure 3.7.

As shown in Figure 3.7(a), normal forces at particle contacts are generated from the combination of a static contact normal force and a dynamic contact normal damping force. The static contact normal force acting at the contact between particle (i) and particle (j) is assumed to be linearly related to the "overlap distance," as illustrated in Figure 3.7(b). The constant defining this relationship is termed the static contact normal stiffness ($k_{N(i:j)}$). The dynamic contact normal force is assumed to be linearly related to the component of the collision velocity acting normal to each particle at the contact, as illustrated in Figure 3.7(c). The constant defining this relationship is the contact normal damping parameter ($c_{CN(i:j)}$). A locally defined vector system, aligned normal ($\underline{n}_{(i:j)}$) and tangential ($\underline{s}_{(i:j)}$) to the surface of the particles, is used to define the normal component of the collision velocity at the contact (see Step 5 of Figure 3.5). In the case of circular or spherical particles, the locally defined normal vector will also align with the vector defined by the difference in the two particles' positions. While the concepts of motion for particles and assemblies described in this report are applicable to an assembly involving any particle shapes, the equations of Steps 5 through 9 of Figure 3.5 are specifically limited to circular or spherical particles.

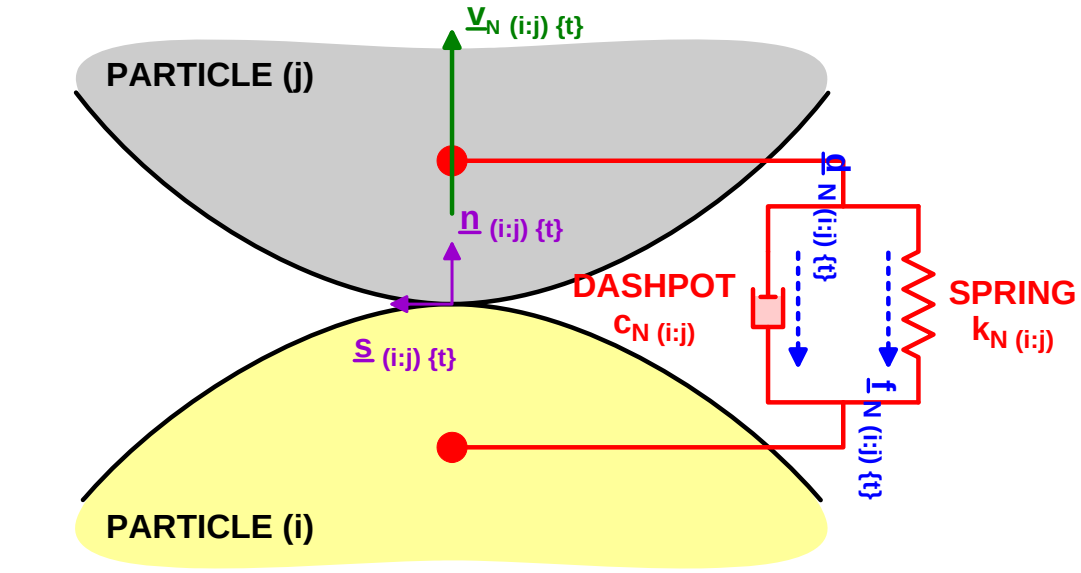

(a)

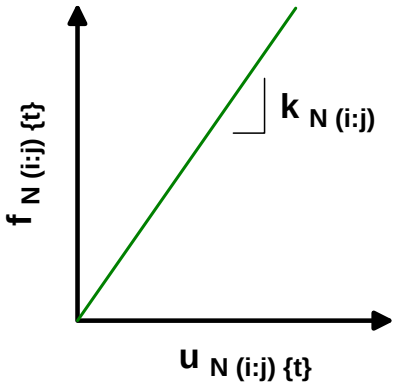

(b)

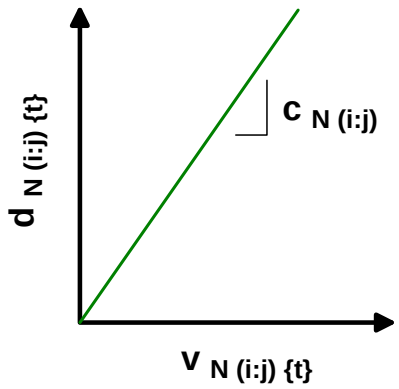

(c)

Figure 3.7 Normal Forces Generated at Interparticle Contact. (a) Rheological Model of Contact, (b) Relationship Between Normal Static Force and Relative Normal Displacement, (c) Relationship Between Normal Damping Force and Velocity of Relative Normal Displacement.

The shearing force which may be generated at a contact also has static and dynamic components, as shown in Figure 3.8(a). The static contact shear force of Figure 3.8(b) is related to the accumulated relative displacement of points on the surface of each particle (as referenced to points on the surface of each particle defined at the instant contact is detected). This relative surface displacement, $u_{S(i:j)\{t\}}$, is calculated by integrating the relative tangential velocity at the contact location over the time increment Δt and adding the resulting displacement to that which existing prior to the time increment, $u_{S(i:j)\{t-1\}}$ (see Step 5B of Figure 3.5). At large relative displacements, the static contact shear force may be limited to a value defined by the available static shearing resistance at the contact. The available static shearing resistance at the contact, is estimated from a simple Coulomb adhesion-friction law incorporating the magnitude of the static contact normal force, as shown in Figure 3.8(c).

At displacements less than that corresponding to particle slip, $\hat{u}_{S(i:j)\{t\}}$, the shear force at the contact is linearly related to the relative displacement through the static contact shear stiffness ($k_{S(i:j)}$). At greater displacements, the shear force at the contact is limited to the available shearing resistance at the contact. Within the equations of Figure 3.5, the limitation on the static contact shear force is enforced by the Heaviside function, $H\langle u_{S(i:j)\{t\}} - \hat{u}_{S(i:j)\{t\}} \rangle$, where the argument of the Heaviside function represents that portion of the relative displacement that is attributable to the particles' "plastic slip." This introduces the notion that a portion of the energy applied to the assembly is being dissipated through friction at particle contacts.

As shown in Figure 3.8(c), the dynamic component of the contact shear force is linearly related to the tangential component of the collision velocity through the contact shear damping coefficient, $c_{CS(i:j)}$, or the contact friction damping coefficient, $c_{CF(i:j)}$. The contact shear damping coefficient is assumed to apply at displacements smaller than that corresponding to particle slip, and the contact friction damping coefficient is applied when displacements are larger than that corresponding to particle slip.

The majority of the forces acting on a particle in a quasi-static simulation are determined from the application of these constitutive laws at the particle contacts. Each particle is also typically assumed to subjected to a force associated with gravitational acceleration of its mass. In addition to these forces, global damping forces are often applied to the motion of the particle. A force is applied to the center of gravity of the particle to

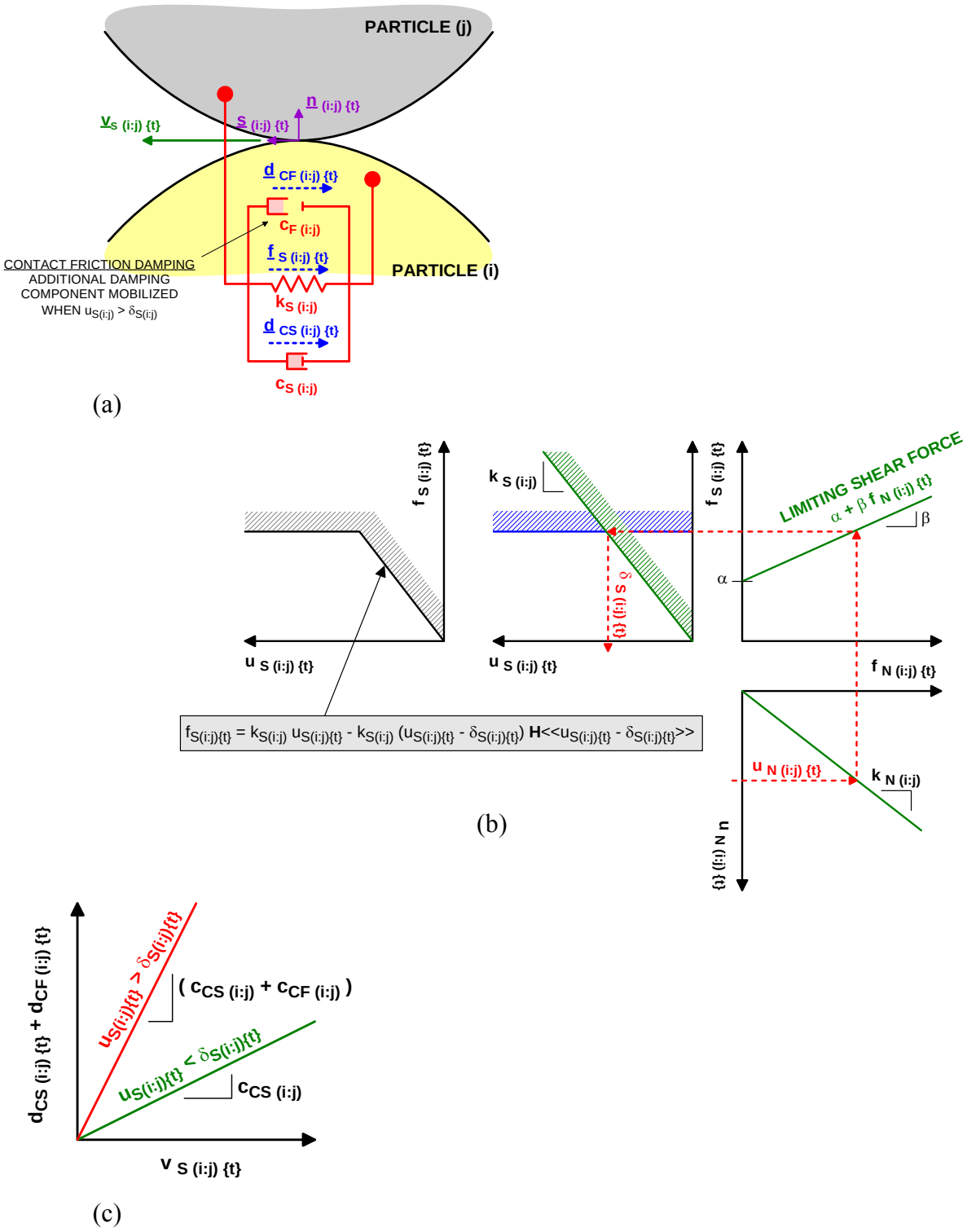

Figure 3.8 Shear Forces Generated at Interparticle Contact. (a) Rheological Model of Contact, (b) Relationship Between Shear Static Force and Relative Shear Displacement, (c) Relationship Between Shear Damping Force and Velocity of Relative Shear Displacement.

oppose the particle's current velocity vector, and the magnitude of this force is taken as a fraction of the particle's current velocity. This fraction is defined by the global linear damping coefficient, c_{GN}. The rotation of the particle is similarly damped by a torque applied to oppose the particle's current angular velocity. The magnitude of the damping torque is related to the particle's angular velocity through the global shear damping coefficient, c_{GS}. Because the damping forces are associated with particle linear and angular velocities, a preliminary estimate of these velocities is often assembled for the upcoming time increment (see Steps 7 and 8 of Figure 3.5). When the mass of the particle, $m_{(i)}$, and its polar moment of inertia, $J_{(i)}$, are considered in subsequent force summations, the global damping forces may be interpreted as inertial damping of the particle motion.

As shown in Step 9 of Figure 3.5, the forces acting on each particle in the assembly are used to estimate the particle's linear acceleration ($\underline{a}_{(i:j)\{t\}}$) and angular accelerations ($\omega_{(i:j)\{t\}}$) through the upcoming time increment. These linear and angular accelerations are then integrated over the time increment, Δt, to produce vectors representing the changes in the linear and angular velocities of Particle 1 over the time increment between {t} and {t+1}. These changes in velocity may be added to the linear and angular velocities existing at time {t} to provide an updated estimate of the particle's linear velocity ($\underline{v}_{(i:j)\{t+1\}}$) and angular velocity ($w_{(i:j)\{t+1\}}$). Similarly, the updated increments of each particle's linear and angular velocities may be integrated over the time increment to provide an estimate of changes in each particle's position and orientation occurring over the time increment Δt. These changes are added to each particle's position and orientation at the beginning of the time increment so that each particle's position ($\underline{x}_{(i:j)\{t+1\}}$) and orientation ($\theta_{(i:j)\{t+1\}}$) are known at the ending of the increment (also, the beginning of the next increment).

The equations shown in Figure 3.5 represent a central difference approximation in time (Cundall and Strack, 1979; Feng, 2005). Most of the forces acting on the particle are generated in a "backward difference" sense, as they employ displacements and velocities acting at the beginning of the time increment. The global linear and angular damping forces are an exception, as these forces are estimated from preliminary estimates of the velocities which will occur over the forthcoming time increment. In this sense, the global damping forces are generated as "forward differences." Particle accelerations result from the forces estimated by this combination of backward and forward differences. As these accelerations

and the updated velocities are applied over the upcoming increment of time, the particle velocities and displacements are also best described as "forward differences." Variations on this basic scheme exist and are primarily related to the displacements and velocities used to estimate the global damping forces.

At the end of a time increment within the DEM calculation cycle, the displacements of all particles over the increment are known (see Step 10 of Figure 3.5). The assembly is said to be in a state of equilibrium when the motions of all particles are zero, so that none of the particles is displaced over a single increment of time. This measure of equilibrium may be stated as a criterion on the largest displacement of any particle in the assembly, or as a criterion on the accumulated displacements of all particles in the assembly. As indicated in Step 11 of Figure 3.5, the error measure for the former criterion is obtained by computing the norm of the displacement for each particle over the increment (formed by the square root of the inner product of the particle displacement with itself). The maximum value of this error is then compared to a user-specified scalar value, $\mathbf{E}_{\mathrm{TOL}}$, representing the maximum displacement of any one particle. The latter criterion may be obtained by computing the norm of all particle displacements and summing these norms to a single scalar value. This scalar value is then compared to the user-specified scalar value, $\mathbf{E}_{\mathrm{TOL}}$, which then represents an averaged displacement for the assembly.

Within the DEM, the trajectory of a single particle is not explicitly tied to the motions of any other particle, except through the influence of discrete interactions that occur during contact with adjacent particles or domain boundaries. Particle motions may be influenced by adjacent particles and boundaries, but they are not directly affixed to the motions of any other particles or to the domain boundaries. This assumption marks a fundamental difference between the DEM and assumed kinematic constraints of the sort associated with discrete nodal unknowns within Cosserat continuum simulations employing the Finite Element Method (FEM).

Through systematic calculations of the sort described here, the DEM provides a means of interpreting the overall behaviors of an assembly of particles. These overall behaviors arise from the application of fundamental and relatively simple physical laws. Critics of the technique identify its failures to precisely preserve all physical laws at the particle-level (e.g., the approximation to conservation of mass at particle contacts). In

addition, the technique enforces user-defined assumptions regarding the relationships between forces and displacements at particle contacts, though these relationships are not well understood. Despite these limitations, the DEM appears to faithfully reproduce important behaviors of granular materials (e.g., pressure-dependency of strength, shear dilatancy, inherent and induced stress anisotropy, and creeping strain behaviors) at the "global" level. The fidelity of DEM models in reproducing overall behaviors of an assembly implies a truthfulness in the models which have been assumed to represent interparticle contacts. For this reason, the technique has gained widespread acceptance in the development of constitutive equations (Sitharan et al, 2002; Yao and Anandarajah, 2003; Jiang et al, 2006; Kock and Huhn, 2007). In addition, gains in computational power, massively parallel programming techniques, and algorithmic efficiency have extended the sizes of problems which may be considered (e.g., Heyes, 2004). Recent work indicates that assemblies as large as 10,000,000 particles may be solved to steady state equilibrium within one day using commonly available desktop computers.

The inability to obtain high-quality measurements of the constitutive parameters defining interparticle contacts underscores the need for a high level of model calibration. As is the case with any model, DEM simulations must be calibrated against physical observations. In the case of the DEM, these physical observations are typically obtained for an assembly, and not for individual particles. The veracity of the model, at least at the particle level, is extrapolated from the veracity of the model in reproducing the behavior of an assembly.

The tracking of individual particle trajectories within the DEM makes the technique ideally suited for simulating a wide variety of problems including: "near continuum" behaviors (e.g., dense packing of soil particles subjected to quasi-static loadings, as in Zeghal and Sharmy, 2004); transitional behaviors (e.g., the shaking of a continuous, unfractured rock masses into one in which fracture planes divide the mass into blocks, as in Koyama and Jing, 2007); and fully discontinuous" behaviors (e.g., blasting and fragmentation, as in Owen et al, 2004). The flexibility of the technique in quasi-static constitutive modeling has led to reported applications in large-scale solid mechanics problems such as slope instability (Staron and Hinch, 2007), tunnel stability (Labra et al, 2008), powder production (Sanfratello et al, 2008; Cleary and Morrison, 2009), and oil-well production (Jensen and Preece, 2009).

In general, the description of particle motions provided so far in this is adequate for problems in which (a) the motion of particles is not influenced by any forces besides those imposed by gravity, the assembly boundaries, and interparticle contacts, and (b) the number of particles within the assembly boundary is essentially constant. The difficulty associated with the incorporation of additional forces into the DEM is directly related to the difficulty in estimating the magnitude of the additional forces. If the additional forces may be calculated with relative ease, it is straightforward to include these additional forces in the DEM calculation cycle. Magnetic forces, for example, are relatively easy to include if the magnetic field is referenced to existing assembly boundaries (Fazekas et al, 2001). The additional magnetodynamic force acting on a particle may be characterized entirely by the particle's size and position within the assembly. As both of these parameters are already included in the calculation scheme, the inclusion of the additional force is straightforward. In contrast, the incorporation of interparticle attractive and repulsive forces (Anandarajah and Yao, 2003) requires a significant computational effort beyond that which would be required for the basic scheme shown in Figure 3.5.

The limitations of the current scheme regarding the number of particles in the assembly may also be removed with relative ease, so long as two assumptions are observed. First, the rate at which new particles are introduced to the assembly must not be significantly greater than rate at which particles exit the assembly. Second, the growth in the number of particles must not be generated by the splitting of particles within the existing assembly. Sediment transport is an important problem which generally conforms to these two assumptions when the sediment is being transported at a "steady state" concentration or when the sediment concentration is extremely low. The DEM has been successfully applied to a limited number of sediment transport problems (Sun and Li, 2001; Calantoni et al, 2004; Heald et al, 2004; and Hobbs, 2009). However, these applications have require certain modifications to the basic calculation scheme depicted in Figure 3.5. The remaining section of this chapter will describe fundamental behaviors which must be considered when modifying the DEM to accommodate dispersed sediment transport problems involving low sediment concentrations.

3.2.3 Multi-Phase Fluid Dynamics

Multi-phase fluid dynamics was developed to describe the motion of a collection of particles within a surrounding continuum. In general, the particles may be formed from solid, liquid, or gas, and these particles move through a surrounding continuum that is assumed to be a liquid or a gas. These flows are typically categorized by the concentration of the particles as a fraction of the surrounding continuum, as various concentration levels correspond to different types of forces influencing the particle motions. For the case of "sparse" multi-phase flow, the trajectories of individual particles are governed by their interaction with the surrounding fluid (as opposed to their interaction with boundaries or other particles). This definition would apply to a case in which a relatively small number of particles are entrained within a fluid flow within a domain that is relatively large, when compared to the size of an individual particle. In this sense, the problem of levee breach closure may be described as a sparse multi-phase, at least during that part of a particle trajectory occurring prior to impact with other particles. Once particle impact has occurred, the behaviors of the various particles in the assembly are well represented by the form of the DEM described in the previous section.

For the purposes of this report, the researchers consider particles to consist of solid matter having a non-buoyant specific gravity of solids (G_S) greater than 2.5. The surrounding continuum will consist of fluid matter having a specific gravity of 1. This specific case removes certain complications associated with surface tension, particle miscibility, particle distortion, and particle flotation. The multi-phase flow will further be considered as an uncoupled process, in the sense that the flow conditions will be assumed to remain unmodified by the introduction of a single particle into the flow. This assumption does not imply the flow conditions are not altered over the history of a simulation. However, flow conditions will be assumed constant between the time a single particle is introduced into the flow and the time at which that particle comes to rest. This assumption implies that a single particle does not strongly influence the flow field associated with those conditions present prior to insertion of the particle into the flow. This may not strictly be the case, and may be significantly in error during the latest stages of breach closure. However, this assumption is conservative in its application to the problem of breach closure, as it will generally result in overestimates of the fluid forces influencing the particle trajectory.

In the case of uncoupled fluid flow, the relative velocity between the particle and the fluid ($\underline{r}_{(i)\{t\}}$) may be taken as the difference between the particle velocity ($\underline{v}_{(i)\{t\}}$) and the unhindered fluid velocity ($\underline{\square}_{\{t\}}$), as illustrated in Figure 3.9. The unhindered fluid velocity is that which would be observed throughout the domain if no particles were present. It may be obtained throughout a defined problem domain via a hydrodynamic simulation of the sort described previously in this chapter.

Interactions between the particle and the fluid are permitted during the uncoupled fluid flow, though these interactions are assumed to leave the flow field unmodified. The forces which generate linear acceleration of the particle during a sparse multi-phase flow are described within the Basset-Boussinesq-Oseen equations of particle motion:

$$m\,\underline{\mathbf{a}} = \underline{\mathbf{f}}_A + \underline{\mathbf{f}}_B + \underline{\mathbf{f}}_D + \underline{\mathbf{f}}_G + \underline{\mathbf{f}}_H + \Sigma\,\underline{\mathbf{f}}_N + \Sigma\,\underline{\mathbf{f}}_S \qquad (3.9) \qquad \text{(vector)}$$

The last two terms of Equation 3.9 arise from particle interactions with other particles or with boundaries. The remaining terms form the following forces acting on the entrained particle:

buoyancy
$$\underline{\mathbf{f}}_B = -\,\rho_F\, V\, \underline{\mathbf{g}} \qquad (3.10) \qquad \text{(vector)}$$

drag
$$\underline{\mathbf{f}}_D = -C_D\,\pi\,\rho_F\,(D^2/8)\,(\underline{\mathbf{r}}\,.\,\underline{\mathbf{r}})\,|\,\underline{\mathbf{r}}\,| \qquad (3.11) \qquad \text{(vector)}$$

apparent mass
$$\underline{\mathbf{f}}_A = -\,\rho_F\,\kappa\,V\,(d\underline{\mathbf{r}}/dt) \qquad (3.12) \qquad \text{(vector)}$$

Basset force
$$\underline{\mathbf{f}}_H = -\frac{3}{2} D^2 \sqrt{\pi\,\rho_F\,\mu}\left[\int_0^t \frac{d\underline{r}}{dt}\frac{1}{\sqrt{t-t^*}}\,dt^* + \frac{\underline{r}_{(t=0)}}{\sqrt{t}}\right] \qquad (3.13) \qquad \text{(vector)}$$

gravity
$$\underline{\mathbf{f}}_G = \rho_S\, V\, \underline{\mathbf{g}} \qquad (3.14) \qquad \text{(vector)}$$

Equation 3.10 describes the static buoyancy force exerted by the fluid on the particle volume. This buoyancy force acts to oppose the gravitational force exerted on the particle's mass. Equation 3.11 describes the viscous force exerted by frictional drag along the surface of the particle. The drag force acts as a sort of "global damping force" as its magnitude is proportional to the relative velocity between the particle and the fluid. The drag force acts opposite to the direction of the relative velocity. Equation 3.12 describes an apparent mass acceleration. This represents the force required to alter the acceleration of the fluid mass which would occupy the volume of the particle in the unhindered velocity field. The force is assumed to act in the direction of the fluid acceleration, and this direction may be extracted from the unhindered velocity field obtained from a hydrodynamic simulation. The apparent mass of this fluid volume must also be added to the particle mass used to determine the particle's acceleration. This is typically achieved by multiplying the true particle mass ($m_{P(i)}$) by a factor equal to $1+\kappa$, where κ is the apparent mass coefficient. The apparent mass coefficient for spheres is taken as 0.5. When the specific gravity of the solids forming the particle is

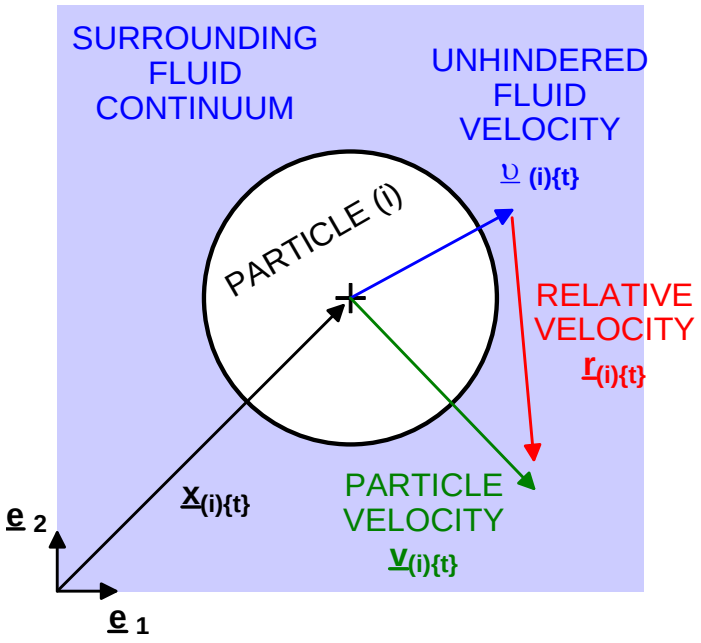

(a)

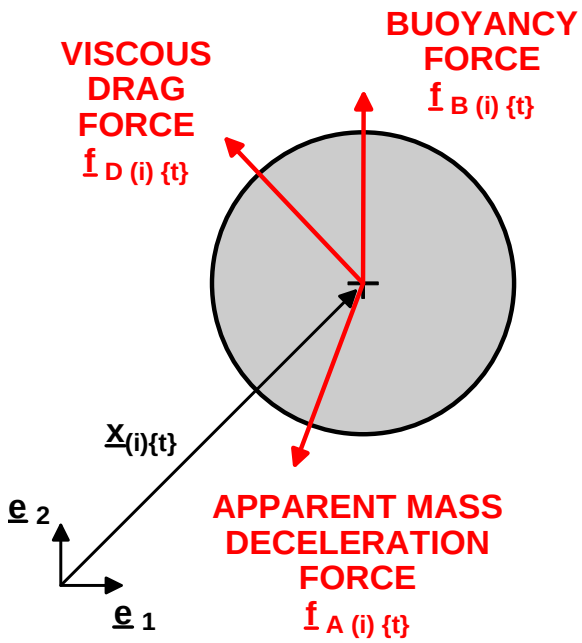

(b)

Figure 3.9 A Sparse Multiphase Flow: (a) Interaction of Particle and Fluid Due to Differences in Velocities, and (b) Resulting Forces Imposed Solely by Fluid Continuum in Vicinity of Particle.

taken as G_S=2.65, the effective particle mass which must be accelerated is approximately 15 percent greater than the true mass of the particle

Equation 3.13 describes the "so called" Basset Force. This force is a drag force associated with unsteady development of the viscous boundary layer creating drag. This force is history dependent, and its influence decreases significantly with increasing time after development of the boundary layer. The Basset Force varies directly with particle acceleration, though it is generally small for accelerations smaller than that attributable to gravity. The force varies inversely with both the particle Reynolds number and the specific gravity of solids for the particle and is often assumed to equal zero for non-creeping flow conditions. For these reasons, the Basset Force is not explicitly considered in subsequent sections of this report.

The viscous drag force (defined in Equation 3.11) is seen to vary linearly with the relative velocity between the particle and the fluid. In reality, this variation is nonlinear, as the drag coefficient has been observed to be a function of the particle Reynold's number. The entrainment of large masses (e.g., 0.3- to 2-m diameter spheres, corresponding to 1- to 6.6-ft diameter spheres) into the floodwaters flowing through a levee breach presents a situation in which the particle Reynolds number may vary over an extremely large range. For this reason, the conditions generating important nonlinear behavior of the drag forces are described here.

At very low Reynolds numbers, the fluid velocity field (actually the field of relative velocities, ($\underline{r}_{(i)\{t\}}$) around the particle is depicted by Point A in Figure 3.10. For this discussion, the front of the particle is assumed to face directly into the fluid flow generated by the relative velocity between the particle and the fluid. The flow around the particle is laminar, and the region of the fluid which is disturbed by a relative motion between the particle and the fluid is relatively large. The drag forces associated with a given relative velocity are seen to be very large in this "viscous" flow condition. As the Reynolds's number increases, through increases in the magnitude of the relative velocity, the disturbance to the fluid flow field becomes localized into a boundary layer around the particle, as illustrated at Points B and C of Figure 3.10. Minimization of the boundary layer thickness results in a reduction of the drag forces associated with a given relative velocity to a local minimum at the conditions defined by Point C.

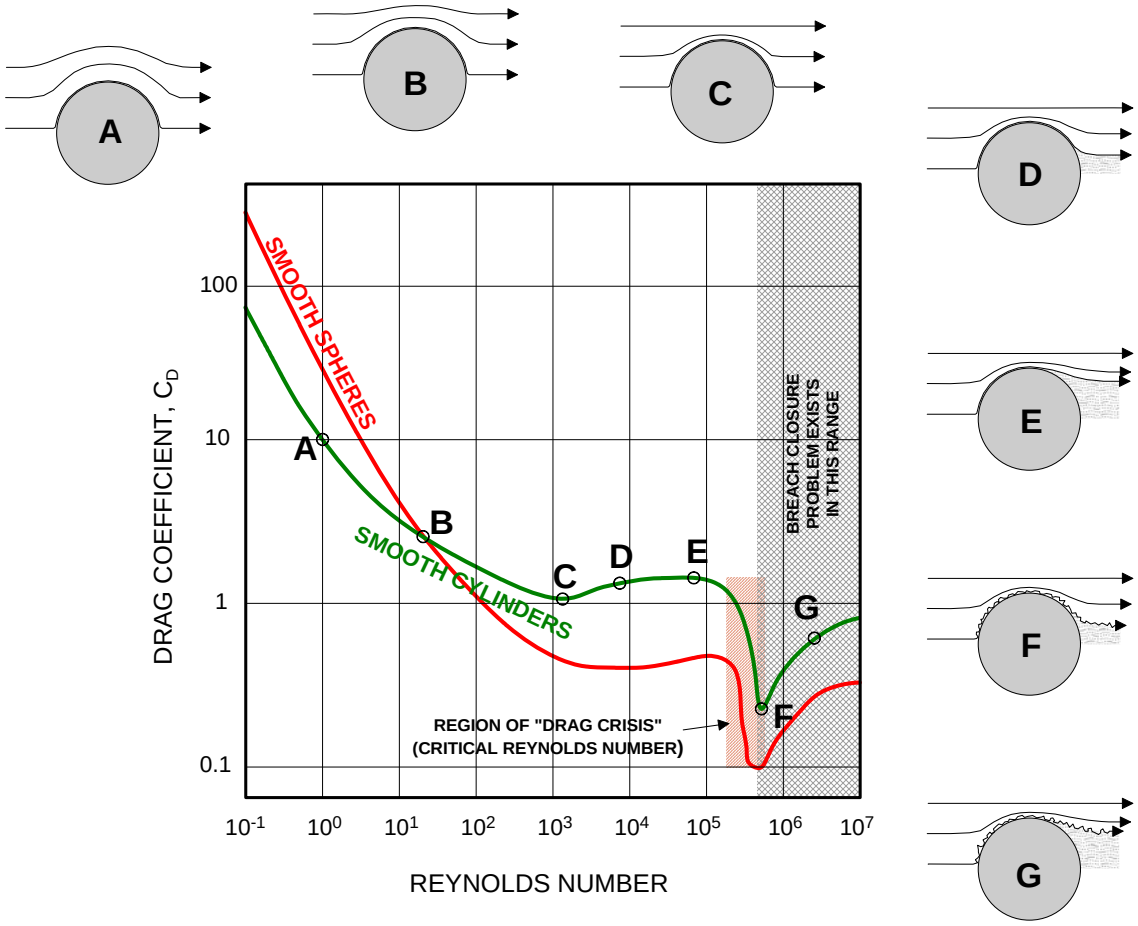

Figure 3.10 Drag Coefficients for Smooth Spheres and Cylinders.

With increasing Reynolds number (associated with increases in the magnitude of the relative velocity), the streamlines defining the fluid flow begin to detach from the surface of the particle. The separation of streamlines from the particle surface is initiated at the rear of the particle, and the detached region grows with increasing Reynolds numbers, as illustrated in the sequence from Point C to Point E. The increasing detachment of the boundary layer results in a decrease in the pressure recovery on the rear side of the particle, where eddies begin to develop. This decreased pressure recovery leads to a gradual increase in the drag forces to the point at which the boundary layer is detached across the entire surface area of the rear face of the particle (see Point E).

Further increases in the relative velocity lead to drastic reductions in the drag coefficient over a very narrow band of relative velocities just greater than those associated with Point E. This condition, illustrated by the steeply sloping curve from Point E to Point F, corresponds to the so-called "drag crisis." The drag crisis is defined by rapidly developing turbulent instability within the boundary layer. This turbulence within the boundary layer causes the eddying wake to quickly collapse, and this collapsed eddy field is illustrated by the conditions at Point F. The "reattachment" of the now-turbulent boundary layer is short-lived, as the eddy field behind the particle again grows with increasing particle Reynolds numbers. This second expansion of the eddy field again causes a gradual rise in the drag coefficient, illustrated by movement from Point F to Point G. As with the first observed increases in the drag coefficient (between Points C and E), this second gradual increase in the drag coefficient occurs under the influence of decreased pressure recovery on the rear face of the particle.

The onset of the drag crisis is commonly observed at particle Reynolds numbers in the range of $1x10^5 \leq \mathbb{R}_P \leq$to $1x10^6$. Examination of the form of the particle Reynolds number indicates the drag crisis should be anticipated for large particles, surrounded by a fluid flow field of high velocities, within a fluid having a relatively low kinematic viscosity. This combination is commonly present within the conditions associated with an attempted levee breach closure using large diameter solid masses. For comparison, a 1.5-m (4.9-ft) diameter particle entrained within floodwaters flowing at a velocity of 6 m/s (20 ft/s), measured relative to the particle velocity, would create a particle Reynolds number of $9x10^6$.

The variation of the drag coefficient with particle Reynolds number is typically obtained through experimental observation of the forces exerted on fixed spheres subjected to ambient velocity fields in a wind tunnel. In these experiments, the drag coefficient is back-calculated from the known value of the particle Reynolds number associated with the applied ambient velocity field and the experimentally-observed forces acting on the particle. This experimental arrangement relies upon the specification of natural boundary conditions (the flow field velocity) to describe the relative motion of the particle and fluid. This differs slightly from the case of a solid mass free-falling through a fluid, where the relative motion of the particle and fluid is prescribed through a force equilibrium. For this reason, small discrepancies may exist between experimental observations of drag derived from wind tunnels and those derived from free-fall experiments (Lyotard et al, 2007). These discrepancies are generally considered to be negligible. On this basis, a piecewise series of curve-fits may be used to conveniently reduce a representative, experimentally-observed relationship between the drag coefficient and the particle Reynolds number, as shown in Table 3.2.

The onset of the drag crisis is related to the roughness of the particle surface, so that roughened surfaces often induce the drag crisis at lower Reynolds numbers than smooth surfaces. This experimentally observed phenomenon may be exploited, as is done by golf ball designers, to decrease the velocity at which the drag coefficient is greatly reduced, thereby slowing the deceleration of the ball. In the case of DEM applications to levee breach closure, an apparent uncertainty in the forces acting on a particle entrained in the fluid flow is introduced by uncertainty in the onset of the drag crisis. However, because the DEM relies heavily upon model calibration for an assembly, errors in a single model parameter (e.g., uncertainty in the onset of the drag crisis through variations in the particle surface roughness or the fluid viscosity) may be covariant with errors generated by an entirely different model parameter. For this reason, the overall error in the simulation must be reduced by proper calibration of the model against a set of physical observations collected during experiments representing conditions similar to those to be modeled. The DEM thus presents a useful tool for scaling experimental results to a larger physical domain involving a similar fundamental problem.

Table 3.2
Observed Relationships Between the Drag Coefficient
and Reynolds Number for Smooth Spheres

APPROPRIATE RANGE OF REYNOLDS NUMBERS	EQUATION FOR SPHERICAL DRAG COEFFICIENT	
$0 \leq R \leq 1.00 \times 10^{0}$	$C_D = \frac{24}{R}$	Stokes
$1.00 \times 10^{0} \leq R \leq 7.00 \times 10^{2}$	$C_D = \frac{24}{R}\left(1 + 0.15^{0.687}\right)$	
$7.00 \times 10^{2} \leq R \leq 1.04 \times 10^{4}$	$C_D = [\sqrt{\frac{24}{R}} + 0.34\left(R^{0.06} + \frac{1}{1.72 + 0.018R}\right)]^{2}$	Carey, 1970
$1.04 \times 10^{4} \leq R \leq 1.50 \times 10^{5}$	$C_D = 0.49 + \frac{24}{R} + \frac{3.73}{\sqrt{R}} - \frac{4.83x10^{-3}\sqrt{R}}{1 + 3.00x10^{-6} R^{3/2}}$	
$1.50 \times 10^{5} \leq R \leq 2.60 \times 10^{5}$	$C_D = -3.013x10^{-7} R + 0.5187$	Weiselsberger, 1979
$2.60 \times 10^{5} \leq R \leq 3.00 \times 10^{5}$	$C_D = -1.400x10^{-6} R + 0.8020$	Weiselsberger, 1979
$3.00 \times 10^{5} \leq R \leq 3.79 \times 10^{5}$	$C_D = -3.0144x10^{-6} R + 1.2350$	Weiselsberger, 1979
$3.79 \times 10^{5} \leq R$	$C_D = 5.700x10^{-8} R + 0.0709$	Weiselsberger, 1979

CHAPTER 4

AN ALGORITHM FOR DISCRETE ELEMENT SIMULATIONS OF MULTI-PHASE FLUID FLOW CONDITIONS PRESENT DURING LEVEE BREACH CLOSURE

4.1 Introduction

The problem of closing an active levee breach is one involving multi-phase fluid flow. Large masses of rock or stabilized soil are dropped into the floodwaters flowing through the breach. These masses are transported along a trajectory that is influenced by the forces generated by gravity, forces generated by contacts with the ground surface or other particles, and forces generated by its motion relative to the surrounding flow of water. In this sense, the breach closure problem may be viewed as a sediment transport problem.

The early stages of a particle's trajectory are likely characterized as "sparse" or "dispersed" multi-phase flows, where the concentration of the solid mass is relatively small. In these early stages, the particle's trajectory is dominated by the influences of gravity and the surrounding fluid. The later stages of a particle's trajectory are more appropriately characterized as "dense" multi-phase flows. In these later stages, the particle's trajectory is dominated by the influences of gravity and the particle's interaction with the ground surface and other particles.

An uncoupled formulation of the discrete element method provides a natural transition from the "sparse" multi-phase flow to the "dense" flow conditions. Within the formulation described here, all forces are permitted to act at any time during the particle's trajectory, and the magnitudes of these forces are evaluated to represent specific conditions in the vicinity of the particle at any instant in time. Through a process of updating these forces over very small increments of time, the particle trajectory can be assembled for a very general set of forces acting on the particle, including the influences of gravity, local boundaries, adjacent particles, and the surrounding fluid.

4.2 The Set of Forces Acting on A Particle In Multi-Phase Flow

The basic framework for an uncoupled formulation of the DEM for multi-phase flow exists in the calculation scheme described in Figure 3.5. However, the scheme shown in

Figure 3.5 does not permit changes in the number of particles within the assembly. The scheme of Figure 3.5 also neglects the interaction between the particle and a surrounding fluid (the fluid existing in the interstitial areas between solid particles). For these reasons, the scheme of Figure 3.5 must be modified to consider the most general class of problems in soil mechanics (Han et al, 2007; Nui et al, 2007; Bui et al, 2008).

To properly simulate a sparse multi-phase flow problem (e.g., the entrainment of solid masses in a floodwater flow to achieve levee breach closure), the basic scheme of the DEM shown in Figure 3.5 must incorporate several additional forces acting on the particle. As a minimum, the set of forces acting to accelerate the particle should include the buoyancy force, the viscous drag force, and the apparent mass acceleration, in addition to those forces described in Figure 3.5. The minimal complete set of forces acting to accelerate a particle within a multiphase flow is illustrated in Figure 4.1. The inclusion of these three additional forces is conceptually straightforward, as it relies upon parameters which are already employed in the basic DEM (e.g., $D_{(i)}$, ρ_S or $m_{(i)}$, and $\underline{v}_{(i)\{t\}}$) and an existing hydrodynamic model of the levee breach (ρ_F, μ, and $\underline{\upsilon}$).

It important to note that particle trajectories generated by the DEM will be described in terms of the set of basis vectors used to define the hydrodynamic model. If the hydrodynamic model used to characterize the fluid velocity field is discretized in all three spatial dimensions, then three velocity components will be computed at a set of gridpoints corresponding to spatial locations defined in three dimensions. While this is generally preferable, a significant computational effort is associated with this model. For this reason, the three-dimensional problem is often reduced to a two-dimensional section view of the problem. In this case, flow velocities are averaged over the spatial dimension corresponding to water depth. The resulting simulation computes two velocity components, one for each "plan view" dimension, at gridpoints defined by the two plan dimensions. Variations in velocity occurring over the height of the element are not considered, though the potential energy associated with the pressure head (measured by the third spatial dimension) is incorporated into the energy balance. This set of assumptions corresponds to the so-called "shallow water equations" of Chapter 3.

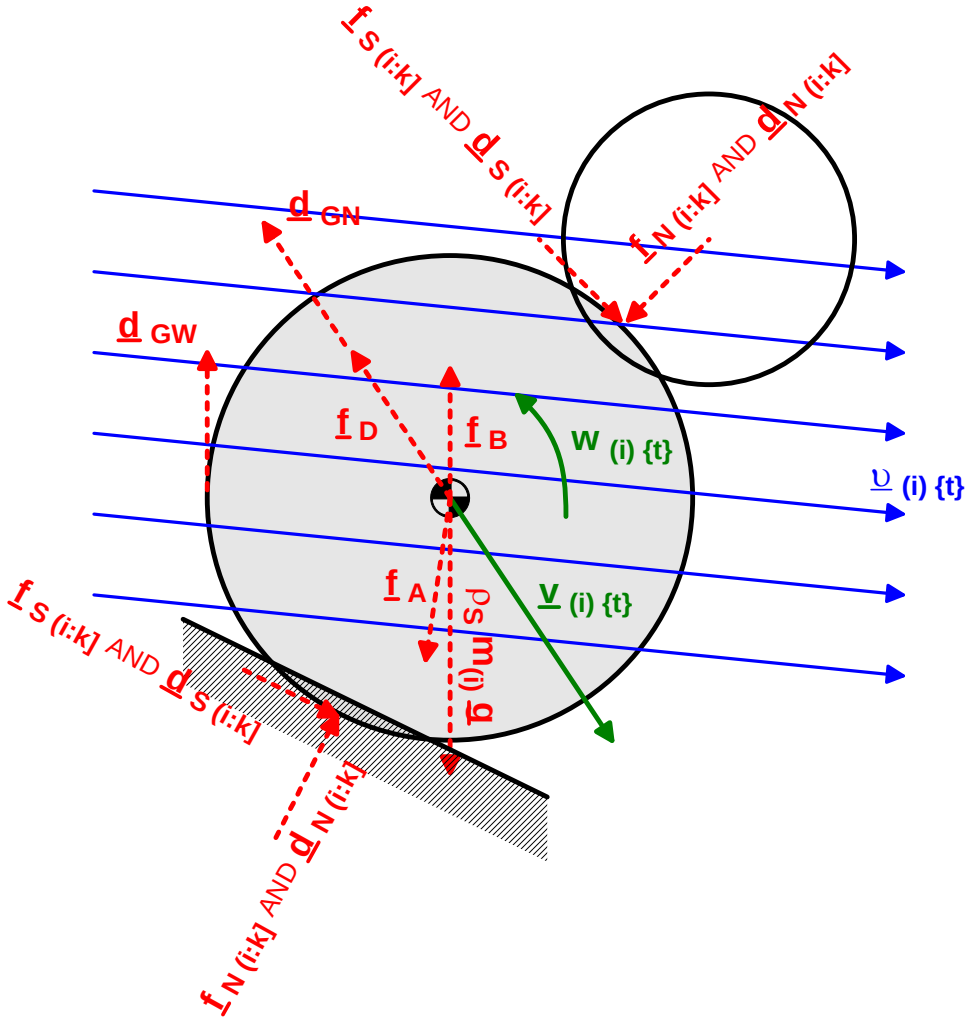

Figure 4.1 Forces Acting to Accelerate Particle (i) in Multi-Phase Flow at Time {t}.

The three-dimensional flow problem may also be reduced by neglecting variations in the fluid flow field occurring in one plan dimension. In this case, the three-dimensional boundary value problem is directly reduced to a two-dimensional problem and the energy balance of equations 3.1 through 3.4 include components along the basis vectors describing elevation and one of the two plan dimensions.

An implicitly enforced mating occurs between the base vector systems used for the hydrodynamic model and the DEM. The fluid velocity is only defined for the base vector system employed in the hydrodynamic model, so that the relative velocity between the particle and the fluid (and thus the velocity of the particle) may only be defined within this same base vector system. For this reason, particle motions within a coupled version of the DEM may only be influenced along base vector directions aligned with those used in the hydrodynamic simulation.

4.3 A Proposed Calculation Algorithm for DEM in Multi-Phase Flow

Because the DEM is directly superimposed on the unhindered fluid velocity field, the hydrodynamic model must be performed first to represent the prevailing conditions in which particles of the DEM will exist. For this reason the DEM is best viewed as a "subroutine" within the hydrodynamic modeling effort, as shown in the proposed calculation algorithm of Figure 4.2. This insertion represents a numerical coupling of the hydrodynamic model for the fluid flow and the DEM model of the particle motions. It is important that this does not imply that behavioral coupling of the particle and fluid motions are being considered. As mentioned in Chapter 3, the particle and fluid flow are "uncoupled" in the sense that the particle's presence is assumed to have no influence on the unhindered fluid flow field.

The "coupling" produced by the insertion of the DEM as a subroutine within the hydrodynamic model is a numerical coupling (previously employed by Kumagai et al, 2006), in which the particle and fluid flow remain behaviorally uncoupled over a single calculation cycle (indicated by the subscript <g>). The subscript <g> thus represents a particular set of steady-state flow conditions which exists over a relatively small increment of time. This small increment (in which a specific hydrodynamic model, identified by <g>, applies) corresponds to the elapsed time from the instant at which a single particle is introduced

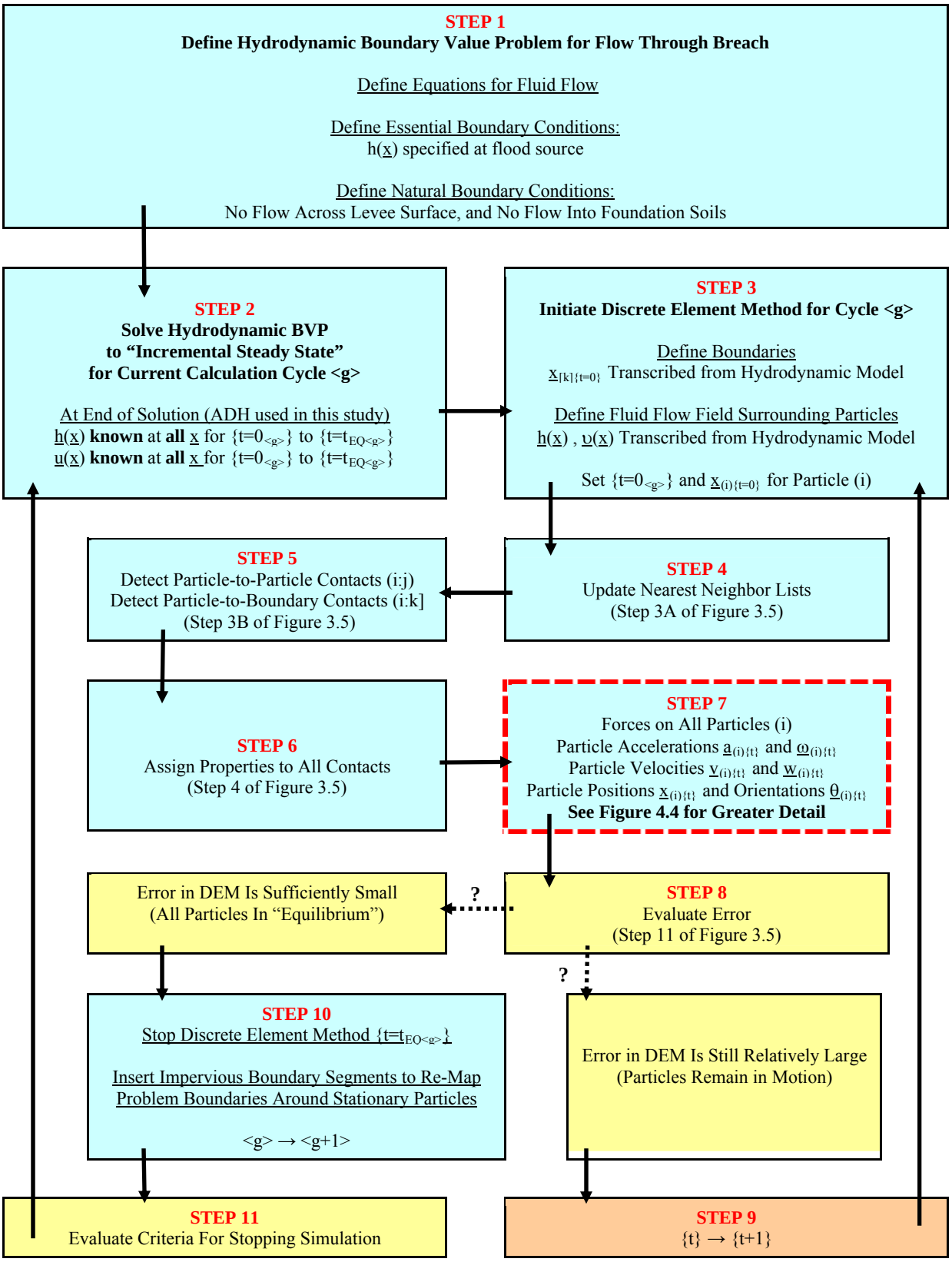

Figure 4.2 Proposed Calculation Algorithm Illustrating Interface Between Hydrodynamic Model of Fluid Flow Field and Discrete Element Model of Particles.

into the assembly and the instant at which that particle achieves equilibrium. This strategy permits an approximation of the behavioral coupling of particle and fluid flows through a complete redefinition of the hydrodynamic model at the end of each particle insertion. As shown in Figure 4.3, at the end of the DEM, the hydrodynamic model is redefined to incorporate all particles in equilibrium as boundaries in the forthcoming model cycle <g+1>.

Assuming the fluid velocity can be appropriately defined at a given position and time (via a particular hydrodynamic model <g>), the forces acting on the particle at time {t} of the DEM may be calculated as shown in Figure 4.3. Figure 4.3 represents that portion of the calculation cycle <g> identified by the dashed red boundary of Figure 4.2. A comparison of Figure 3.5 and Figure 4.3 reveals that all forces considered in the basic DEM calculation scheme are given an identical account within the modified scheme of Figure 4.3.

The additional forces associated with particle-fluid interaction are estimated in the steps immediately following the estimates of contact forces, as shown in Figure 4.3. These additional forces require the development of certain partial derivatives of the fluid flow in the vicinity of each particle, and these quantities are obtained by simple averaging procedures based on the particle size, as depicted in Figure 4.4. "Large particles" are defined as those having a particle diameter greater than twice the largest distance between any two nodes of the hydrodynamic model grid ($D_{(i)}>2\hat{s}_{MAX}$). The diameter of the large particle thus defines the particle's neighborhood ($\varepsilon_{(i)}$) with respect to its interaction with the local flow field as shown in Figure 4.4(a). Any particle having a diameter less than that defining a "large particle" is classified as a "small particle." As illustrated in Figure 4.4(b), the neighborhood of small particles is taken to equal that of the minimum diameter corresponding to a large particle, even though this neighborhood extends outside the actual surface of the particle. This scheme ensures that several nodal grid points (being in number $Y_{(i)}$) of the hydrodynamic simulation at cycle <g> are located within the perimeter defined by the particle neighborhood.

The unhindered fluid velocity acting at the particle location ($\underline{\upsilon}_{(i)\{t\}}$) is estimated as a simple average of unhindered velocity vectors associated with grid points located within the particle's averaging neighborhood. Velocities obtained by this procedure account for the effects of fluid drag in a manner consistent with that used to develop the Basset-Boussinesq-Oseen Equation, though more sophisticated techniques exist (Feng et al, 2007). Once the

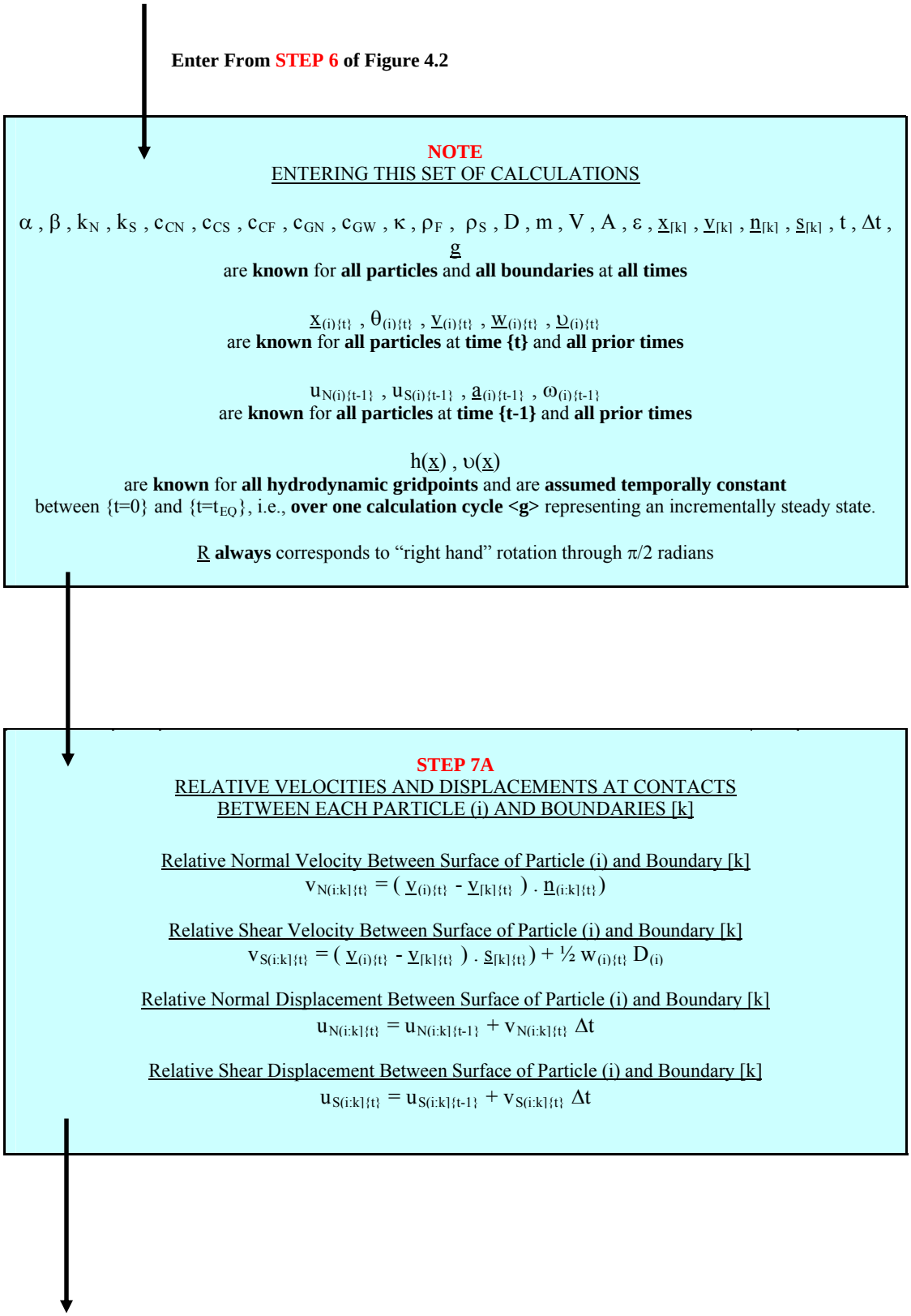

Figure 4.3 Proposed Algorithm for Calculation of Accelerations for Each Particle (i) in Particle Assembly at Time {t}.

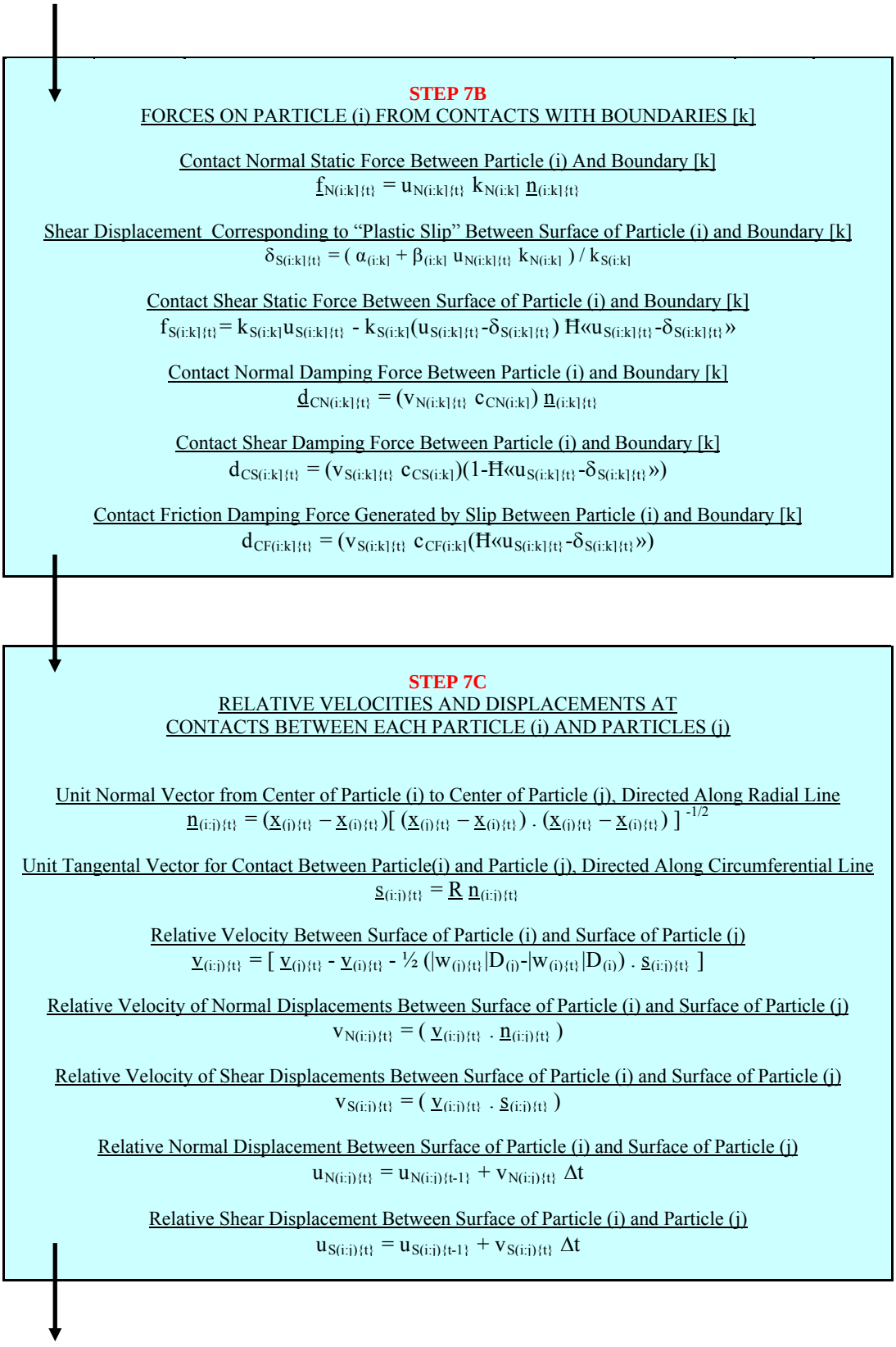

Figure 4.3 (continued) Proposed Algorithm for Calculation of Accelerations for Each Particle (i) in Particle Assembly at Time {t}.

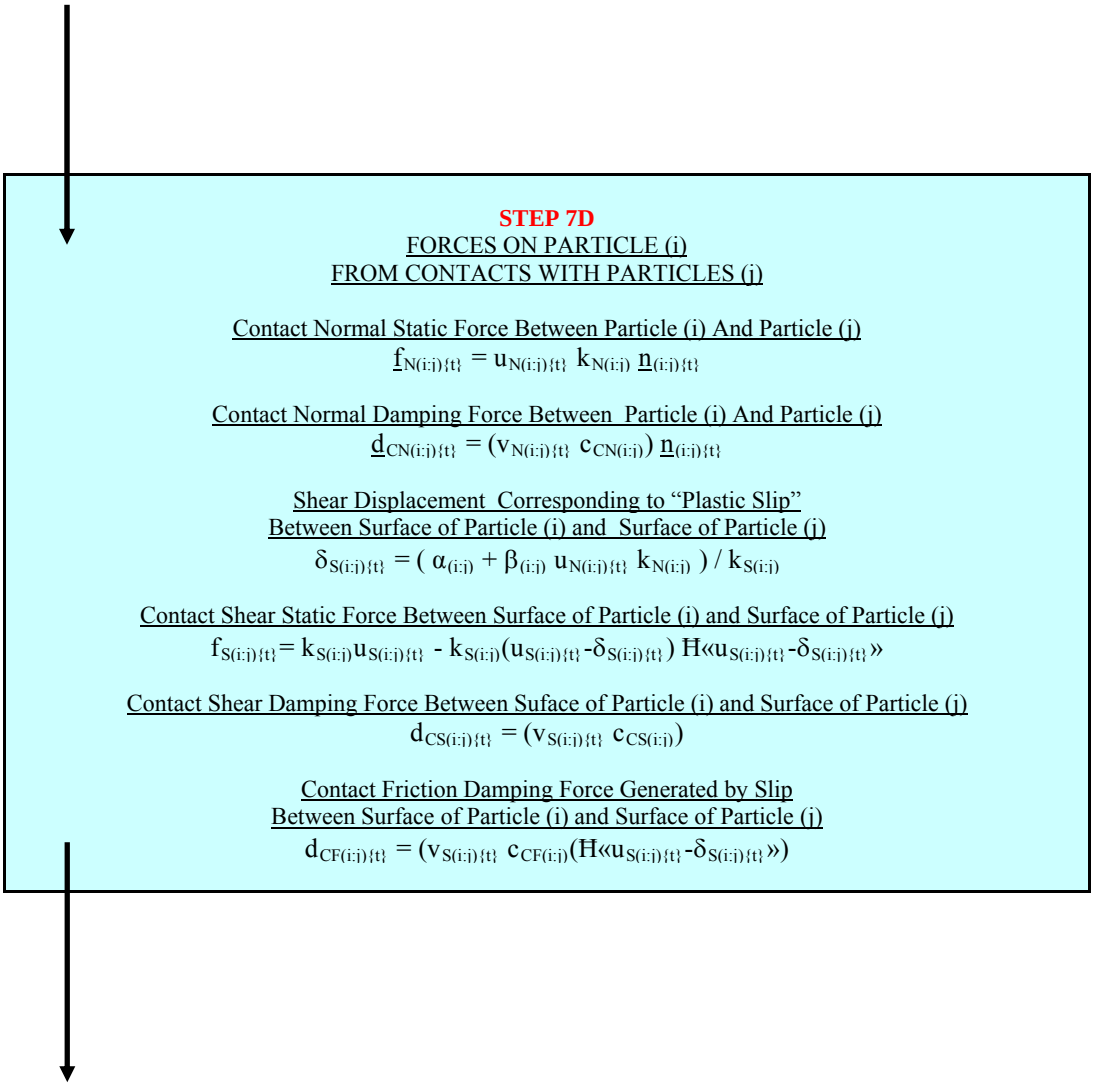

Figure 4.3 (continued) Proposed Algorithm for Calculation of Accelerations for Each Particle (i) in Particle Assembly at Time {t}.

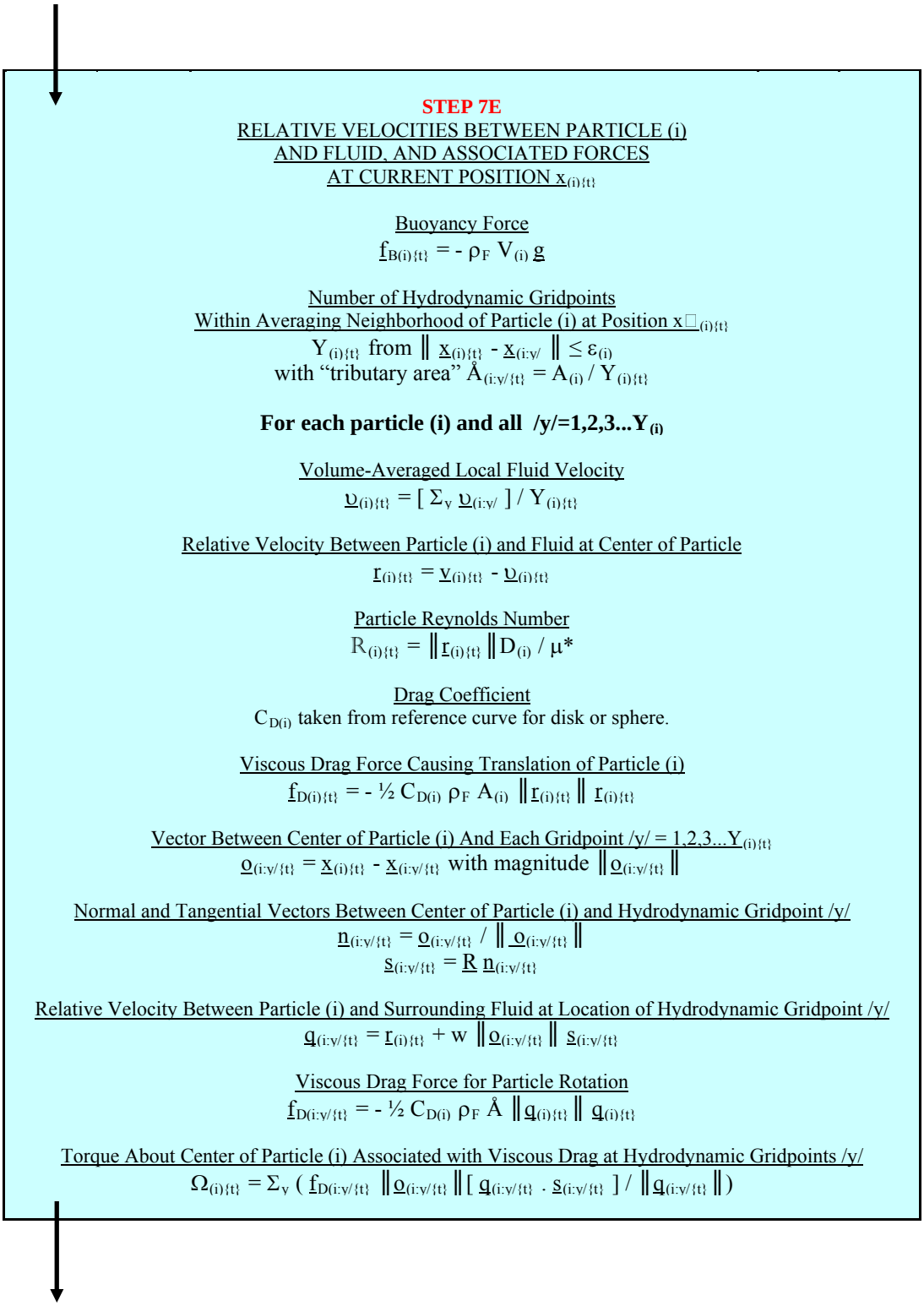

Figure 4.3 (continued) Proposed Algorithm for Calculation of Accelerations for Each Particle (i) in Particle Assembly at Time {t}.

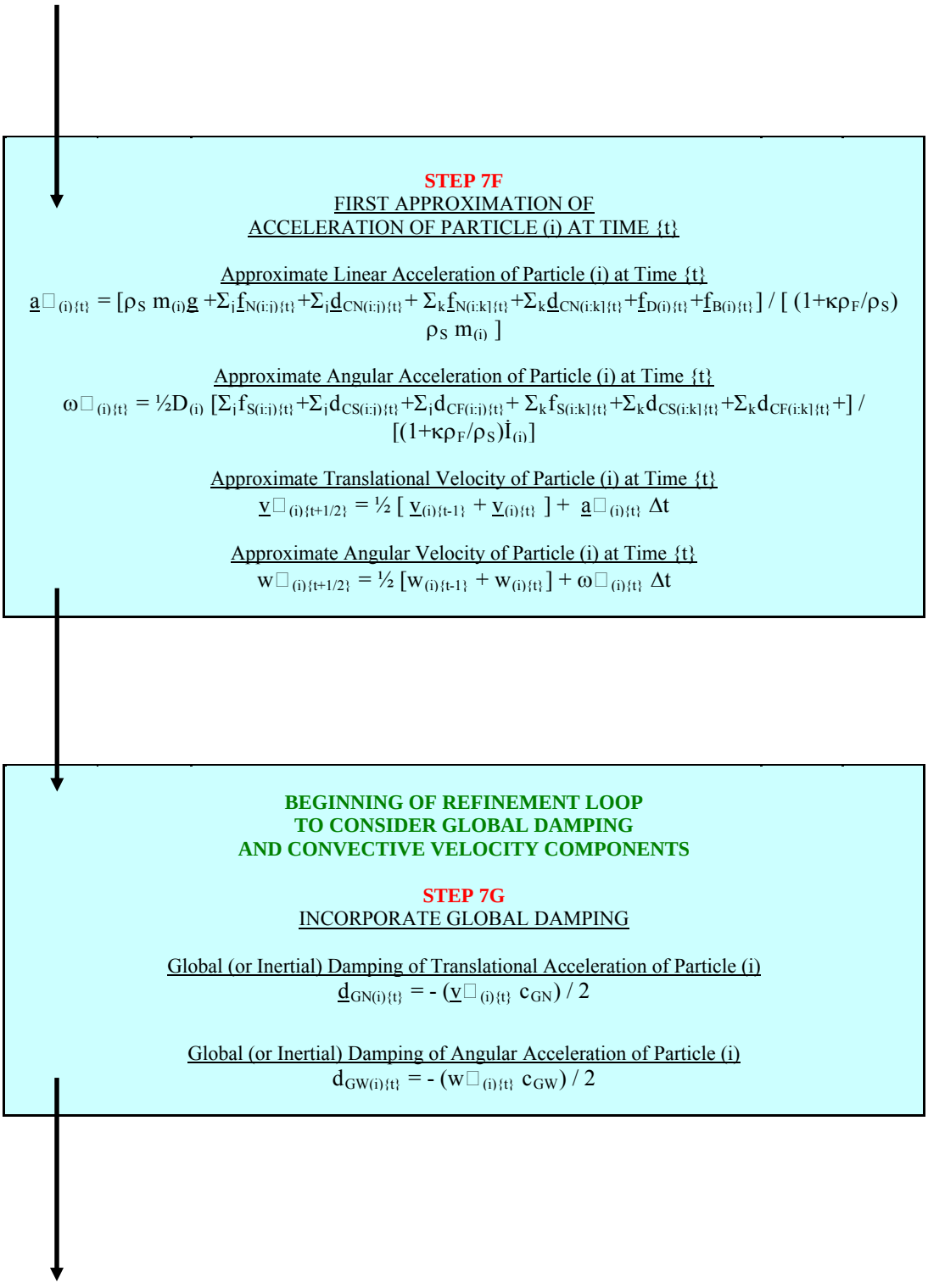

Figure 4.3 (continued) Proposed Algorithm for Calculation of Accelerations for Each Particle (i) in Particle Assembly at Time {t}.

STEP 7H

CALCULATION OF CONVECTIVE COMPONENTS OF VELOCITIES

Predictor of Spatial Positions Over Which Convective Components Will Act in Upcoming Time Step

$$\underline{x}_{(i)\{t+1\}} = \underline{x}_{(i)\{t\}} + \underline{v}_{(i)\{t+1/2\}}\,\Delta t$$

For each particle (i) and all /y/=1,2,3...$Y_{(i)}$

Volume-Averaged Local Fluid Velocity For Particle (i) at Position $\underline{x}_{(i)\{t\}}$

$$\underline{\upsilon}_{(i)\{t\}} = [\,\Sigma_{v}\,\underline{\upsilon}_{(i:v/}\,]\,/\,Y_{(i)\{t\}}$$

NOTE: To increase stability of convergence, this step uses the same set of hydrodynamic gridpoints as those in STEP 5 of this figure.

Relative Velocity Between Particle (i) and Fluid at Center of Particle

$$\underline{r}_{(i)\{t\}} = \underline{v}_{(i)\{t+1/2\}} - \underline{\upsilon}_{(i)\{t\}}$$

Particle Reynolds Number

$$\mathbb{R}_{(i)\{t\}} = \|\underline{r}_{(i)\{t\}}\|\,D_{(i)}\,/\,\mu^{*}$$

Drag Coefficient

$C_{D(i)}$ taken from reference curve for disk or sphere.

Vector Between Center of Particle (i) And Each Gridpoint /y/ = 1,2,3...$Y_{(i)\{t\}}$

$$\underline{o}_{(i:y/\{t\}} = \underline{x}_{(i)\{t\}} - \underline{x}_{(i:y/\{t\}} \text{ with magnitude } \|\underline{o}_{(i:y/\{t\}}\|$$

Normal and Tangential Vectors Between Center of Particle (i) and Hydrodynamic Gridpoint /y/

$$\underline{n}_{(i:y/\{t\}} = \underline{o}_{(i:y/\{t\}} \,/\, \|\underline{o}_{(i:y/\{t\}}\|$$

$$\underline{s}_{(i:y/\{t\}} = \underline{R}\,\underline{n}_{(i:y/\{t\}}$$

Relative Velocity Between Particle (i) and Surrounding Fluid at Location of Hydrodynamic Gridpoint /y/

$$\underline{q}_{(i:y/\{t\}} = \underline{r}_{(i)\{t\}} + w_{(i)\{t+1/2\}}\,\|\underline{o}_{(i:y/\{t\}}\|\,\underline{s}_{(i:y/\{t\}}$$

Viscous Drag Force for Particle Rotation

$$\underline{f}_{D(i:y/\{t\}} = -\,\tfrac{1}{2}\,C_{D(i)}\,\rho_{F}\,\text{Å}\,\|\underline{q}_{(i:y/\{t\}}\|\,\underline{q}_{(i:y/\{t\}}$$

Torque About Center of Particle (i) Associated with Viscous Drag at Gridpoints /y/

$$\Omega_{(i)\{t\}} = \Sigma_{y}\,(\,\underline{f}_{D(i:y/\{t\}}\,\|\underline{o}_{(i:y/\{t\}}\|\,[\,\underline{q}_{(i:y/\{t\}}\,.\,\underline{s}_{(i:y/\{t\}}\,]\,/\,\|\underline{q}_{(i:y/\{t\}}\|\,)$$

Effective Relative Velocity (□) Between Particle (i) And Surrounding Fluid Considering Convective Components of Material Time Derivative

$$\underline{r}^{*}_{(i)\{t\}} = \tfrac{1}{2}\,(\underline{r}_{(i)\{t\}} + \underline{r}_{(i)\{t\}})$$

Apparent Mass Acceleration at Particle (i)

$$\underline{f}_{A(i)\{t\}} = -\,\kappa\,\rho_{F}\,V_{(i)}\,[\,a_{(i)\{t\}} + (\underline{r}_{(i)\{t\}} - \underline{r}_{(i)\{t\}})\,/\,\Delta t\,]$$

Effective Viscous Drag Force Causing Translation of Particle (i) Considering Convective Components of Material Time Derivative

$$\underline{f}^{*}_{D(i)\{t\}} = -\,\tfrac{1}{2}\,C_{D(i)}\,\rho_{F}\,A_{(i)}\,\|\underline{r}^{*}_{(i)\{t\}}\|\,\underline{r}^{*}_{(i)\{t\}}$$

Effective Torque About Center of Particle (i) Associated with Viscous Drag at Gridpoints /y/ Considering Convective Components of Material Time Derivative

$$\Omega^{*}_{(i)\{t\}} = \tfrac{1}{2}\,(\Omega_{(i)\{t\}} + \Omega_{(i)\{t\}})$$

Figure 4.3 (continued) Proposed Algorithm for Calculation of Accelerations for Each Particle (i) in Particle Assembly at Time {t}.

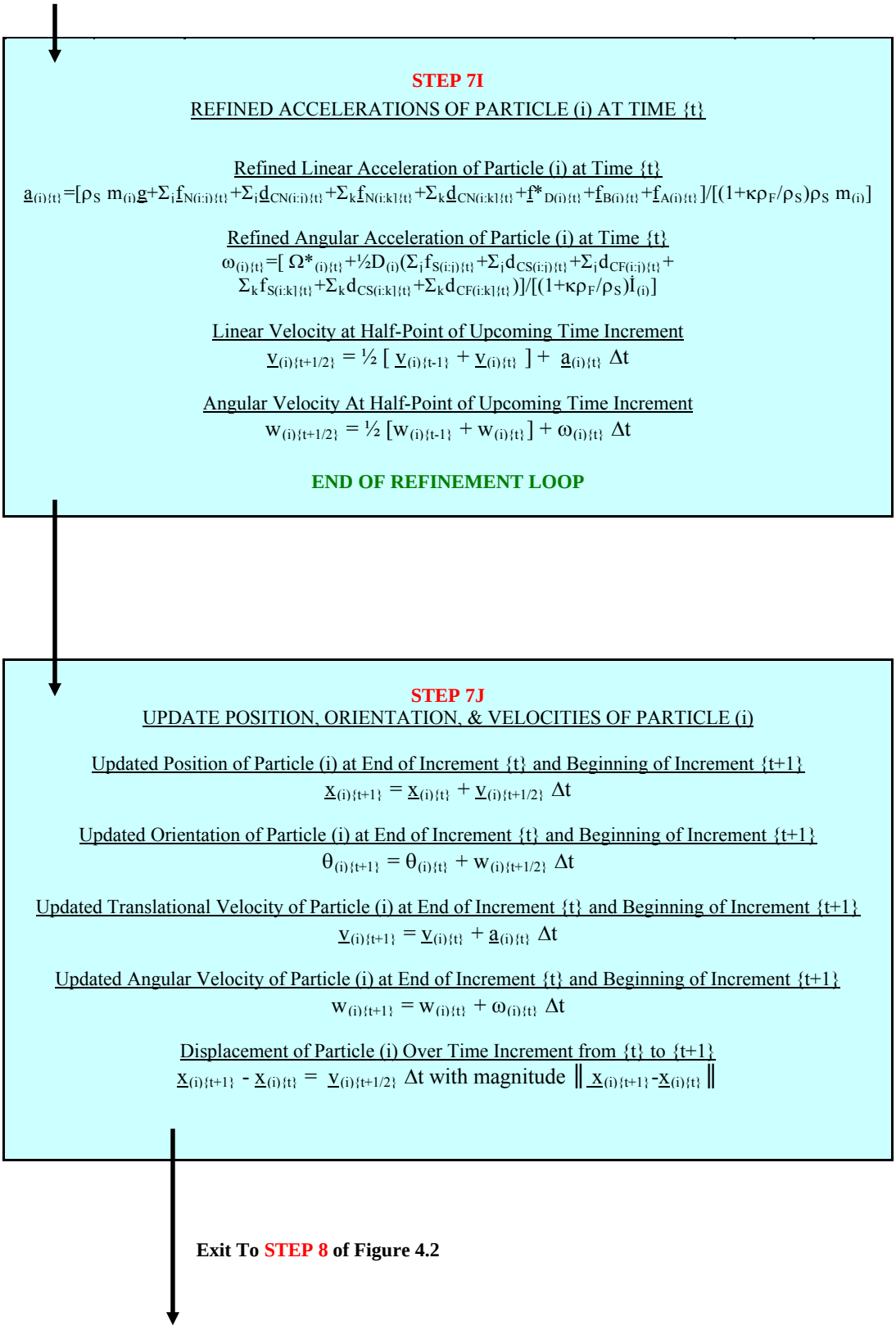

Figure 4.3 (continued) Proposed Algorithm for Calculation of Accelerations for Each Particle (i) in Particle Assembly at Time {t}.

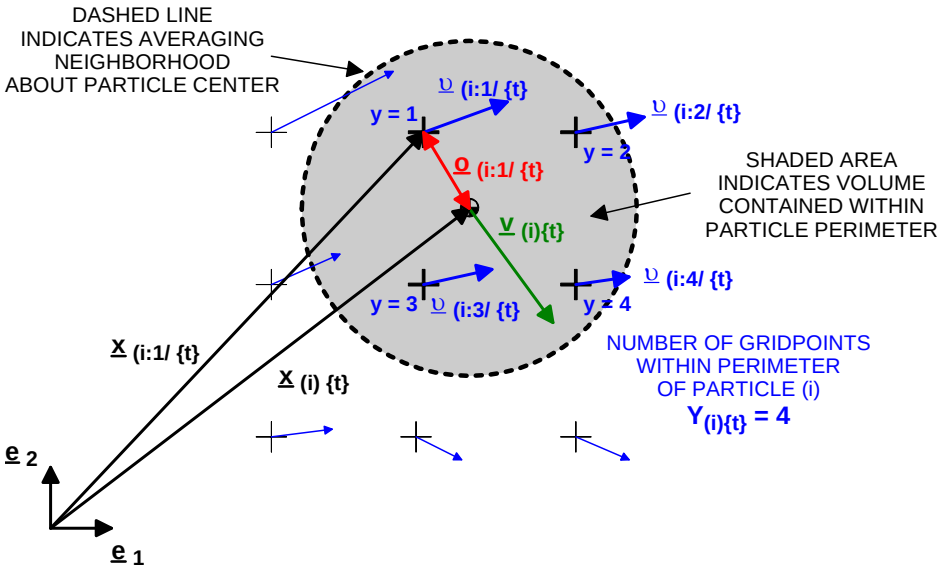

(a)

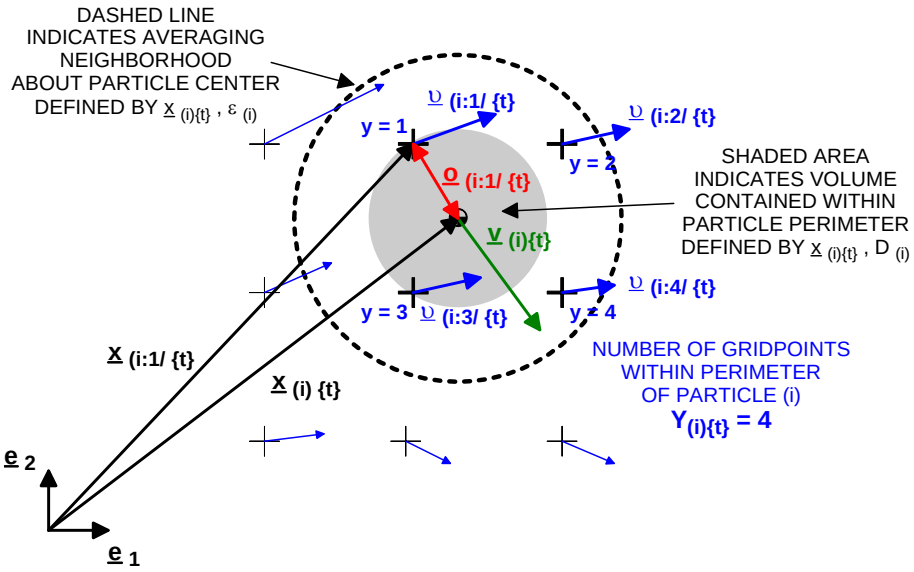

(b)

Figure 4.4 Averaging of Fluid Velocity Field (a) Over Volume of a Large Particle and (b) In Neighborhood of a Small Particle.

volume-averaged fluid velocity is estimated, the relative fluid velocity between the particle and the fluid ($\underline{r}_{(i)\{t\}}$) may be calculated, as shown in Steps 7E and 7H of Figure 4.3.

The vector $\square_{(i)\{t\}}$, representing the volume-averaged fluid velocity within the area bounded by Particle (i), may not be aligned with the particle's center of gravity. In this case, the volume-averaged fluid velocity exerts a torque on the particle, as shown in Figure 4.4(b). The magnitude of this torque is estimated from a summation of moments generated by the various fluid velocity vectors ($\underline{\upsilon}_{(i:y/\{t\}}$ where $y=1,2,3...Y_{(i)}$) within the averaging neighborhood. The moment arm for each of these vectors is first calculated from the difference in the position of each fluid velocity vector and the particle's center of gravity. The tangential component of each of the fluid velocity vectors is then calculated by projection of the velocity vector onto a vector tangential to the radial line passing through the velocity vector's nodal position. Each velocity vector is assumed to act over an equal fraction of the particle's cross-sectional area, regardless of its position in the neighborhood. This assumption is equivalent to weighting the drag force associated with the tangential component of each fluid velocity vector by a factor equal to its squared magnitude divided by the sum of the squared magnitudes for the tangential components of all fluid velocity vectors within the averaging neighborhood. Additional sophistication which may be obtained by assigning tributary areas to each nodal velocity by other means was judged to be unwarranted. The collective error in particle spins may be offset through adjustments to the global damping parameter c_{GS} when the DEM model is calibrated against experimental observations of an actual particle assembly.

The drag force resulting from the tangential component of each fluid velocity vector within the neighborhood is then multiplied by its associated moment arm to provide the magnitude of the particle torque generated by the local fluid flow, according to the equations shown in Step 7H of Figure 4.3. By the "right-hand convention," a positive torque is associated with counterclockwise angular acceleration of the particle, and this assumption is consistent with that used to develop the equations of particle motion employed by the DEM. The resultant torque is then inserted into the equations used to estimate the angular acceleration of the particle.

A similar averaging scheme is required to estimate the apparent mass accelerations of Equation 3.11. The balance of momentum associated with the apparent mass acceleration

requires the material time derivative of the relative velocity between the particle and the surrounding fluid. To consider convective components of this derivative, variations in the particle velocity and fluid velocity must be evaluated over the upcoming time increment. Within Step 7H of the algorithm shown Figure 4.3, these components are estimated from preliminary approximations of the particle's position and orientation ($\underline{x}^{*}_{(i)\{t+1\}}$ and $\theta^{*}_{(i)\{t+1\}}$) at the end of the upcoming time increment. These preliminary approximations of particle position are taken from preliminary approximations of the particle's linear and angular velocities ($\underline{v}^{*}_{(i)\{t+1\}}$ and $\underline{w}^{*}_{(i)\{t+1\}}$) which must be generated for the purpose of applying the global damping forces. Using the preliminary approximations of the particle's position at the next time step, an estimate of the volume-averaged fluid velocity at the new particle location ($\underline{u}^{*}_{(i)\{t+1\}}$) may be obtained by the same procedure described above. In turn, an approximation of the relative fluid velocity ($\underline{r}^{*}_{(i)\{t+1\}}$) may also be preliminarily gained for the upcoming time step. Through these estimates of the particle's upcoming position and the relative fluid velocity at that position, the convective terms are considered in the material time derivative of the relative fluid velocity shown in Figure 4.3.

The complete set of forces shown in Figure 4.1 may then be estimated for each particle. As with the basic DEM scheme, the summation of these forces is divided by the particle mass to provide an estimate of the particle's acceleration through the upcoming time increment. However, Step 7I of the algorithm in Figure 4.4 shows that the particle's acceleration is influenced by its own mass and the apparent mass of the fluid which must be accelerated from the particle's volume. Torques applied to each particle are also summed to provide an estimate of the particle's angular acceleration. The apparent mass is also incorporated into the mass moment of inertia used to estimate the particle's angular acceleration. Once the linear and angular accelerations have been estimated, the algorithm proceeds similarly to that of the basic DEM by updating particle velocities and angular velocities. Finally, updated estimates of particle positions and orientations are generated.

The particle accelerations estimated in the final steps of Figure 4.3 are generated by the set of forces presented in Figure 4.1 at every time increment during which a "new" particle is in motion toward a state of equilibrium. The duration of the DEM simulation within a given model cycle $t_{F<g>}$ is defined by the time required to achieve equilibrium of the assembly under the influence of the newly introduced particle. However, in the manner

described for the basic DEM calculation scheme, the equations of motion are applied to all particles (the "new" particle and all particles existing at the beginning of the DEM for model cycle <g>) at all times {t} between the instant the particle is introduced {t=0} and the instant of equilibrium $\{t=t_{F<g>}\}$.

As shown in Figure 4.2, the DEM model is stopped when the assembly has achieved equilibrium under the influence of the new particle (a sort of "temporary equilibrium"), and the positions of all particles in the assembly are fixed. The positions of all particles corresponding to the temporary equilibrium of model cycle <g> are used to define the particle positions at the initiation of model cycle <g+1>, when another particle is introduced into the assembly. At the end of model cycle <g>, the particle positions are also used to remap the boundaries of the hydrodynamic model, as shown in Figure 4.5. With this remapping, the algorithm shown in Figure 4.2 completes an entire model cycle <g>. The algorithm returns to the beginning of a model cycle, unless the user indicates the simulation is complete. The simulation may run to the point at which the entire domain of the problem is filled with particles, though the user will typically want to stop the simulation at an earlier time.

The solution for the flow field in cycle <g+1> may differ from that used in the prior model cycle <g>. In this sense, a certain degree of coupling is introduced between the fluid flow and the particle motions, as the field of unhindered flow velocities is altered by the presence of an additional particle. However, the field of unhindered flow velocities during a particular calculation cycle is employed over the entire model cycle without modification, regardless of any changes to the positions and motions of particles in the DEM during that cycle. It is only at the end of the model cycle that the field of unhindered flow velocities is modified, so that the coupling between fluid and particle motions is weak.

4.4 Potential Criteria for Ending the Breach Closure Simulation

The proposed algorithm illustrated in Figures 4.2 and 4.3 may be continued until the entire domain is occupied by particles. Obviously, this result is a computationally expensive one which has no value in determining the efficacy of an actual breach closure.

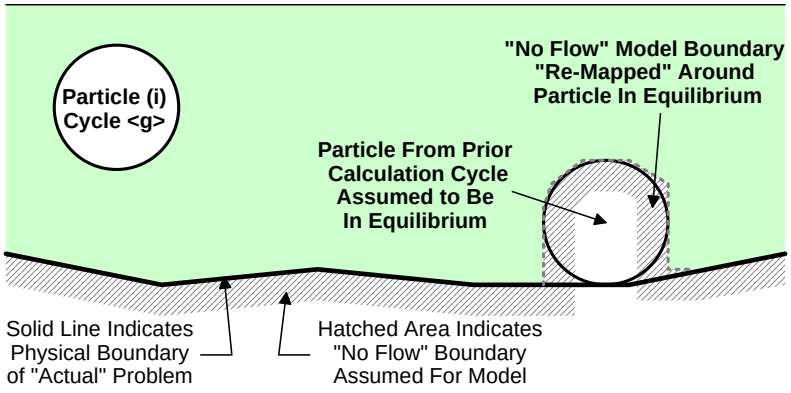

(a)

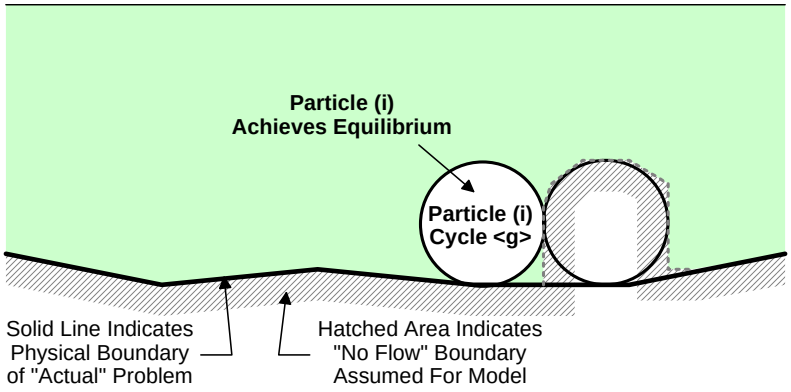

(b)

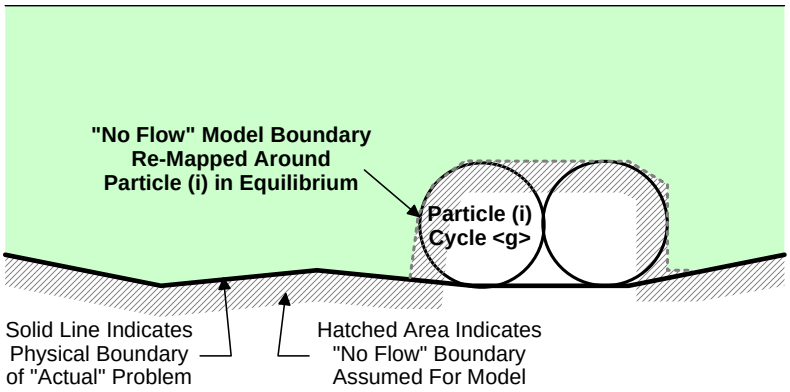

(c)

Figure 4.5 Remapping of Boundary Conditions for Hydrodynamic Model: (a) At Beginning of Discrete Element Simulation in Calculation Cycle <g>, (b) At End of Discrete Element Simulation in Calculation Cycle <g>, and (c) After Re-Mapping for Beginning of Calculation Cycle <g+1>.

For this reason, the user must specify a criterion (or a combination of criteria) which signifies that the simulation has successfully achieved a breach closure. Development of a set of appropriate criteria for ending the simulation is a substantive effort, requiring calibration of the simulation technique against physical observations. While the development of these criteria is beyond the scope of the current study, six potential criteria are subsequently proposed and discussed. However, a combination of these various criteria seems most appropriate. All of the potential end criteria proposed herein are experimental in nature.

First, the user may elect to terminate the simulation when the particle assembly occupies a certain specified volume (or provides a certain minimal cross-sectional area transverse to the breach discharge) at all points in the domain at the end of the model cycle. This criterion is equivalent to specifying that the reconstructed levee (created by breach closure) forms a pre-approved shape which has been judged to provide an adequate level of safety. While the DEM assembly may not conform to the specified shape, this end criterion is relatively easy to enforce and its physical meaning is easily interpreted.

A second criterion for ending the simulation may be developed by requiring the maximum fluid velocity at any point in the problem domain be less than a specified velocity. This criterion builds upon the widely-accepted practice of limiting overland flow velocities to those which will not remove soil particles from a defined boundary and subsequently transport the particles away from that boundary. These flow velocities may be as low as 0.2 m/s (0.7 ft/s) to limit the scour and transport of loose fine sands and silts. Higher limitations on the maximum fluid velocity may be permissible, though, as unblended or unstabilized fine sands and silts are among the least preferred soils for achieving breach closure.

A third criterion arises from specifying a maximum value for the product of the maximum flow velocity and the amount of "open area" existing over subdomains. This sort of specification may be interpreted as a limitation on the volume of flow through the breach. While such a specification may be very useful, its use within a DEM will provide only a corollary measure of reductions in breach discharge. DEM simulations, especially two dimensional simulations, produce overlaps at particle contacts which may appear to block the flow of water. In reality, fluid may flow freely along the tortuous path connecting openings between particles, even when the particles are forced into very dense assemblies. In addition,

a set of supplementary criteria would be necessary to define the appropriate sizes of subdomains used to calculate the discharge.

A fourth criterion for ending the simulation may correspond to a restriction on the maximum energy gradient observed between any two nodal points in the hydrodynamic simulation. The energy represented by the total head is easily calculated from the ground surface elevation, water depth, and flow velocities at each node in the domain. A limitation on the spatial gradient of this energy is thus a measure of the energy being dissipated by flow through the breach closure. Energy gradient criteria of this sort are often used to prevent piping in embankment dams (though there is strong disagreement regarding the seepage gradients at which piping is initiated). These criteria are only valid for reducing the likelihood of piping within continuous soil masses. By its nature, the DEM produces discontinuous assemblies of particles which seem to preclude the direct application of piping criteria, especially for assemblies of large particles. Furthermore, very slight energy gradients (well below a specified threshold) may exist within very large fluid flows (e.g., the slight energy gradients of river systems), so that this restriction loses its meaning when applied to a partially closed breach.

A fifth measure of closure stability (within the context of DEM simulations described here) is provided by investigating the maximum displacement observed among all particles in the assembly after remapping of the hydrodynamic problem boundaries. At the end of a model cycle <g>, the positions of all particles are known and these positions are used to remap the boundaries employed in a subsequent hydrodynamic model (representing conditions over model cycle <g+1>). Prior to the introduction of an additional particle in Cycle <g+1>, a complete solution of the existing DEM assembly (prior to introduction of the "new" particle in Cycle <g+1> could be recomputed from superposition of the DEM solution at Cycle <g> onto the revised flow conditions of Cycle <g+1>. This solution would thus provide displacements of all particles in the assembly which are solely attributable to changes in the fluid flow field. By limiting the displacements of every particle in the assembly to a specified maximum value, the user effectively imposes a stability criterion upon the assembly.

A sixth criterion for ending the simulation may be developed from a restriction on the greatest change in the maximum fluid velocity observed anywhere in the domain between

any two successive model cycles. This restriction may be interpreted as a measure of the reduction in breach discharge achieved by the addition of one particle into the assembly (i.e., by the addition of one additional mass into the breach closure). As such, this criterion is a better measure of the efficiency of the breach closure process rather than the safety or effectiveness of the breach closure.

CHAPTER 5

COMPARISON OF PROPOSED ALGORITHM WITH EXPERIMENTAL OBSERVATIONS

5.1 General Objectives

The algorithms described in Chapter 4 provide one scheme for modeling multiphase fluid dynamics problems. These algorithms were developed from equations describing sparse multiphase flows to represent sequential insertions of large particles into a transient hydraulic flow. Under the objectives of the SERRI program, this case of multiphase flow may be made specific by considering the release of a solid mass (i.e., the "particle" of the multiphase flow problem) into the water flowing through a levee breach (i.e., the "fluid flow field" of the multiphase flow problem). The solid mass may represent a mass of stabilized soil, a geosynthetic bag filled with stone, or a single stone or boulder. The distribution of fluid velocities and depths in the vicinity of the breach may be approximated from conventional hydrodynamic simulations employing easily defined boundary conditions for water levels (on both the flood side of the levee and the protected side) and a reasonably defined geometry of the levee breach.

The algorithms presented herein include a number of specific assumptions which have been incorporated to permit reasonable simulations of the physical problem within the constraints of widely available computing capacity. The hydrodynamic simulations presented in Chapter 4 were completed to "steady state" by a non-parallel, non-distributed, Intel Pentium-class chipset and architecture within 24 hours of model definition.

5.2 Descriptions of Physical Experiment and Numerical Simulation

The algorithm presented in Chapter 4 was employed to simulate a set of simple physical experiments involving the dropping of heavily weighted spherical balls into a viscous fluid under quiescent conditions. This set of conditions does not require the generation of a hydrodynamic model of the boundary value problem, and consideration of this simplified problem does not provide validation of the hydrodynamic modeling component of the algorithm. However, the form of the algorithms presented in Chapter 4 assumes that any hydrodynamic model used to represent the unhindered velocity field has

been independently validated. These algorithms thus permit the use of any hydrodynamic modeling software capable of defining the "free surface" of the water and the distribution of fluid velocities within the domain bounded by the free surface and user-defined flow boundaries. A number of commercially-available and research software codes exist for such a problem and may be independently validated (Ratcliffe, 1999).

As the hydrodynamic model is assumed to be completely developed at every calculation cycle <g>, it may exist independent of the discrete element portion of the model used to simulate the particle trajectory. The coupling of the hydrodynamic model and the solid particle trajectory is achieved by casting the output from the hydrodynamic model into a set of spatial gridpoints for which the distance to the free surface and fluid velocity components are known. This coupling may be no more sophisticated than the generation of a text file including these elements, as was used in the current study. These results are then fed into the portion of the modeling algorithm associated with tracking particle trajectory (e.g., Figure 4.3). The simple problem considered further in this chapter thus represents a complete set of hydrodynamic gridpoints for which the unhindered fluid velocities ($\upsilon_{(i)\{t\}}$) are set to zero for all positions ($\underline{x}$) and all times {t}. These unhindered fluid velocities may be viewed as the result of a single hydrodynamic model cycle <g> for which no changes are necessary to represent the entire duration of the simulation.

The flow field in this hydrostatic case provides an optimal data set for calibrating the calculations associated with particle forces and trajectory within a known flow field. Because the particle model represents a significant uncertainty in the proposed algorithm (aside from additional uncertainty which may be associated with the veracity of the hydraulic model), simulation of this experiment represents the highest level of fidelity which may be expected from the particle-tracking method within a coupling scheme of the sort described in this report. The experiment further provides a valuable assessment of the algorithm at its current state of development, considering that the initial emphasis of the research program was directed toward algorithm components for particle motion.

The physical experiments involved the release of spherical steel balls (ρ_S = 7.8 g/cm^3) into a square-shaped tube which is filled with water (ρ_F = 1.0). The experimental setup is illustrated in Figure 5.1 (Lyotard et al 2007). For each experiment, a single ball of known diameter was submerged and suspended at the top of the water column by use of an

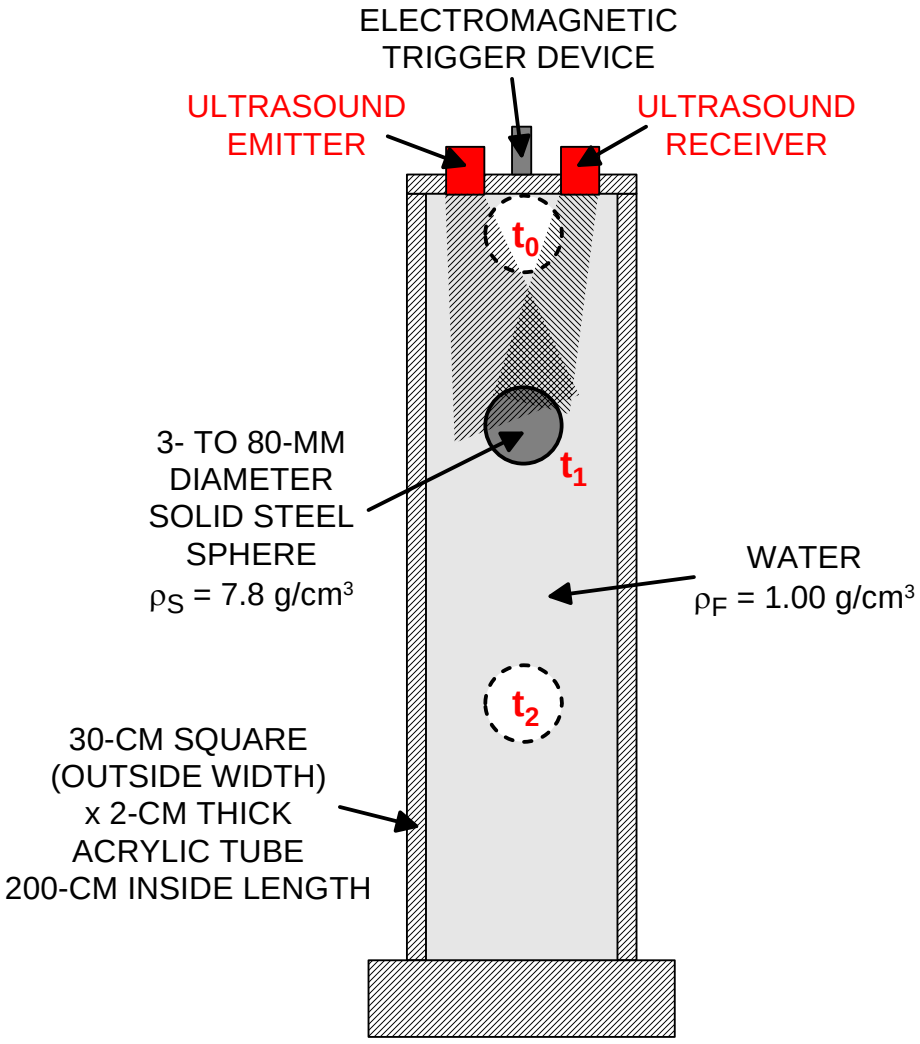

Figure 5.1 Experimental Arrangment for Tracking Spheres During Free-Fall Through Water (after Lyotard et al, 2007).

electromagnet. The ball was then released by a timed short-circuit of the electromagnetic contact, and observations of particle position were initiated within 2 ms after release of the ball. Observations of particle position continued at a frequency of 2.8 MHz during the freefall of the ball through the water column. Filtering of the resulting signal reportedly resulted in estimation of the fall velocity to an accuracy of 1 mm/s during the experiments. The authors of the study did not report the sampling frequency used to filter the raw data. This experiment was repeated for eight ball diameters varying from 3 mm to 80 mm. While several of these experiments may have involved interactions between the turbulent eddies and the walls of the cylinder, the authors report reducing the data set to include only those experiments in which minimal disturbance was observed. The reported results generally confirm prior experiments involving a similar test arrangement (Watanabe et al, 1998).

The current research attempted to reproduce this set of physical experiments by computational simulation. For these experiments, global damping of particle motions was set to zero, so that particle motions were solely affected by gravity and drag forces. While the particular details of the data-smoothing procedures were not known, the data filtering and averaging process was given account by increasing the magnitude of the simulation time step to a value at least one order of magnitude higher than the inverse of the data acquisition frequency. Thus, assuming the data was filtered and averaged to reduce its representative frequency, the simulated trajectories could then be compared directly to the observed trajectories at the same instant in time. Data filtration and averaging were assumed to be performed over a bandwidth of approximately 30 data points, so that the time increment for calculation was set at 1.0×10^{-5}. The fluid viscosity and particle density were matched with quantities reported for the physical experiment. Drag coefficients were calculated at each time increment using the equations for smooth spheres presented previously in Chapter 4.

5.3 Comparison of Results For Quiescent Settling

The results of the experimental data and computational simulation are superposed in Figure 5.2, where the instantaneous velocity of the ball is plotted as a function of elapsed time for ball diameters of 3 mm, 10 mm, and 80 mm. In the physical experiments, the smaller particles achieved terminal velocity within the 2-m length of the water column, as evidenced in Figure 5.2 by the flattening of the velocity records at large times. The

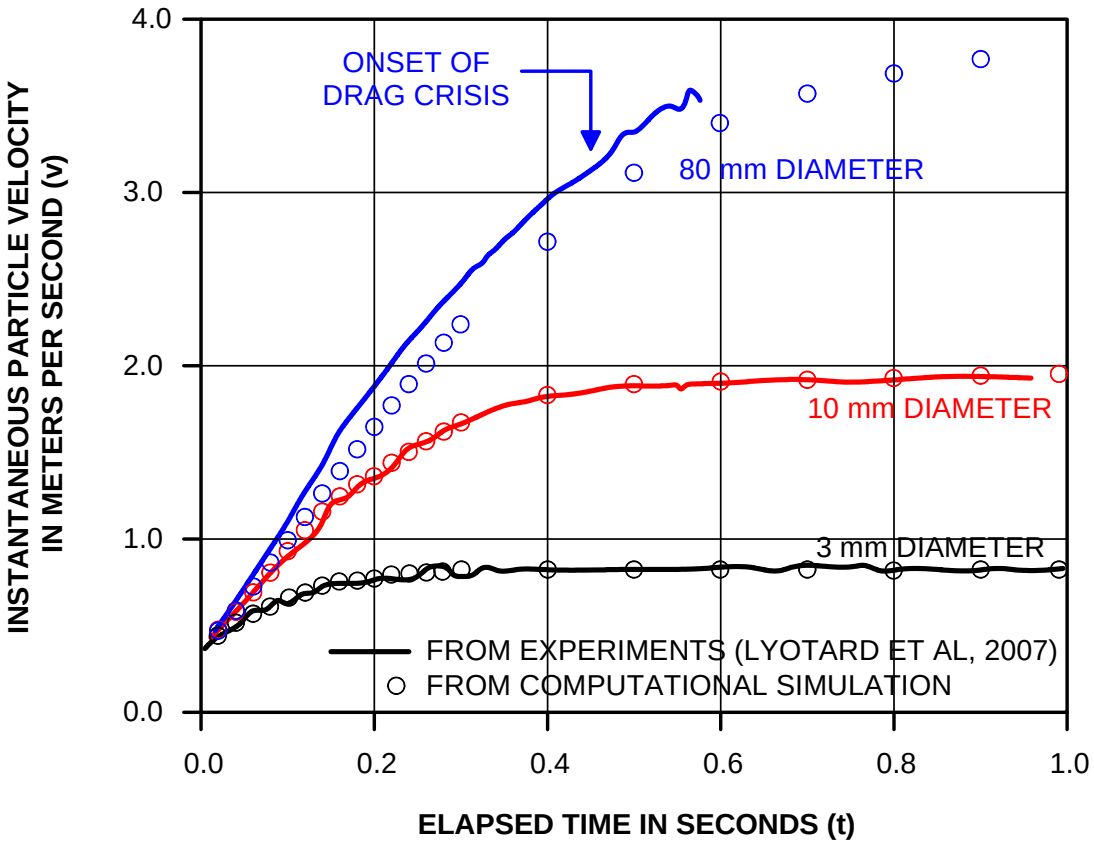

Figure 5.2 Comparison of Simulated and Experimentally-Observed Motions of Particles in Free-Fall Through Water.

computational simulation provides excellent replication of the physical experiments for these smaller particle diameters.

Larger particles, reported by the authors of the experimental study as those larger than 60 mm, typically did not achieve terminal velocity. Furthermore, the researchers reported observation of the drag crisis in these larger particles, as evidenced by slight increases in particle acceleration and corresponding increases in the particle velocity. This trend is barely noticeable in the velocity record for the 80-mm diameter particle at approximately t=0.45 seconds, where the slope of the velocity record steepens slightly near the end of the record. The computational simulation provides a reasonable replication of the physical experiments for these larger particle diameters, though an error exists at larger particle velocities, and the magnitude of this error appears to increase monotonically throughout the simulation.

Differences between the computational simulation may be attributable to any of several sources. Because the algorithm involves a forward approximation for the particle acceleration (though it is one generated to create a central difference with respect to particle velocity), the accuracy of the computational simulation is a function of the magnitude of the time step used to calculate the incremental particle accelerations. The trajectory simulations were performed for magnitudes of the time step corresponding to 0.1, 1.0, and 3.0 MHz ($\Delta t = 1.0 \times 10^{-5}$ seconds, 1.0×10^{-6} seconds, and 3.0×10^{-6} seconds, respectively). The resulting estimates of particle velocities were seen to vary less than two percent for those portions of the velocity record greater than 0.1 second over the range of particle diameters considered.

Errors associated with the onset of the drag crisis may be more significant. These errors were precisely the motivation for the experimental work, and the authors of the experimental study observed very large increases in particle velocities for “roughened” particles. As described in Chapter 4, the drag crisis is initiated by the development of turbulence in the boundary layer between the particle and the fluid. This turbulence is initiated at lower Reynolds numbers for “rough” particles. The result is that the drag force is decreased at lower Reynolds numbers for “rough” particles than for “smooth” particles. This error may be insignificant for very long time records, as the drag force eventually becomes essentially constant with Reynolds number. However, for the relatively short durations associated with the experimental work reproduced here, the effect is of greater importance.

These errors may be addressed within the discrete element method by any of several means. The particle motion during freefall is influenced within the simulation by both the drag coefficient and the global damping coefficient. To enforce a compatibility between the experimental data and the simulation, the modeler may alter either or both of these parameters. Use of an appropriate relationship between drag force and Reynolds number is clearly preferred, as this provides a more rationally-based adjustment to the particle motion. However, the author is not aware of specific data to characterize this relationship for large, roughened particles at high Reynolds numbers.

In any case, differences between the experimentally-observed and simulated particle trajectories act to underscore an important consideration in simulations involving computational coupling of fluid flows within the discrete element method. Specifically, modelers must calibrate the results of these numerical simulations against available physical observations of particle trajectories. In the case of breach simulation, the technique may be calibrated against physical observations from scale models (e.g., Sattar et al, 2008), but certain errors should be anticipated to remain as a result of calibration of a computational model to observations obtained from a scaled physical model. Because large-scale physical models of the breach closure problem do not exist, applications of the computational techniques presented herein are limited to providing qualitative evaluations of breach closure techniques. It is important to note that this limitation is not unique to the techniques presented herein, and any computational simulation technique will require calibration and validation via comparison with physical observations. Despite the need for calibration and validation, computational simulations continue to function as a valuable and cost-effective tool for evaluating the relative merits or behavioral differences existing within a large set of potential scenarios.

With proper calibration against physical observations, the coupling of the discrete element method and hydrodynamic models similarly offers a means to evaluate problems of breach closure involving varying length scales for both the breach size and the masses of particles used to close the breach. With appropriate calibration to large particle sizes and high velocity fluid flows at a length scale near that of existing levee breaches, modelers may use the technique to qualitatively evaluate the variation of breach closure time with respect to breach length. Another use of the technique may exist in evaluating breach closure times

associated with different particle sizes, as these sizes may be influenced by the availability of materials or the limitations of available construction equipment.

5.4 Extensions of Existing Algorithm

The proposed algorithm produces results in reasonable agreement with limited experimental data. However, several difficulties have been identified in scaling the algorithm to large physical systems of the sort associated with levee breach closure. These limitations of the current state of model development may be characterized as one of two types-- those associated with incomplete development of the model, and those associated with fundamental inadequacies of the model equations to represent physical reality.

The first set of these limitations is only significant when viewed in terms of the resources required to remove the limitations. At the present state of model development, the program code omits contact detection algorithms which would permit the simultaneous entrainment of multiple particles. The current state of the model further incorporates the simplest of interpolation routines for fluid velocity fields in the vicinity of a given particle. While efforts to refine these components of the model are substantive, they can be achieved leveraging existing techniques described in the technical literature.

Larger questions are posed by the uncertainty associated with the model's fundamental fidelity to physical behaviors. The equations used herein to approximate the fluid flow field and particle motions were taken from the well-known equations for multiphase flow. By necessity, these equations contain model parameters to describe the properties of the fluids, the entrained solids, and the problem boundaries. Additional model parameters are associated with the decomposition of the equations from their continuous analytic forms into an approximate set of equations which are solved at discrete locations and times. All of the associated model parameters act corporately to scale the solutions of the equations of flow in a way that enforces a match with observed behaviors inside the domain.

However, a void exists in experimental data regarding the closure of levee breaches via the insertion of large particles into highly turbulent, transient, three-dimensional flow fields of the sort associated with breach discharges. Such data constitutes the known behavior against which any computational simulation must be compared. With the limited

data available to serve as benchmarks, the relative merits of any computational simulation (e.g., computational accuracy, fidelity of assumptions, simplicity or complexity) can not be properly assessed. Furthermore, the appropriate set of model parameters (i.e., those which will scale the model solution to appropriately mimic physical reality) will remain unknown.

This weakness in the experimental data thus places severe limits upon evaluations of the adequacy and performance of any one model. It is unlikely that any members of the set of model parameters will be linearly related to the solution variables (i.e., positions or displacements). Considering the large number of model parameters and the similarly large number of physical phenomena being represented by these parameters, it is likely that one or more combinations of model parameters may produce equally good (or bad) solutions. The most appropriate combination of model parameters (for the present model and any other computational simulation technique) is unclear without large scale physical experiments which may be used for calibration. Given the possibility for non-uniqueness between model parameters and the solution set, it is also possible that large scale physical experiments may fully reveal the appropriate set of model parameters to be incorporated. In this case, the simplest models which faithfully reproduce experimental observations are the most justifiable models.

Given the lack of experimental data, computational models may be evaluated in the relatively simple conditions for which observations are available, and such a demonstration has been performed herein. The simulations of simple conditions appear to indicate the algorithms proposed in this report capture important physical behaviors. Furthermore, the suite of model parameters is sufficiently rich to permit calibration of the model equations to physical data over a wide range of length scales. Despite such promise, the algorithms presented herein have not been calibrated against data suitably representative of the levee breach closure problem, and appropriate model parameters for such a case have yet to be identified.

CHAPTER 6

CONCLUSIONS AND RECOMMENDATIONS

6.1 Summary of Research Program

This report has examined the common conditions in which levee breaches may exist and the various means by which the typical size of a levee breach may be estimated. These assessments are important to emergency responders, as they may be used to crudely define the initial conditions (e.g., breach size, breach discharge, fluid velocities) acting at the initiation of breach closure. When coupled with additional information regarding the polder size, polder topography, and flood period, these initial assessments have been demonstrated to provide additional critical information regarding the time available to achieve breach closure.

A set of computational algorithms have been developed to simulate the motion of solid particles entrained within a fluid flow. These algorithms were developed for specific application to the problem of achieving levee breach closure via entraining large solid masses into the breach discharge. However, the algorithms are general in nature and may be useful in applications beyond the levee breach closure problem.

The algorithms presented herein are a version of the MCDS technique for partially coupled analysis of the strongly-coupled interactions between fluid flows and particles entrained in these flows. The computational algorithms are centered upon modeling the trajectory of the solid masses (e.g., the “particles”) under the influence of interactions with a flowing fluid, local boundaries, and other particles. The motions of the fluid in the vicinity of the particle are incorporated from the results of a hydrodynamic simulation performed to evaluate the unhindered fluid velocity field prior to insertion of a single particle. The resulting fluid velocity field is maintained constant over a small increment of time corresponding to that required for a single particle to be entrained and subsequently come to rest. An entire simulation of breach closure may be created in this partially coupled manner through successive cycles alternating between the hydrodynamic model and the particle trajectory model.

Several simplifying assumptions were employed to demonstrate the proposed algorithms within the abbreviated scope of the project. The developed algorithms were demonstrated to qualitatively reproduce the behavior of spherical-shaped masses traveling through a fluid for the simplest case of particle drops in free-fall through a column of viscous and incompressible fluid. Because of the general nature of the concepts presented herein, limitations placed upon the model via its partial development may be removed with relative ease, by including more sophisticated algorithms for particle contact detection, particle geometries and rotation. These additions may leverage existing techniques documented in the technical literature.

Despite the simplicity of the demonstrations presented herein, sufficient model complexity exists to closely replicate observed multiphase flows. The most significant obstacles to further development of the model described herein (and, in truth, any model developed to simulate breach closure) are related to the development of substantial experimental data by which computational simulations may be properly evaluated.

6.2 Conclusions and Recommendations

The conditions in which levee breaches occur, and thus the conditions in which breach closure may be attempted, are influenced by a wide variety of factors. Socio-political conditions may have certain implications upon the most likely locations of levee breaches or the appropriate response to achieve breach closure, as will studies of the efforts required to mobilize construction personnel and equipment to a particular breach site. These complicating factors have been given little or no consideration in this report. Despite a reduction of the levee breach and closure problem to one that is essentially technical, the factors influencing levee breaching and closure remain numerous and widely-varying. Relatively simple empirical equations continue to provide the best techniques for rapidly estimating the sizes of levee breaches as a function of the elapsed time from breaching. These equations may be highly erroneous, though, as they have generally been developed from simple curve-fitting to datasets involving relatively small numbers of documented failures.

In light of the numerous and widely-valued influences upon levee breach geometry, a significant need exists for a reliable means to evaluate conditions which may

exist at the time levee breach closure is attempted. This important link in the breach closure problem will involve supplementary research programs into the mechanisms of breach initiation and growth. These programs, by necessity, would consist primarily of physical experimentation involving the effects of levee geometry, flood and floodwave characteristics, erodibility and strength degradation of compacted soils, and techniques for levee protection ("naturally", as by vegetation, or by synthetic means).

The strongest data may be gained from "in-event" monitoring of active levee breaches. While levee breaches are monitored from afar as a safety precaution, the profession could gain considerable understandings of the mechanisms governing breach growth through collecting data during actual breaching. This type of monitoring may include visual recording referenced to known physical scales and targets, periodic topographic and bathymetric surveys of the breach area during its growth, dye tracer studies, ongoing sampling of soils and pore water conditions within the remaining levee in the vicinity of the breach, sediment sampling, and measurement of fluid velocities and depths in the vicinity of the breach. Ideally, an instrumentation set would be introduced into the breach to record conditions existing in the vicinity of the breach and through the breach itself, in a manner similar to that used by meteorologists to characterize similarly turbulent fluid fields in the vicinity of storms. The instrument set could subsequently be retrieved for analysis to refine understandings of the complex interactions between the fluid flow and levee at the location of a breach.

Observations from experimental programs may then be incorporated into generalized breach growth models which may be used to estimate breach growth for combinations of polders, levee systems, and floods corresponding to specific communities. First responders may then gain a strong approximation of conditions which will exist at the initiation of breach closure through a program of "pre-event breach modeling." This program represents a coordinated effort to evaluate the "typical" conditions which may exist within a specific levee jurisdiction. As an example, the USACE may complete such models for each major river system within a particular District Office to evaluate the size and growth of levee breaches which may be expected within the district. These models could incorporate specific information regarding polder size, polder topography, levee geometries, and flood characteristics to identify the

specific set of conditions within the levee district that create the greatest vulnerability. More sophisticated models may subsequently be developed to combine a levee breach development model with the characteristics of the population which may be influenced by levee breaching.

Advances in breach modeling, presumably to provide more fundamentally sound representations of the mechanics of particle transport, must be considered with a certain degree of pragmatism when applied to computational simulation of large breach closures. While the inclusion of higher fidelity models in numerical approximation is clearly desirable, it may yield little value to a closure effort if the mechanism by which breach closure is achieved (i.e., the process being replicated within the computer simulation) is not physically attainable within the time span necessary to create value to the community affected by the breach. In this way, advances in model sophistication may be greatly tempered by the results of ongoing research efforts to establish the window of time in which breach closure must be achieved and the availability of material and labor resources within that window.

The severe constraints imposed by the limited time available to achieve breach closure may also shift the emphasis of preparedness and response measures away from breach mitigation and toward breach prevention. The time to achieve closure underscores the need for appropriate risk assessments to identify vulnerable levee reaches and the need for staging of repair equipment and materials in the vicinity of these reaches in advance of a pending threat.

With reasonable understanding of the mechanisms governing breach initiation and growth, additional efforts may be placed upon simulation of closure techniques. While this report has focused upon breach closure simulation via computational techniques, the work identified a significant void in the set of physical experiments needed to calibrate all computational models of levee breach closure. This need directly influences the development of computational models, as well as their accuracy and any attempt to ascertain the relative merits of various computational techniques.

Assuming sufficient experimental data may be accumulated to properly calibrate a computational breach closure simulation, significant value remains in extending and applying these models. Models of the sort proposed herein offer immediate values to the

levee breach closure problem in evaluating various proposed techniques for achieving breach closure. These evaluations would permit proper staging and placement of equipment and supply lines during the breach closure process to achieve the most rapid solution in a manner that reduces the risks associated with loss of life or property during construction. Furthermore, computational simulations may provide valuable insight into the dispersal of sediments or construction materials in the vicinity of the levee closure effort, as a result of closure construction. Finally, these simulations may permit evaluation of secondary threats to the levee system or polder which may be introduced during the breach closure construction. These system-wide evaluations of the breach closure process, particularly those in which a large number of construction variables exist, are easily made cost-effective through computational breach closure simulation.

Regarding the computational techniques themselves, the algorithms presented in this report appear to be sufficiently flexible to accommodate modeling of levee breach closure. However, several questions remain regarding the level of sophistication required of the various model parameters (and the appropriate set of values themselves) to faithfully reproduce problems of true physical scale. These problems may be greatly resolved by the results of experiments, as mentioned above. In addition, the algorithms should be compared against competing breach closure models within representative prototype levee breach closure problems. This benchmarking would permit modelers to identify the strengths and weaknesses associated with various computational modeling approaches.

REFERENCES

American Society for Testing and Materials, (2000). "Standard Test Methods for Laboratory Compaction Characteristics of Soil Using Standard Effort," within Annual Book of ASTM Standards, Volume 04.08, ASTM, West Conshohocken, Pennsylvania.

Ariathurai, C. R., and Arulandan, K. (1974). "Erosion Rates of Cohesive Soils," ASCE Journal of the Hydraulics Division, Vol. 104, No. 2, pp. 279-282.

Berger, R.C., and Stockstill, R.L. (1995). "Finite Element Model for High-Velocity Channels," ASCE Journal of Hydraulic Engineering, Vol. 121, No. 10, pp. 710-716.

Berger, R.C., and Howington, S.E., (2002). "Discrete Fluxes and Mass Balance in Finite Elements," ASCE Journal of Hydraulic Engineering, Vol. 128, No. 1, pp. 87-92.

Berger, R.C., and Lee, L.M. (2004). "Multidimensional Numerical Modeling of Surges Over Initially Dry Land," Technical Report ERDC/CHL TR-04-10, United States Army Corps of Engineers Engineering Research and Development Center, 26 pp.

Briaud, J.L., Chen, H.C., Govindasamy, A.V., Storesund, R. (2008). "Erosin by Overtopping in New Orleans During the Katrina Hurricane," ASCE Journal of Geotechnical and GeoEnvironmental Engineering, Vol 134, No. 5, pp. 618-632.

Broich, K. (2005). "Breach Modeling, Description of Breach Model DEICH-P," Report to EU-IMPACT Project, Program EVG1-CT2001-00037, Work Package 2.3, Appendix 1.1. Available online at www.impact-project.net.

Bui, H., Fukagawa, R., Saki, K., and Ohno, S. (2008). "Lagrangian Meshfree Particles Method (SPH) for Large Deformation and Failure Flows of Geomaterial Using Elastic-Plastic Soil Constitutive Model," International Journal for Numerical and Analytical Methods in Geomechanics, Volume 32, pp. 1537-1570.

Calantoni, J., Holland, K., and Drake, T. (2004). "Modelling Sheet-Flow Sediment Transport in Wave-Bottom Boundary Layers Using Discrete-Element Modelling," Philosophical Transactions of the Royal Society of London, Volume 362, pp. 1987-2001.

Carey, W.W. (1970). "Settling of Spheres in Newtonian and Non-Newtonian Fluids," Ph.D. Thesis, Syracuse University.

Chaudhry, M.H. (1993). Open Channel Flow, Prentice Hall, New Jersey, 483 pp.

Cleary, P.W., and Morrison, R.D. (2009). "Particle Methods for Modelling in Mineral Processing," International Journal of Computational Fluid Dynamics, Vol. 23, No. 2, pp. 137-146.

Connell, K.J., Larson, M., and Kraus, N. (2007). "Morphologic Modeling of Multiple Barrier Island Breaches for Regional Application," Proceedings of ASCE Specialty Conference on Coastal Sediments, pp. 2011-2073.

Cundall, P.A. (1978). "An Evaluation of Critical Time Step in the Simulation of Small Particle Kinematics"

Cundall, P.A., and Strack, O.D.L. (1979). "The Distinct Element Method as a Tool for Research in Granular Media, Part I," Report to the U.S. National Science Foundation Concerning NSF Grant ENG76-20711, University of Minnesota Department of Civil and Mineral Engineering.

Cundall, P. (2001). "A Discontinuous Future for Numerical Modelling in Geomechanics," Proceedings of the Institute of Civil Engineers, Issue 1, pp. 41-47.

Davies, T.R., Manville, V., Kunz, M., and Donadini, L. (2007). "Modeling Landslide Dambreak Flood Magnitudes: Case Study," ASCE Journal of Hydraulic Engineering, Vol. 133, No. 7, pp. 713-722.

Davletshin, V.K. (2001). "Failure Dynamics of a Homogeneous Earth Dam Leaking Through a Fissure," Hydrotechnical Construction, Vol. 35, No. 4, pp. 48-52.

DHS (2008). *National Response Framework.* US Department of Homeland Security, Washington, DC, pp. 82.

Fazekas, S., Kertesz, J., and Wolf, D.E. (2005). "Piling and Avalanches of Magnetized Particles," Physical Review E, Volume 71, No. 061303, 9 pp.

Faeh, R. (2007). "Numerical Modeling of Breach Erosion of River Embankments," ASCE Journal of Geotechnical and GeoEnvironmental Engineering, Vol. 133, No. 9, pp. 1000-1009.

Federal Emergency Management Agency, (2009). Photographic Documentation of Hurricane Katrina in Louisiana, available online at: www.fema.gov/hazard/hurricane/2005katrina/slideshow/page1.htm.

Feng, Y. (2005). "On the Central Difference Algorithm in Discrete Element Modeling of Impact," International Journal for Numerical Methods in Engineering, Volume 64, pp. 1959-1980.

Feng, Y., Han, K., and Owen, D.R.J. (2007). "Coupled Lattice Boltzmann Method and Discrete Element Modeling of Particle Transport in Turbulent Fluid Flows: Computational Issues," International Journal for Numerical Methods in Engineering, Vol. 72, pp. 1111-1134.

Foster, M.A., Fell, R., and Spannangle, M. (2000). "The Statistics of Embankment Dam Failures and Accidents," Canadian Geotechnical Journal, Vol. 37, No. 5, pp. 1000-1024.

Fread, D.L. (1987). "BREACH: An Erosion Model for Earthen Dams," National Weather Service Hydrologic Research Laboratory Report, U.S. Department of Commerce, 34 pp.

Fread, D.L., (1996). "Chapter 5: Dam Breach Floods," in Hydrology of Disasters, ed. V.P. Singh, Kluwer Academic Publishing, 439 pp.

Fritz, H.M., and Hager, W.H. (1998). "Hydraulics of Embankment Weirs," ASCE Journal of Hydraulic Engineering, Vol, 124, No. 9, pp. 963-971.

Froehlich, D.C.., (1995). "Embankment Dam Breach Parameters Revisited," Proceedings of the ASCE Specialty Conference on Water Resources Engineering, San Antonio, pp. 887-891.

Gilbert, P.A., and Miller, S. P. (1989). "A Study of Embankment Performance During Overtopping," Technical Report GL-91-23, U.S. Army Corps of Engineers Engineering Research and Development Center, 96 pp.

Han, K., Feng, Y., and Owen, D. (2007). "Coupled Lattice Boltzmann and Discrete Element Modeling of Fluid-Particle Interaction Problems," Computers and Structures, Volume 85, pp. 1080-1088.

Hanson, G., and Temple, D. (2007). "The National Dam Safety Program: Final Report on Coordination and Cooperation with the European Union on Embankment Failure Analysis, FEMA-602," United States Federal Emergency Management Agency, Washington, DC

Hanson, G.J, Cook, K.R., and Hunt, S.L. (2005). "Physical Modeling of Overtopping Erosion and Breach Formation of Cohesive Embankments," Transactions of ASAE, Vol. 48, No. 5, pp 1783-1794.

Heald, J., McEwan, I., and Tait, S. (2004). "Sediment Transport Over a Flat Bed in a Unidirectional Flow: Simulations and Validation," Philosophical Transactions of the Royal Society of London, Volume 362, pp. 1973-1986.

Heyes, D., Baxter, J., Tuzun, U., and Qin, R. (2004). "Discrete-Element Method Simulations: From Micro to Macro Scales," Philosophical Transactions of the Royal Society of London, Volume 362, pp. 1853-1865.

Hobbs, A. (2009). "Simulation of an Aggregrate Dryer Using Coupled CFD and DEM Methods," International Journal of Computational Fluid Dynamics, Vol. 23, No. 2, pp. 199-207.

Jensen, R., and Preece, D. (2000). "Modeling Sand Production with Darcy-Flow Coupled With Discrete Elements," Sandia National Laboratories, Internal Report.

Jiang, M., Yu, H., and Harris, D. (2006). "Bond Rolling Resistance and Its Effect on Yielding Bonded Granulates by DEM Analyses," International Journal for Numerical and Analytical Methods in Geomechanics, Volume 30, pp. 723-761.

Kamrath, P., Disse, M., Hammer, M. and Kongeter, J. (2006). "Assessment of Discharge Through a Dike Breach and Simulation of Flood Wave Propagation," Natural Hazards, Volume 38, pp. 63-78.

Kelley, J.R., Vroman, N., Groves, C., Harder, L., and Sills, G. (2009). "The Spring 2008 Midwest Flood, Observations of Missouri and Iowa Levee Breaches, 21-23 July 2008," Report No. ERDC/GSL SR-09-1, U.S. Army Corps of Engineers Engineering Research and Development Center, 59 pp.

Kock, I., and Huhn, K. (2007). "Influences of Particle Shape on the Frictional Strength of Sediments – A Numerical Case Study," Sedimentary Geology, Volume 196, pp. 217-233.

Koyama, T., and Jing, L. (2007). "Effects of Model Scale and Particle Size on Micro-Mechanical Properties and Failure Processes of Rocks-- A Particle Mechanics Approach," Engineering Analysis with Boundary Elements, Vol. 31, pp. 458-472.

Kumagai, K., Oda, K., Fujii, N. (2006). "Applicability of Simulation Model for Drift Behavior of Containers due to Tsunami," Proceedings of the Nineteenth Engineering Symposium of the Japanese Association of Naval Scientists and Ocean Engineers, Techno-Ocean 2006, Kobe, pp. 1301-1307.

Labra, C., Rojek, J., Onate, E., and Zarate, F. (2008). "Advances in Discrete Element Modelling of Underground Excavations," Acta Geotechnica, Vol. 3, pp. 317-322.

Lyotard, N., Shew, W.L., Bocquet, L, and Pinton, J.-F. (2007). "Polymer and Surface Roughness Effects on the Drag Crisis for Falling Spheres," European Physical Journal B, Vol. 60, No. 4., pp. 469-476.

MacDonald, T.C., and Langridge-Monopolis, J. (1984). "Breaching Characteristics of Dam Failures," ASCE Journal of Water Resources, Vol. 110, No. 5, pp. 567-586.

McAnally, W.H., and Mehta, A.J. (2001). "Collisional Aggregation of Fine Estuarial Sediment," in Coastal and Estuarine Fine Sediment Processes, Elsevier Proceedings in Marine Science, No. 3, pp. 19-39.

Nagy, L. (2006). "Estimating Dike Breach Length from Historical Data," Periodica Polytechnica, Serial Civil Engineering, Vol. 90, No. 2, pp. 125-139.

National Oceanic and Atmospheric Agency (2009). Database of tidal gage data maintained at http://tidesandcurrents.noaa.gov

Nezami, E., Hashash, Y., Zhao, D., and Ghaboussi, J. (2006). "Shortest Link Method for Contact Detection in Discrete Element Method," International Journal for Numerical and Analytical Methods in Geomechanics, Volume 30, pp. 783-801.

Nui, H., Sako, K., and Fukagawa, R. (2007). "Numerical Simulation of Soil-Water Interaction Using Smoothed Particle Hydrodynamics (SPH) Method," Journal of Terramechanics, Volume 44, pp. 339-346.

Owen, D.R.J., Feng, Y.T., DeSouza Neto, E.A., Cottrell, M., Wang, F., Andrade Pires, F.M., and Yu, J. (2004). "The Modelling of Multi-Fracturing Solids and Particulate Media," International Journal for Numerical Methods in Engineering, 2004, Vol. 60, No. 1, pp. 317-340.

Powledge, G.R., Ralston, D.C., Miller, P., Chen, Y.H., Clopper, P.E., and Temple, D.M. (1989). "Mechanics of Overflow Erosion on Embankments. II: Hydraulic and Design Considerations," ASCE Journal of Hydraulic Engineering, Vol. 115, No. 8, pp. 1056-1075.

Pugh, C.A. (1985). "Hydraulic Model Studies of Fuse Plug Embankments," United States Department of the Interior, Bureau of Reclamation Research Report REC-ERC-85-7.

Ratcliffe, T. (1999). "Validation of Free-Surface, Reynolds-Averaged Navier-Stokes and Potential Flow Codes," Proceedings of the Twenty-Second Symposium on Naval Hydrodynamics, National Academy of Sciences, 1016 pp.

Resio, D., Boc, S., Maynord, S., Wal, D., Abraham, D., Dudeck, D., and Welsh, B. (2009). "Development and Deployment of Rapid Repair of Levee Breaching Technology," Report to Southeastern Regional Research Initiative, Department of Homeland Security.

Sanfratello, L. Caprihan, A., and Fukushima, E. (2007). "Velocity Depth Profile of Granular Matter in a Rotating Drum," Granular Matter, Vol. 9, pp. 1-6.

Sattar, A.M.A., Kassem, A.A., and Chaudhry, M.H. (2008). "Case Study: 17 th Street Canal Breach Closure Procedures," ASCE Journal of Geotechnical and GeoEnvironmental Engineering, Vol. 134, No. 11, pp. 1547-1558.

Shames, I.H. (1982). Mechanics of Fluids, Second Edition, McGraw-Hill, 753 pp.

Sills, G. (2009). Personal communication with author.

Singh, V.P., and Scarlatos, P.D. (1985). "Breach Erosion of Earthfill Dams and Flood Routing: BEED Model," United States Army Research Office Report, 131 pp.

Sitharam, T., Dinesh S., and Shimizu, N. (2002). "Micromechanical Modeling of Monotonic Drained and Undrained Shear Behavior of Granular Media Using Three-Dimensional DEM," International Journal for Numerical and Analytical Methods in Geomechanics, Volume 26, pp. 1167-1189.

Staron, L., and Hinch, E.J. (2007). "The Spreading of a Granular Mass: Role of Grain Properties and Initial Conditions," Granular Matter, Vol. 9, pp. 205-217.

Sun, Q., and Li., J. (2001). "Lagrangian Simulations of Gas-Solid Two-Phase Flow: Pseudo Particle Model," Particulate Science and Technology, Vol. 19, pp. 187-197.

United States Army Corps of Engineers, (1966). "Potamology Investigations of Sand-Filled Bags as Dike Material," Report of Potamology Research Project 9, Serial 60567, United States Army Corps of Engineers, Memphis District.

United States Army Corps of Engineers, South Atlantic Division, Mobile District (1970). "Report of Hurricane Camille."

United States Army Corps of Engineers Interagency Performance Evaluation Team (2007a). "Performance Evaluation of the New Orleans and Southeast Louisiana Flood Protection System, Volume 4 – The Storm".

United States Army Corps of Engineers Interagency Performance Evaluation Team (2007b). "Performance Evaluation of the New Orleans and Southeast Louisiana Flood Protection System, Volume 5 – The Performance of Levees and Floodwalls."

United States Bureau of Reclamation, (1988). "Downstream Hazard Classification Guidelines," ACER Technical Memorandum No. 11, United States Department of the Interior, 56 pp.

United States Congress (1898). "Sworn Testimony of Major T.G. Dabney Before the U.S. Senate Special Committee on the Floods of 1897, Recorded February 5, 1898 on board the Steamer 'Mississippi' at Arkansas City," Congressional Record, 55th Congress.

United States Department of Homeland Security (2008). "National Response Framework, FEMA Publication P-682", Federal Emergency Management Agency, Washington, DC, 82 pp.

United States Geological Survey (2009). Database of historical stream gaging data maintained at http://waterwatch.usgs.gov.

Verheij, H. (2002). "Time Dependent Breach Development in Cohesive Material," Internal Research Summary Report, Delft Hydraulics Laboratory. Available online at www.wldelft.nl/rnd/publ/docs/ve_2002.pdf .

Visser, P.J., Zhu, Y., and Vrijling, J.K. (2006). "Breaching of Dikes," Proceedings of the Thirtieth International Conference on Coastal Engineering, San Diego, pp. 2893-2905.

.von Thun, J.L., and Gillette, D.R. (1990). "Guidance on Breach Parameters," Internal Technical Memorandum, United States Bureau of Reclamation, Denver, Colorado, pp.17.

Wahl, T. (1998). "Prediction of Embankment Dam Breach Parameters: A Literature Review and Needs Assessment," United States Department of the Interior, Bureau of Reclamation Water Resources Research Laboratory Report No. DSO-98-004. 60 pp.

Wahl, T., Hanson, G., Courivand, R., Morris, M.W., Kahawita, R., McClenathan, J.T., and Gee, D.M. (2007). "Development of Next-Generation Embankment Dam Breach Models," United States Department of the Interior, Bureau of Reclamation Internal White Paper.

Watanabe, K., Kui, H., Motsui, I. (1998). "Drag of a Sphere in Dilute Polymer Solutions in High Reynolds Number Range," Rheologica Acta, Vol. 37, No. 4, pp. 328-335.

Watson, T. (2004). "When the Wind Blows," Cranes Today, June 2004.

Weiselsberger, C., and Schlichting, H. (1979). Boundary Layer Theory, Seventh Edition, McGraw-Hill, New York.

Yao, M., and Anandarajah, A. (2003). "Three-Dimensional Discrete Element Method of Analysis of Clays," ASCE Journal of Engineering Mechanics, Volume 129, No. 6, pp. 585-596.

Zeghal, M., and el Sharmy, U. (2004). "A Continuum-Discrete Hydromechanical Analysis of Granular Deposit Liquefaction," International Journal for Numerical and Analytical Methods in Geomechanics, Volume 28, pp. 1361-1383.

Zhu, Y., Visser, P.J., and Vrijling, J.K. (2006). "Laboratory Observations of Embankment Breaching," Proceedings of the Seventh International Conference on Hydroscience and Engineering, pp. 1-10.

APPENDIX I

LISTING OF PROGRAM "PHASE-DEM"

FOR

P ARTIALLY-COUPLED
H YDRODYNAMIC
A NALYSES OF
S EDIMENT
E NTRAINMENT BY THE
D ISCRETE
E LEMENT
M ETHOD

```
using System;
using System.Collections.Generic;
using System.Windows.Forms;

namespace DamBreach
{
    static class Program
    {
        /// <summary>
        /// The main entry point for the application.
        /// </summary>
        [STAThread]
        static void Main()
        {
            Application.EnableVisualStyles();
            Application.SetCompatibleTextRenderingDefault(false);
            Application.Run(new mainForm());
        }
    }
}
```

```
using System;
using System.Collections.Generic;
using System.ComponentModel;
using System.Data;
using System.Drawing;
using System.IO;
using System.Text;
using System.Windows.Forms;

namespace DamBreach
{
    public partial class mainForm : Form
    {
        public mainForm()
        {
            InitializeComponent();
        }

        private void xPosBox_MouseDown(object sender, MouseEventArgs e)
        {
            xPosBox.Text = boxClick(xPosBox.Text);
        }

        private string boxClick(string oldText)
        {
            string newText = oldText;
            switch (oldText)
            {
                case "Init. X Pos.":
                case "Radius":
                case "Init. Y Pos.":
                    newText = "";
                    break;
            }
            return newText;
        }

        private void radiusBox_MouseDown(object sender, MouseEventArgs e)
        {
            radiusBox.Text = boxClick(radiusBox.Text);
        }

        private void yPosBox_MouseDown(object sender, MouseEventArgs e)
        {
            yPosBox.Text = boxClick(yPosBox.Text);
        }

        private void exportOut(string fileName, List<string> linesCol)
        {
```

```
            // this overwrites any old files opened by the program, does not append to
end**
            FileStream fs = new FileStream(@fileName, FileMode.Create, FileAccess.Write,
FileShare.Read);
            StreamWriter sw = new StreamWriter(fs);

            foreach (string line in linesCol)
            {
                sw.WriteLine(line);
            }

            sw.Close();
        }

        private void calculateButton_Click(object sender, EventArgs e)
        {
            double xPos, yPos, xVel, yVel, radius;
            radius = 0;
            xPos = 0;
            yPos = 0;
            yVel = 0;
            xVel = 0;

            try
            {
                xPos = Convert.ToDouble(xPosBox.Text);
                yPos = Convert.ToDouble(yPosBox.Text);
                radius = Convert.ToDouble(radiusBox.Text);
            }
            catch (System.FormatException)
            {
                MessageBox.Show("Format Exception, must enter a valid number.");
            }
            catch
            {
                MessageBox.Show("Strange exception.");
            }
            string fileName;

            SaveFileDialog saveFileDialog1 = new SaveFileDialog();
            saveFileDialog1.InitialDirectory = @"C:\";
            saveFileDialog1.Title = "Select a Name to Save to";
            saveFileDialog1.Filter = "Text file (*.txt)|*.txt";
            saveFileDialog1.FileName = "";
            if (saveFileDialog1.ShowDialog() != DialogResult.Cancel)
            {
                fileName = saveFileDialog1.FileName;
            }
            else
            {
                fileName = "";
            }

            if (fileName != "")
            {
                // vertical locations from the bottom boundary (1-D for now) and the
water surface
                double botBound = 0;
                double waterSurface = 500.0;
                double volObj = (4.0 / 3.0) * Math.PI * radius * radius * radius;

                // creates a collection and inputs the initial conditions for Iteration,
Y-Position, Y-Velocity,
                // Overlap, and Y-Acceleration
                List<string> stringCollection = new List<string>();
                string firstLine = "0," + yPos + "," + yVel + ",0,-9.81";
                stringCollection.Add(firstLine);

                // Takes given conditions (including X conditions for now) and runs the
algorithm
```

```
                double[] origCond = {xPos, yPos, xVel, yVel, radius, botBound,
waterSurface, volObj, 0.0, 0.0};
                calculateIt runStart = new calculateIt();                              //
create new instance of Calculation
                List<double> newCond = runStart.calcRun(origCond);                     //
creates a list of doubles as result
                string nextLine = newCond[4] + "," + newCond[0] + "," + newCond[1] + ","
+ newCond[2] + "," + newCond[3];
                stringCollection.Add(nextLine);

                //  newyPos, newyVel, overlap, yAcc, iteration are the parts of
newCond[4]

                while (newCond[4] < 2000)
                {
                    // while the number of iterations is below the set number, this
writes to a string collection
                    // sending to exportOut writes the collection to a NEW (overwriting
any old files) text file
                    double[] secCond = {xPos, newCond[0], xVel, newCond[1], radius,
botBound, waterSurface, volObj,
                        newCond[2],newCond[4]};
                    // sends xPos, yPos, xVel, yVel, radius, botBound, waterSurface,
volObj, overlap, iteration ^
                    newCond = runStart.calcRun(secCond);
                    string nextLine2 = newCond[4] + "," + newCond[0] + "," + newCond[1] +
"," + newCond[2] + "," + newCond[3];
                    stringCollection.Add(nextLine2);
                }
                // sending to exportOut writes the collection to a NEW (overwriting any
old files) text file
                exportOut(fileName, stringCollection);
            }
        }

        public class calculateIt
        {
            public List<double> calcRun(double[] origCond)
            {
                double xPos = origCond[0], yPos = origCond[1], xVel = origCond[2],
                    yVel = origCond[3], radius = origCond[4], botBound = origCond[5],
                    waterSurface = origCond[6], volObj = origCond[7], overlap =
origCond[8],
                    iterCount = origCond[9];
                double specWt = 7800.0;
                double massObj = specWt * volObj;    // 150 pcf or 2402.775 kg/m3 assumed
|||||  7800 to 8010 for steel tests

                // gets a resultant acceleration for the Y-direction
                double newAcc = resultForce(yPos, yVel, radius, waterSurface, volObj,
botBound, overlap, massObj, specWt);

                // gets new velocity and position for the Y-direction
                List<double> newResult = resPos(yPos, yVel, newAcc, botBound, radius,
massObj);
                iterCount++;
                newResult.Add(iterCount);
                return newResult;
            }

            private double resultForce(double yPos, double yVel, double radius, double
waterSurface,
                double volObj, double botBound, double overlap, double massObj, double
specWt)
            {
                // Upward direction positive
                double gAcc = -9.81;
                double yForce = 0.0;
                double addForce = 0.0;

                // determines whether in water or out of water for drag purposes
```

```
                string condition = determineCondition(radius, yVel, yPos, waterSurface);

                // gets a Coefficient of drag for the current iteration
                double dragCoef = dragConstant(radius, yVel, condition);

                if (overlap > 0.0)
                {
                    // if there was overlap from passing the bottom boundary from
previous iteration
                    // coefficients for this spring-interaction not calibrated
                    if (yVel < 0)
                    {
                        addForce = (overlap * 800000.0) + (Math.Abs(yVel) * 200000.0);
                    }
                    else
                    {
                        addForce = (overlap * 800000.0);
                    }
                }

                if ((yPos - radius) >= waterSurface)
                {
                    double surfArea = Math.PI * Math.Pow(radius, 2.0);
                    double dragForce = 0.5 * 1.23 * Math.Pow(Math.Abs(yVel), 2.0) *
surfArea * dragCoef;
                    if (yVel <= 0)
                    {
                        yForce = addForce + (massObj * gAcc) + dragForce;
                    }
                    else if (yVel > 0.0)
                    {
                        yForce = addForce + (massObj * gAcc) - dragForce;
                    }
                }

                else if ((yPos - radius) < waterSurface && (yPos + radius) >
waterSurface)
                {
                    double amountSub = (waterSurface - (yPos - radius));
                    double volDisp;

                    if (amountSub < radius)
                    {
                        volDisp = (1.0 / 3.0) * Math.PI * Math.Pow(amountSub, 2.0) *
((3.0 * radius) - amountSub);
                        double smallRadius = Math.Sqrt(amountSub * ((2.0 * radius) -
amountSub));
                        double surfArea = Math.PI * Math.Pow(smallRadius, 2.0);
                        double surfArea2 = Math.PI * Math.Pow(radius, 2.0);
                        double dragForce = 0.0;

                        if (yVel <= 0)
                        {
                            dragForce = 0.5 * 1000.0 * dragCoef *
Math.Pow(Math.Abs(yVel), 2.0) * surfArea;
                            yForce = addForce + (volDisp * 1000.0 * 9.81) + (massObj *
gAcc) + dragForce;
                        }
                        else if (yVel > 0)
                        {
                            dragForce = 0.5 * 1.23 * dragCoef * Math.Pow(Math.Abs(yVel),
2.0) * surfArea2;
                            yForce = addForce + (volDisp * 1000.0 * 9.81) + (massObj *
gAcc) - dragForce;
                        }
                    }

                    else if (amountSub == radius)
                    {
                        volDisp = ((4.0 / 3.0) * Math.PI * Math.Pow(radius, 2.0)) / 2.0;
                        double surfArea = Math.PI * Math.Pow(radius, 2.0);
```

```
                        double dragForce = 0.0;
                        if (yVel <= 0)
                        {
                            dragForce = 0.5 * 1000.0 * dragCoef *
Math.Pow(Math.Abs(yVel), 2.0) * surfArea;
                            yForce = addForce + (volDisp * 1000.0 * 9.81) + (massObj *
gAcc) + dragForce;
                        }
                        else if (yVel > 0)
                        {
                            dragForce = 0.5 * 1.23 * dragCoef * Math.Pow(Math.Abs(yVel),
2.0) * surfArea;
                            yForce = addForce + (volDisp * 1000.0 * 9.81) + (massObj *
gAcc) - dragForce;
                        }
                    }

                    else if (amountSub > radius)
                    {
                        double height = (yPos + radius) - amountSub;
                        volDisp = ((4.0 / 3.0) * Math.PI * Math.Pow(radius, 2.0)) -
                            (1.0 / 3.0) * Math.PI * Math.Pow(height, 2.0) * ((3.0 *
radius) - height);
                        double surfArea = Math.PI * Math.Pow(radius, 2.0);
                        double smallRadius = Math.Sqrt(height * ((2.0 * radius) -
height));
                        double surfArea2 = Math.PI * Math.Pow(smallRadius, 2.0);
                        double dragForce = 0.0;

                        if (yVel <= 0)
                        {
                            dragForce = 0.5 * 1000.0 * dragCoef *
Math.Pow(Math.Abs(yVel), 2.0) * surfArea;
                            yForce = addForce + (volDisp * 1000.0 * 9.81) + (massObj *
gAcc) + dragForce;
                        }
                        else if (yVel > 0)
                        {
                            dragForce = 0.5 * 1.23 * dragCoef * Math.Pow(Math.Abs(yVel),
2.0) * surfArea2;
                            yForce = addForce + (volDisp * 1000.0 * 9.81) + (massObj *
gAcc) - dragForce;
                        }
                    }
                }

                else if ((yPos + radius) <= waterSurface)
                {
                    // drag is still accounted for if the sphere penetrates into the
ground
                    double volDisp = volObj;
                    double surfArea = Math.PI * Math.Pow(radius, 2.0);
                    double dragForce = 0.5 * 1000.0 * dragCoef * Math.Pow(Math.Abs(yVel),
2.0) * surfArea;
                    if (yVel <= 0)
                    {
                        yForce = addForce + (volDisp * 1000.0 * 9.81) + (massObj * gAcc)
+ dragForce;
                    }
                    if (yVel > 0)
                    {
                        yForce = addForce + (volDisp * 1000.0 * 9.81) + (massObj * gAcc)
- dragForce;
                    }
                }

                double newyAcc = 0.0;
                if ((yPos + radius) <= waterSurface)
                {
                    newyAcc = yForce / ((massObj)*(1 + (0.5 * (1000.0 / specWt))));
                    double testAcc = yForce / massObj;
```

```
            }
            return newyAcc;
        }

        private string determineCondition(double radius, double yVel, double yPos,
double waterLevel)
        {
            /* Makes the following assumptions:
             * 1) if sphere moving downward (negative velocity), the drag switches to
water-based
             *      with given submersed frontal area
             * 2) same assumption for upward movement (positive velocity), but
switches to air as soon as
             *      breaking the surface
             *
             */

            string condition = "";

            if (yVel <= 0)
            {
                if ((yPos - radius) >= waterLevel)
                {
                    condition = "air";
                }
                else if ((yPos - radius) < waterLevel)
                {
                    condition = "water";
                }
            }

            else if (yVel > 0)
            {
                if ((yPos + radius) > waterLevel)
                {
                    condition = "air";
                }
                else if ((yPos + radius) <= waterLevel)
                {
                    condition = "water";
                }
            }
            return condition;
        }

        private double dragConstant(double radius, double yVel, string condition)
        {
            /* Coefficient of drag is determined here with the assumption of the full
surface area of the sphere
             * (for calculation of Reynolds number and thusly the coefficient)
             * as opposed to with only the submerged surface area (as is the case in
the determineCondition method)
             */
            double reynoldsNumber = 0.0;
            if (condition == "water")
            {
                reynoldsNumber = (Math.Abs(yVel) * (2.0 * radius)) / 0.00000112;
            }
            else if (condition == "air")
            {
                reynoldsNumber = (Math.Abs(yVel) * (2.0 * radius)) / 0.0000146;
            }
            if (reynoldsNumber == 0.0)
            {
                reynoldsNumber = 0.000001;
            }

            double dragConstant = 0;

            // Coefficient equations from Wieselberger as per Watanabe
            if (reynoldsNumber > 0.0 && reynoldsNumber < 1.0)
```

```
                {
                    dragConstant = 24.0 / reynoldsNumber;
                }
                else if (reynoldsNumber >= 1.0 && reynoldsNumber < 700.0)
                {
                    dragConstant = 24.0 / (reynoldsNumber * (1.0 + (0.15 *
Math.Pow(reynoldsNumber, 0.687))));
                }
                else if ( reynoldsNumber >= 700.0 && reynoldsNumber < 10443.0)
                {
                    dragConstant = Math.Pow((Math.Pow((24.0 / reynoldsNumber), 0.5) +
(0.34 * (Math.Pow(reynoldsNumber, 0.06) +
                        (1.0 / (1.72 + (0.018 * reynoldsNumber))))))), 2.0);
                }
                else if (reynoldsNumber >= 10443.0 && reynoldsNumber < 1.5e5)
                {
                    dragConstant = (24.0 / reynoldsNumber) + (3.73 /
Math.Pow(reynoldsNumber, 0.5)) -
                        ((0.00483 * Math.Pow(reynoldsNumber, 0.5)) / (1.0 + (0.000003 *
Math.Pow(reynoldsNumber, (3.0 / 2.0)))))
                        + 0.49;
                }
                else if (reynoldsNumber >= 150000.0 && reynoldsNumber < 260000.0)
                {
                    dragConstant = (-0.000000301 * reynoldsNumber) + 0.5187;
                }

                else if (reynoldsNumber >= 260000.0 && reynoldsNumber < 300000.0)
                {
                    dragConstant = (-0.0000014 * reynoldsNumber) + 0.8020;
                }
                else if (reynoldsNumber >= 300000.0 && reynoldsNumber < 379000.0)
                {
                    dragConstant = (-0.0000030144 * reynoldsNumber) + 1.2350;
                }
                else if (reynoldsNumber >= 3.79e5 && reynoldsNumber < 5773859.65)
                {
                    dragConstant = (5.70e-8 * reynoldsNumber) + 0.07089;
                }
                else if (reynoldsNumber >= 5773859.65)
                {
                    dragConstant = 0.2;
                }

                return dragConstant;
            }

            private List<double> resPos(double yPos, double yVel, double yAcc, double
botBound, double radius, double massObj)
            {

                double newyVel = yVel + (yAcc * 0.001);
                double newyPos = yPos + (0.5 * (yVel + newyVel) * 0.001);
                double overlap = 0.0;

                if ((newyPos - radius) < botBound)
                {
                    overlap = botBound - (newyPos - radius);
                }
                double[] interResult = { newyPos, newyVel, overlap, yAcc };
                List<double> result = new List<double>(interResult);

                return result;
            }
        }

        private void mainForm_Load(object sender, EventArgs e)
        {
        }
    }
}
```

OAK RIDGE
National Laboratory

Mississippi State University
CMRC
Construction Materials
Research Center
"An Industry, Agency & University Partnership"

JAMES WORTH
BAGLEY
COLLEGE OF ENGINEERING
MISSISSIPPI STATE UNIVERSITY
CIVIL & ENVIRONMENTAL
ENGINEERING